Aspects of interface modelling in fluid-structure interaction problems.

Joosten, Martina Maria

Swansea University
Prifysgol Abertawe

Aspects of interface modelling in fluid-structure interaction problems

Martina Maria Joosten

Submitted to Swansea University in fulfilment of the requirements for the Degree of Doctor of Philosophy

Supervisors: Prof. D. Perić and Dr. W.G. Dettmer

December 11, 2011

Declarations

This work has not previously been accepted in substance for any degree and is not being concurrently submitted in candidature for any degree.

Signed ..... Date 19-12-2011

This thesis is the result of my own investigations, except where otherwise stated. Other sources are acknowledged by references. A bibliography is appended.

Signed ..... Date 19-12-2011

I hereby give consent for my thesis, if accepted, to be available for photocopying and for interlibrary loan, and for the title and summary to be made available to outside organisations.

Signed ..... Date 19-12-2011

Acknowledgements

I would like to thank Prof. Djordje Perić and Dr. Wulf Dettmer for giving me the opportunity to carry out the research project presented in this thesis. Their help and support has been extremely valuable and encouraging.

I am also thankful for the financial support provided by the Engineering and Physical Sciences Research Council (EPSRC).

Abstract

Different aspects of computational fluid-structure interaction are considered in this work. A brief introduction to fluid dynamics, structural mechanics and the finite element method is given, followed by an overview of interface modelling and the different solution strategies available for the coupling of the domains. A number of time integration schemes are explained in detail with a focus on their stability and accuracy properties. A model problem is introduced to investigate the situation where different domains of a coupled problem are solved with different time integration schemes. It is shown that appropriate interpolation of the solution variables at the interface is required to maintain the stability and accuracy properties of the individual time integration schemes. The Gauß-Seidel solution strategy is analysed in detail. Stability limitations are investigated and are shown to be related to the mass ratio between the different domains. Different relaxation strategies are introduced to improve the convergence behaviour. Finally, a number of 2D fluid-structure interaction examples are considered, in order to compare the different solution strategies.

Contents

Chapter 1

Introduction

Fluid-structure interaction problems are coupled problems with one or more fluid domains, one or more solid domains and one or more interfaces between the fluid and the solid domains. Coupled problems are problems that consist of two or more domains with different physical properties. Different spatial and temporal discretisation techniques may be employed for the domains involved in the coupled problem.

The field of fluid-structure interaction has been the topic of substantial research effort, regarding numerous applications. Research of fluid-structure interaction problems has been carried out amongst others, by [1–17]. Extensive research in fluid-structure interaction has led to knowledge about different solution strategies. However, when modelling the interface a number of questions are still unanswered. In this work, the modelling of the interface for two different time integration schemes is addressed [18]; the limitations of the Gauß-Seidel solution strategy are discussed [19] and a comparison between a number of solution strategies is carried out. For the comparison between different strategies, the Gauß-Seidel strategy is implemented in a code that already contained monolithic and partitioned Newton strategies. Thus all strategies are implemented in exactly the same computer program, solving exactly the same system of nonlinear algebraic equations.

Even though coupled problems, and thus fluid-structure interaction problems, may consist of more than two domains, here only problems are considered with one fluid domain and one solid domain. It is possible to solve the different domains in a coupled problem with different computational strategies, e.g. the finite volume method for one domain and the finite difference

method for the other domain. In here, however, it is chosen to solve both domains with the finite element method. A short introduction into fluid dynamics, solid mechanics and the formulation of the finite element method is given in Chapter 2.

For transient analyses a time integration scheme is applied to the finite element formulation. As the general stability and accuracy of the time integration schemes is important regarding the modelling of fluid-structure interaction problems with two different time integration schemes, Chapter 3 gives a detailed overview of common schemes. The generalised midpoint rule and the generalised-α method are introduced and their stability and accuracy when applied to first and second order model problems is analysed. The terminology and methodology used in this chapter are also used in the following chapters.

Chapter 4 discusses the scenario where the fluid domain and the solid domain are solved with different time integration schemes. The motivation for this chapter comes from the question whether the equilibrium equation at the interface (see Chapter 2) is still satisfied when the integration of the solution variable is not performed at the same time instant within the time step. In order to answer this question, a one dimensional model problem with one degree of freedom is introduced. The model problem consists of two domains and represents a fluid-structure interaction problem. The two domains are solved with the generalised-α method, which allows for user controlled numerical damping and is therefore appropiate to create two different time integration schemes for the two domains.

Another issue addressed in this work are the limitations of the Gauß-Seidel solution strategy. The strategy has been used by many, see *e. g.* [20, 21]. Giving satisfying results for certain situations, stability problems have been reported for other situations. In order to analyse the limitations of the strategy in more detail, another one dimensional model problem is introduced in Chapter 5. For the model problem, one Gauß-Seidel iteration step is calculated analytically. Using the amplification factor that determines the convergence behaviour of the iterative process, stability criteria are established. In addition, constant and adaptive relaxation methods are discussed in order to circumvent possible stability issues.

Finally, in Chapter 6, three different two dimensional numerical examples are discussed in order to confirm the findings from earlier chapters and in order to compare different solution strategies. The numerical examples concern a flow around a flexible beam, an internal flow through a channel with

a flexible part in the wall and a flow through a flexible pipe. The solution strategies are compared based on number of iterations needed per time step and the computational time per time step. Also, the robustness and the complexity of the implementation are discussed.

Chapter 2

The basics of modelling fluid-structure interaction problems

Fluid-structure interaction problems are coupled problems with a fluid domain and a structural domain. Both domains are described by a set of partial differential equations. It is possible to solve each domain with a different method, however, in this work it is chosen to solve both domains with the finite element method. Also, this work is restricted to incompressible Newtonian fluids and elastic solids. In this chapter first the equations that describe the fluid domain and the solid domain are introduced, followed by a short description of the finite element method. Finally, the modelling of the interface and the different solution strategies for the coupled problem are discussed.

2.1 Fluid dynamics

In typical fluid-structure interaction problems the boundary of the fluid domain moves considerably. It is convenient to use the arbitrary Langrangian-Eulerian (ALE) formulation to allow for the motion of the spatial domain. When using a Langrangian formulation the spatial reference frame moves together with the material. This approach is commonly used in the description of solid mechanics. In standard Eulerian fluid flow the spatial domain

remains fixed and therefore does not have a velocity field. In the ALE formulation the spatial reference frame is free to move independently of the fluid.

Only incompressible Newtonian fluids are considered. For the ALE formulation the mass conservation law, or continuity equation, can be written as

$$\nabla \cdot \mathbf{u} = 0 \qquad \forall\, (\hat{\mathbf{x}}, t) \in \Omega \times I \tag{2.1}$$

where $\mathbf{u}$ is the velocity of the fluid, $\hat{\mathbf{x}}$ contains the coordinates associated with the movement of the spatial domain, t is the time and Ω and I are the space and time domain respectively.

For conservation of momentum the following local form can be obtained

$$\rho\left(\dot{\mathbf{u}} + \nabla\mathbf{u}\left(\mathbf{u} - \hat{\mathbf{v}}\right) - \mathbf{f}\right) - \nabla \cdot \boldsymbol{\sigma} = \mathbf{0} \qquad \forall\, (\hat{\mathbf{x}}, t) \in \Omega \times I \tag{2.2}$$

where ρ denotes fluid density, the expression $\dot{\mathbf{u}}$ corresponds to the change of the fluid velocity as seen by an observer travelling with the movement of the spatial domain, $\hat{\mathbf{v}}$ denotes the velocity of the spatial domain, $\mathbf{f}$ gives the body force and $\boldsymbol{\sigma}$ denotes the Cauchy stress tensor. As only Newtonian fluids are considered the Cauchy stress tensor is given as

$$\boldsymbol{\sigma} = -p\mathbf{I} + 2\mu\nabla^s\mathbf{u} \tag{2.3}$$

in which p denotes the pressure, $\mathbf{I}$ denotes the identity tensor, and the fluid viscosity is given by μ. The symmetric part of the gradient is denoted as ∇^s, *e.g.* $\nabla^s\mathbf{u} = \frac{1}{2}\left(\nabla\mathbf{u} + \nabla^T\mathbf{u}\right)$. Equations (2.1), (2.2) and (2.3) together form the Navier-Stokes equations for incompressible fluid flow.

The boundary of the fluid domain can be divided into several subdomains that each require a different set of boundary conditions. The fluid-structure interaction problems considered in this work are flows with interaction between a fluid and an elastic solid. For the fluid domain this means that the boundary Γ is divided into inflow Γ_{in} and outflow Γ_{out} boundaries, slip Γ_{slip} and no-slip $\Gamma_{no-slip}$ boundaries and an interface boundary Γ_i.

At the inflow, the fluid velocity $\mathbf{u}$ is usually described, which leads to the following boundary condition

$$\mathbf{u} - \mathbf{u}_{in} = \mathbf{0} \qquad \forall\, (\hat{\mathbf{x}}, t) \in \Gamma_{in} \times I \tag{2.4}$$

where $\mathbf{u}_{in}$ is the prescribed inflow velocity. At the outflow, the velocity is usually unknown and the boundary traction forces are set to zero

$$\boldsymbol{\sigma}\hat{\mathbf{n}} = \mathbf{0} \qquad \forall\, (\hat{\mathbf{x}}, t) \in \Gamma_{out} \times I. \tag{2.5}$$

On the slip and no-slip boundaries all velocity components normal to the boundary are set to zero. If slip conditions apply then the tangential velocity component is allowed to be non zero, however, if no-slip conditions apply then this component is set to zero as well. This gives for slip conditions the following

$$\mathbf{u} \cdot \hat{\mathbf{n}} = 0, \qquad (\boldsymbol{\sigma}\hat{\mathbf{n}}) \cdot \hat{\mathbf{m}} = 0 \qquad \forall\, (\hat{\mathbf{x}}, t) \in \Gamma_{slip} \times I \tag{2.6}$$

where the normal and the tangential unit vectors of the boundary Γ_{slip} are denoted by respectively $\hat{\mathbf{n}}$ and $\hat{\mathbf{m}}$. For no-slip conditions it follows that

$$\mathbf{u} = \mathbf{0} \qquad \forall\, (\hat{\mathbf{x}}, t) \in \Gamma_{no-slip} \times I. \tag{2.7}$$

The boundary conditions for the interface Γ_i are not as straightforward as the geometry of the interface is not known and will need to be solved for. There are different ways to model the interface between a fluid and a solid. In this work it is chosen to apply no-slip conditions at the interface. This leads to the following

$$\mathbf{u} = \dot{\mathbf{d}} \qquad \forall\, (\hat{\mathbf{x}}, t) \in \Gamma_i \times I \tag{2.8}$$

where $\dot{\mathbf{d}}$ denotes the displacement vector of the solid surface. Also, the normal component of the velocity $\hat{\mathbf{v}}$ of the spatial domain must be equal to the normal component of the fluid velocity $\mathbf{u}$

$$(\mathbf{u} - \hat{\mathbf{v}}) \cdot \hat{\mathbf{n}} = 0 \qquad \forall\, (\hat{\mathbf{x}}, t) \in \Gamma_i \times I. \tag{2.9}$$

Finally, to satisfy the equilibrium of the stresses at the interface, the following boundary condition applies

$$(\boldsymbol{\sigma}\hat{\boldsymbol{n}})_f = -(\boldsymbol{\sigma}\mathbf{n})_s \qquad \forall\, (\hat{\mathbf{x}}, t) \in \Gamma_i \times I \tag{2.10}$$

where $(\boldsymbol{\sigma}\hat{\mathbf{n}})_f$ and $(\boldsymbol{\sigma}\mathbf{n})_s$ denote respectively the traction force exerted by the fluid on the interface and the traction force exerted by the solid on the interface.

2.2 Structural mechanics

In structural mechanics it is common to use the Langrangian approach, which means the movement of the solid coincides with the motion of the spatial reference frame. The displacement of the solid structure is denoted by vector

$\mathbf{d}$ and the material is assumed to be compressible. The momentum conservation law for the structure can be expressed as

$$\rho\left(\ddot{\mathbf{d}} - \mathbf{f}\right) - \nabla \cdot \boldsymbol{\sigma} = \mathbf{0} \qquad \forall\ (\mathbf{x}, t) \in \Omega_s \times I \tag{2.11}$$

where $\ddot{\mathbf{d}}$ expresses the acceleration of the solid structure. The solid structures are often modelled as a Neo-Hookean elastic material, which means that the following stress-strain relation is employed

$$\boldsymbol{\sigma} = \mu J^{-\frac{5}{3}}\left(\mathbf{B} - \frac{1}{3}\mathrm{tr}\left(\mathbf{B}\right)\mathbf{I}\right) + K\frac{J^2 - 1}{2J}\mathbf{I} \tag{2.12}$$

where the shear and the buk moduli of the solid are given by respectively μ and K. The left Cauchy-Green tensor $\mathbf{B}$ and the scalar J are depending on the deformation tensor $\mathbf{F}$

$$\mathbf{B} = \mathbf{F}\mathbf{F}^T, \qquad J = \det\left(\mathbf{F}\right) \tag{2.13}$$

with

$$\mathbf{F} = \frac{\partial \mathbf{x}}{\partial \mathbf{x}_0} = \mathbf{I} + \frac{\partial \mathbf{d}}{\partial \mathbf{x}_0} \tag{2.14}$$

where $\mathbf{x}$ are the coordinates of the current configuration and $\mathbf{x}_0$ are the coordinates of the original configuration.

In fluid-structure interaction, the boundary of the solid domain may consist of different subsections. Parts of the boundary can be fixed Γ_{fixed} or free to move Γ_{free}. This gives the following boundary conditions

$$\mathbf{d} = \mathbf{0} \qquad \forall\ (\mathbf{x}, t) \in \Gamma_{fixed} \times I \tag{2.15}$$

$$\boldsymbol{\sigma}\mathbf{n} = \mathbf{0} \qquad \forall\ (\mathbf{x}, t) \in \Gamma_{free} \times I. \tag{2.16}$$

Sections of the boundary can also be a symmetry plane Γ_{sym}, for which the following conditions apply

$$(\boldsymbol{\sigma}\mathbf{n}) \cdot \mathbf{m} = 0, \qquad \mathbf{d} \cdot \mathbf{n} = 0 \qquad \forall\ (\mathbf{x}, t) \in \Gamma_{sym} \times I \tag{2.17}$$

where again $\mathbf{n}$ and $\mathbf{m}$ express the outward normal and tangential vectors of the boundary respectively. Finally a part of the solid boundary will form the interface with the fluid domain Γ_i. The boundary conditions at the interface are given as

$$\dot{\mathbf{d}} = \mathbf{u}, \qquad (\boldsymbol{\sigma}\mathbf{n})_s = -\left(\boldsymbol{\sigma}\hat{\mathbf{n}}\right)_f \qquad \forall\ (\mathbf{x}, t) \in \Gamma_i \times I \tag{2.18}$$

2.3 Finite element method

2.3.1 Classical Galerkin method

The partial differential equations that describe the fluid and the solid domains are solved using the finite element method. The finite element method has been shown to perform well on structured as well as unstructured meshes. Different formulations have been derived for different types of partial differential equations. This section first gives a general introduction into the finite element method, which will be followed by formulations specifically for the fluid and solid domain. The principles of the finite element method are explained in detail by Hughes [22] and Zienkiewicz *et al.* [23] amongst others.

To illustrate the basic principles of the finite element method the heat conduction equation is introduced, where the temperature distribution u over the domain Ω is described as follows

$$\kappa \Delta u = -f \qquad \forall\, \mathbf{x} \in \Omega. \tag{2.19}$$

The Laplace operator Δu is given by $\nabla \cdot (\nabla(u))$ and f and κ respectively denote the distribution of heat sources in Ω and the conductivity which is assumed to be constant. The Neumann boundary condition for the temperature flux is defined as

$$\mathbf{q} = \kappa \nabla u. \tag{2.20}$$

The principle of virtual temperature is applied to obtain an alternative formulation for Equations (2.19) and (2.20), by multiplication with a virtual perturbation w and subsequent integration over the domain Ω. If $u \in H^1(\Omega)$, then the following perturbations w, also referred to as the test or weighting functions, are allowed

$$w \in \{w \in H^1(\Omega) \mid w = 0 \;\forall\, \mathbf{x} \in \Gamma_g\}. \tag{2.21}$$

If the resulting expression is integrated by parts, with the order of the highest derivative reduced compared to the original equation, then the following formulation can be derived after using the divergence theorem

$$\begin{aligned} \int_\Omega w\,(\kappa \Delta u)\mathrm{d}v &= \int_\Gamma \kappa w\,(\nabla u \cdot \mathbf{n})\mathrm{d}a - \int_\Omega \kappa \nabla w \cdot \nabla u \mathrm{d}v \\ &= \int_{\Gamma_t} w\,(\mathbf{q} \cdot \mathbf{n})\mathrm{d}a - \int_\Omega \kappa \nabla w \cdot \nabla u \mathrm{d}v = -\int_\Omega w f \mathrm{d}v. \end{aligned} \tag{2.22}$$

Applying the Neumann boundary condition that states that $\mathbf{q}(u)\cdot\mathbf{n}-q_t = 0\ \forall\ \mathbf{x}\in\Gamma_t$, where q_t represents prescribed fluxes across the boundary, gives

$$\int_\Omega \kappa\nabla w\cdot\nabla u\mathrm{d}v = \int_{\Gamma_t} wq_t\mathrm{d}a + \int_\Omega wf\mathrm{d}v. \tag{2.23}$$

The exact solution u of Equation (2.19) satisfies Equation (2.23) for every weighting function w that satisfies Equation (2.21). Equations (2.19) and (2.23) are referred to as respectively the strong and the weak form of the problem. The advantage of the weak form of the problem is that it possesses solutions u^h in a finite dimensional subspace, whereas the strong form can only be satisfied by the exact solution u.

This advantage is used to derive the classical Galerkin method: If $u\in W$ and if the finite dimensional subspace of W is denoted by W^h, then an approximate solution $u^h\approx u$ is obtained by finding $u^h\in W^h$ such that

$$\int_\Omega \kappa\nabla w^h\cdot\nabla u^h\mathrm{d}v = \int_{\Gamma_t} w^h q_t\mathrm{d}a + \int_\Omega w^h f\mathrm{d}v \qquad \forall\ w^h\in W^h. \tag{2.24}$$

In summary, the Galerkin method seeks to find solutions $u^h\in W^h$ of the weak form of the problem (2.24) in order to approximate the solution u of the strong form (2.19). For certain choices of the finite dimensional subspace W^h, the Galerkin method leads to the standard finite element method. In this case the finite element spaces W^h are spaces of piecewise continuous polynomials. The domain Ω is divided into n_{el} subdomains Ω^e, which are called finite elements. For each element there is a relation between the domain Ω^e and a parametric element domain. The relation between the parametric coordinates ξ and the element coordinates $\mathbf{x}^h$ is defined as

$$\mathbf{x}^h = \bar{N}_A(\boldsymbol{\xi})\mathbf{x}_A \tag{2.25}$$

for $A=1,2,...,n_{ne}$, with n_{ne} being the number of nodes per element. The coordinates of node A in domain Ω^e are denoted by $\mathbf{x}_A$. The shape functions $N_A=\bar{N}_A(\xi)$ are linearly independent polynomials in the parametric domain and they are equal to one in node A of the element and zero in all other nodes. For each element e a weighting function $w^h\in W^h$ can be expressed as

$$w^h = \bar{N}_A(\xi)\mathbf{w}_A = \hat{N}_A(\mathbf{x}^h)\mathbf{w}_A, \qquad \mathbf{x}^h\in\Omega^e \tag{2.26}$$

where the nodal values of w^h are denoted by $\mathbf{w}_A$.

The finite element mesh is obtained by joining the finite elements together. If the relation given in (2.26) is used for both w^h and u^h, and applied

to all elements in the mesh, then the Galerkin formulation given in (2.24) can be expressed as follows

$$\sum_{e=1}^{n_{el}} \mathbf{w}_A \mathbf{u}_B \int_{\Omega^e} \kappa \nabla N_A \cdot \nabla N_B \mathrm{d}v = \sum_{e=1}^{n_{el}} \mathbf{w}_A \int_{\Gamma_t \cap \Gamma^e} N_A q_t \mathrm{d}a + \sum_{e=1}^{n_{el}} \mathbf{w}_A \int_{\Omega^e} N_A f \mathrm{d}v. \tag{2.27}$$

This can be written in a general form

$$\mathbf{w} \cdot \mathbf{K}\mathbf{u} = \mathbf{w} \cdot \mathbf{P} \tag{2.28}$$

with $\mathbf{K}$ being the stiffness matrix and $\mathbf{P}$ being the external force vector. The vectors $\mathbf{w}$ and $\mathbf{u}$ give the nodal values of the weighting function w^h and the trial solution u^h.

2.3.2 Petrov-Galerkin method

The fluid domain in fluid-structure interaction problems is described with the Navier-Stokes equations, see Section 2.1. It has been shown that the standard Galerkin finite element formulation is not suitable to solve the Navier-Stokes equations, due to instabilities in the velocity and pressure fields [24]. The instabilities can be stabilised by modification of the standard Galerkin formulation. In order to show how the stabilised formulation is derived, the Navier-Stokes equations are considered for a steady state fluid flow on a fixed domain with standard Dirichlet and Neumann conditions. This gives the following simplification of the conservation equation, continuity equation and boundary conditions given in Section 2.1

$$\begin{aligned}
\rho\left((\nabla \mathbf{u})\,\mathbf{u} - \mathbf{f}\right) - \nabla \cdot \boldsymbol{\sigma} &= \mathbf{0} \qquad \forall\, \hat{\mathbf{x}} \in \Omega && (2.29)\\
\nabla \cdot \mathbf{u} &= 0 \qquad \forall\, \hat{\mathbf{x}} \in \Omega && (2.30)\\
\mathbf{u} - \mathbf{q}_g &= \mathbf{0} \qquad \forall\, \hat{\mathbf{x}} \in \Gamma_g && (2.31)\\
\boldsymbol{\sigma}\mathbf{n} - \mathbf{q}_t &= \mathbf{0} \qquad \forall\, \hat{\mathbf{x}} \in \Gamma_t && (2.32)
\end{aligned}$$

with

$$\boldsymbol{\sigma} = -p\mathbf{I} + 2\mu\nabla^s \mathbf{u}. \tag{2.33}$$

The weak form can be derived in a similar way as described in Section 2.3.1. With the perturbations in velocity and pressure respectively denoted by $\mathbf{w}$ and q, the weak form is given as

$$\int_\Omega \mathbf{w} \cdot \rho\left((\nabla \mathbf{u})\,\mathbf{u} - \mathbf{f}\right) - (\nabla \cdot \mathbf{w})\,p + 2\mu\nabla\mathbf{w} : \nabla^s\mathbf{u} + q\,(\nabla \cdot \mathbf{u})\mathrm{d}v - \int_{\Gamma_t} \mathbf{w} \cdot \mathbf{q}_t \mathrm{d}a = 0. \tag{2.34}$$

By replacing the subdomains of $\mathbf{u}$, $\mathbf{w}$, p and q with finite element spaces, the standard Galerkin formulation for the Navier-Stokes equations can be formulated

$$\int_{\Omega} \mathbf{w}^h \cdot \rho \left(\left(\nabla \mathbf{u}^h \right) \mathbf{u}^h - \mathbf{f} \right) - \left(\nabla \cdot \mathbf{w}^h \right) p^h + 2\mu \nabla \mathbf{w}^h : \nabla^s \mathbf{u}^h + q^h \left(\nabla \cdot \mathbf{u}^h \right) \mathrm{d}v - \int_{\Gamma_t} \mathbf{w}^h \cdot \mathbf{q}_t^h \mathrm{d}a = 0. \quad (2.35)$$

It can be shown that instabilities in the velocity field occur for the solution of Equation (2.35) when it is advection dominated. The instabilities in the pressure field are related to the choices for the finite dimensional subspaces. For the standard Galerkin formulation, the finite dimensional subspaces are chosen as equal order piecewise polynomials, which have been shown to lead to additional instabilities by *e.g.* [24, 25]. Both the velocity and the pressure field can be stabilised with certain techniques, as will be described in the next section.

Stabilisation of the velocity field

A simple stabilisation technique for the velocity field is the addition of artificial diffusion. The amount of artificial diffusion for optimal results varies within the domain Ω and depends on the properties of the discretised problem, as discussed by Johnson [26] and Hirsch [27], among others. It is obvious that the performance of this technique very much depends on the amount of artificial diffusion that is applied. It can be shown that the accuracy significantly improves when the artificial diffusion is only applied in the direction of the flow. This is called the streamline diffusion method, as no artificial diffusion is applied perpendicular to the streamlines (crosswind diffusion). As a final improvement, the weighting functions can be defined in such a way that for a certain finite element node, the adjoint upstream elements are weighted more heavily than the downstream elements. This stabilisation technique is called the streamline-upwinding/Petrov-Galerkin (SUPG) method and is studied in *e.g.* [26, 28].

Stabilisation of the pressure field

For the stabilisation of the pressure field, the pressure-stabilising/Petrov-Galerkin (PSPG) method was developed by Hughes *et al* [29]. Similar to the

SUPG method, a stabilisation term is added to the standard Galerkin formulation. In the standard Galerkin formulation the only term that involves the pressure is $(\nabla \cdot \mathbf{w}^h)p^h$, which is not sufficient to damp out spurious modes of the pressure for equal order velocity and pressure interpolations. This is caused by the fact that the Babuška-Brezzi condition is not satisfied [30,31]. The Babuška-Brezzi condition restricts the dimension of the finite dimensional subspace P^h in relation to W^h, in order to guarantee convergence of the solution as the mesh is refined. The added stabilisation term involves $\nabla q^h \cdot \nabla p^h$, which circumvents the Babuška-Brezzi condition and therefore leads to a good performance of the stabilised scheme.

SUPG/PSPG formulation

Even though the origins of the instabilities in the velocity and pressure fields are different, the stabilisation techniques are similar. For the incompressible steady state Navier-Stokes equations it is therefore straightforward to combine stabilisation of the velocity field with the stabilisation of the pressure field to obtain a stable finite element method

$$\begin{aligned}\int_\Omega \Big[\mathbf{w}^h \cdot \rho\left(\left(\nabla \mathbf{u}^h\right)\mathbf{u}^h - \mathbf{f}\right) - \left(\nabla \cdot \mathbf{w}^h\right)p^h \\ +2\mu\nabla\mathbf{w}^h : \nabla^s\mathbf{u}^h + q^h\left(\nabla\cdot\mathbf{u}^h\right)\Big]\,\mathrm{d}v - \int_{\Gamma_t}\mathbf{w}^h\cdot\mathbf{q}_t^h\mathrm{d}a \\ + \sum_{e=1}^{n_{el}}\int_{\Omega^e}\left[\tau_{\mathbf{u}}\rho\left(\nabla\mathbf{w}^h\right)\mathbf{u}^h + \tau_p\nabla q^h\right]\cdot\left[\rho\left(\left(\nabla\mathbf{u}^h\right)\mathbf{u}^h - \mathbf{f}\right) + \nabla p^h\right]\mathrm{d}v = 0.\end{aligned} \tag{2.36}$$

The formulation contains two stabilisation parameters, $\tau_{\mathbf{u}}$ and τ_p, which allows independent control of the velocity and pressure stabilisations. Following Dettmer and Perić [4], the stabilisation parameters are both defined as

$$\tau = \frac{h^e}{2||\mathbf{u}^e||\rho}\xi, \qquad \xi = \frac{\beta_1}{\sqrt{1+\left(\frac{\beta_1}{\beta_2 \mathrm{Re}^e}\right)^2}}, \qquad \mathrm{Re}^e = \frac{||\mathbf{u}^e||h^e\rho}{2\mu} \tag{2.37}$$

however, the scaling parameters β_1 and β_2 can be set independently. The characteristic element size is denoted by h^e, the fluid velocity in the element

centroid by $\mathbf{u}^e$ and the element Reynolds number by Re^e. For the characteristic element size the following relation is used

$$h^e = \sqrt{\frac{4A^e}{\pi}} \tag{2.38}$$

where A^e is the area of the triangular finite element in the 2D setting. Different choices can be made for the values of the scaling parameters β_1 and β_2. Based on the motivation given in [25], the following values are used in this work

$$\tau_{\mathbf{u}}: \quad \beta_1 = 1, \qquad \beta_2 = \frac{1}{3} \tag{2.39}$$

$$\tau_p: \quad \beta_1 = 30, \qquad \beta_2 = \frac{1}{10}. \tag{2.40}$$

Equation (2.36) gives the SUPG/PSPG formulation for the incompressible steady state Navier-Stokes equations. For transient problems a time integration scheme is applied, as discussed in more detail in Chapter 3. To be able to use the formulation in Equation (2.36), this will need to be adjusted for moving domains. Based on the governing equation, the SUPG/PSPG formulation for the Navier-Stokes equations in an ALE framework can be expressed as

$$\begin{aligned}\int_\Omega \Big[\mathbf{w}^h \cdot \rho\left(\dot{\mathbf{u}}^h + \left(\nabla \mathbf{u}^h\right)\left(\mathbf{u}^h - \hat{\mathbf{v}}^h\right) - \mathbf{f}\right) - \left(\nabla \cdot \mathbf{w}^h\right) p^h + 2\mu \nabla \mathbf{w}^h : \nabla^s \mathbf{u}^h \\ + q^h \left(\nabla \cdot \mathbf{u}^h\right)\Big] \mathrm{d}v - \int_{\Gamma_t} \mathbf{w}^h \cdot \mathbf{q}_t^h \mathrm{d}a + \sum_{e=1}^{n_{el}} \int_{\Omega^e} \left[\tau_{\mathbf{u}} \rho \left(\nabla \mathbf{w}^h\right)\left(\mathbf{u}^h - \hat{\mathbf{v}}^h\right) + \tau_p \nabla q^h\right] \\ \cdot \left[\rho\left(\dot{\mathbf{u}}^h + \left(\nabla \mathbf{u}^h\right)\left(\mathbf{u}^h - \hat{\mathbf{v}}^h\right) - \mathbf{f}\right) + \nabla p^h\right] \mathrm{d}v = 0.\end{aligned} \tag{2.41}$$

Also the definitions for the stabilisation parameters $\tau_{\mathbf{u}}$ and τ_p are adjusted for the moving domain

$$\tau = \frac{h^e}{2||\mathbf{u}^e - \hat{\mathbf{v}}^e||\rho}\xi, \qquad \xi = \frac{\beta_1}{\sqrt{1 + \left(\frac{\beta_1}{\beta_2 \mathrm{Re}^e}\right)^2}}, \qquad \mathrm{Re}^e = \frac{||\mathbf{u}^e - \hat{\mathbf{v}}^e||h^e \rho}{2\mu}. \tag{2.42}$$

Apart from the time integration schemes, also a mesh updating algorithm is needed for transient analyses. There are two different mesh updating algorithms used in this work. The first one, the pseudo-elastic technique, assumes the mesh to represent an elastic solid body. The new geometry of the domain is then obtained by applying a standard Lagrangian finite element

technique. The other algorithm that is used aims for the optimisation of the aspect ratio. This means that the aspect ratio of the elements is used to create a mesh with an optimal quality. Both approaches require the application of a Newton-Raphson procedure. See Dettmer [25] for details.

2.4 Fluid-structure interaction

2.4.1 The interface

Due to the nature of the physical behaviour, the fluid domain often requires a denser mesh than the the solid domain to solve a problem. To prevent the need for an equally dense solid mesh, the interface should be capable of combining non matching boundary nodes. The position of the solid interface nodes follows from the structural deformation, which determines the position of the fluid interface nodes, and subsequently the position of the internal fluid nodes. At the interface, no-slip conditions require that the displacements and the velocities at the fluid interface and the solid interface coincide with the motion of the fluid and solid mesh boundaries. A finite element interpolation of the solid allows the transfer of kinematic data between the solid and the fluid at the interface, which can be expressed as follows

$$\hat{\mathbf{x}}_A = c_{B,A}\left(\mathbf{x}_{B,0} + \mathbf{d}_B\right) \tag{2.43}$$

$$\mathbf{u}_A = \hat{\mathbf{v}}_A = c_{B,A}\,\dot{\mathbf{d}}_B \tag{2.44}$$

where A and B refer to a fluid interface node and a nearby solid interface node, respectively. The kinematic data for the fluid interface node A is found by interpolation between solid interface node B and its neighbouring interface node. So $\hat{\mathbf{x}}_A$, $\mathbf{u}_A$, $\hat{\mathbf{v}}_A$ and $\dot{\mathbf{u}}_A$ are the nodal values in A of respectively $\hat{\mathbf{u}}^h$, $\mathbf{u}^h$, $\hat{\mathbf{v}}^h$ and $\dot{\mathbf{u}}^h$. Similarly, the displacement, velocity and acceleration of the solid interface node B are denoted by $\mathbf{d}_B$, $\dot{\mathbf{d}}_B$ and $\ddot{\mathbf{d}}_B$. The value of the structural shape function associated with node B, and evaluated at the position of the fluid interface node A, is denoted by $c_{B,A}$.

To satisfy equilibrium of the forces at the interface, the nodal residual forces of the fluid and the solid are balanced by the principle of virtual work. A virtual displacement of the interface can be expressed as

$$\delta d = N_B^s \delta \mathbf{d}_B \tag{2.45}$$

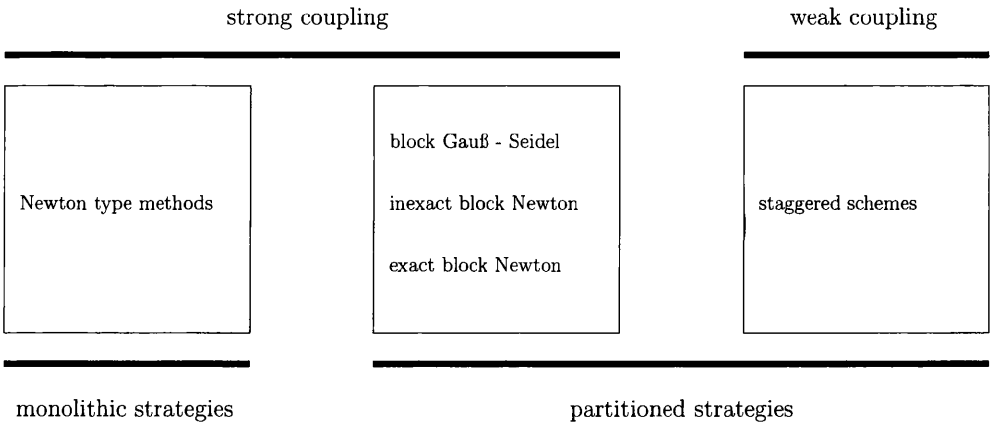

Figure 2.1: Overview of solution algorithms.

which leads to the following sum of the work of the fluid and the solid nodal forces

$$\delta W = \mathbf{g}_A^f N_B^s(\xi_A)\,\delta\mathbf{d}_B + \mathbf{g}_B^s \delta\mathbf{d}_B = 0. \tag{2.46}$$

The vectors $\mathbf{g}_A^f$ and $\mathbf{g}_B^s$ express the fluid residual force in fluid interface node A and the solid residual force in solid interface node B respectively. This results in

$$\mathbf{g}_A^f c_{B,A} + \mathbf{g}_B^s = 0. \tag{2.47}$$

The formulation is based on the principle that the momentum and energy released by the fluid is identical to momentum and energy absorbed by the solid and vice versa. However, the time discretisation of the fluid and the solid domains might influence the exact conservation. This issue is addressed in Chapter 4.

There are several solution strategies possible to solve the coupling between the domains. The different strategies can roughly be divided between partitioned and monolithic schemes and include weakly and strongly coupled algorithms. A schematic overview of the available solution strategies can be found in Figure 2.1. Strongly coupled algorithms are methods in which the global conditions, such as equilibrium, are satisfied in each time step up to the desired convergence tolerance which leads to the exact solution of total system of discretised equations. In weakly coupled strategies this is not the case as small errors in the residuals of the equations are allowed.

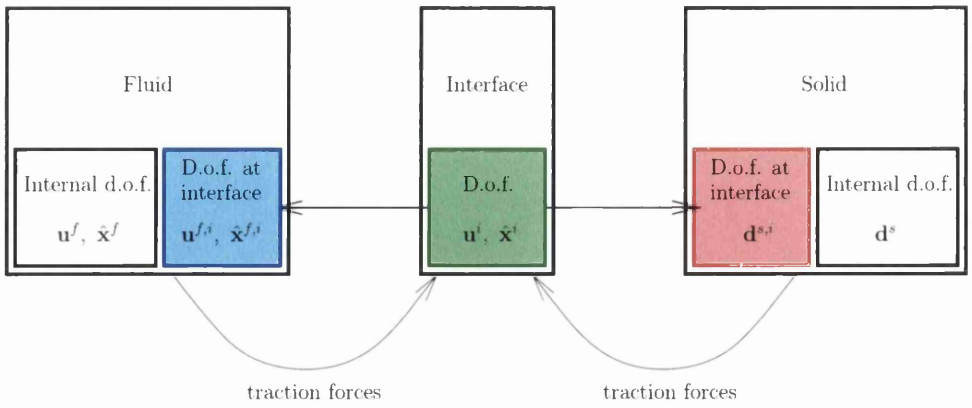

Figure 2.2: Schematic view of the domain decomposition for the strongly coupled strategies.

2.4.2 Weakly coupled strategies - Staggered schemes

In the weakly coupled strategies, or staggered schemes, a prescribed sequence of solution steps is followed to obtain an approximation of the solution at time instant t_{n+1}. The sequence of solution steps includes the solvers of the different domains, predictor steps and communication of data between the domains. The different domains are solved separately, which means that weakly coupled strategies are partitioned strategies.

It is relatively straightforward to implement staggered schemes and make use of existing computer codes. It is for this reason that staggered schemes are a popular choice to solve large scale problems. However, as the total system of equations is not solved exactly, appropiate accuracy and stability properties need to be ensured.

2.4.3 Strongly coupled strategies

The strongly coupled strategies can be divided into monolithic and partitioned strategies. In a monolithic strategy the entire set of coupled equations is solved simultaneously, whereas in a partitioned strategy the system of equations is decomposed into subsystems which are then solved separately. The partitioned strategies that are discussed are the Gauss-Seidel solution strategy and exact and inexact block Newton solution strategies.

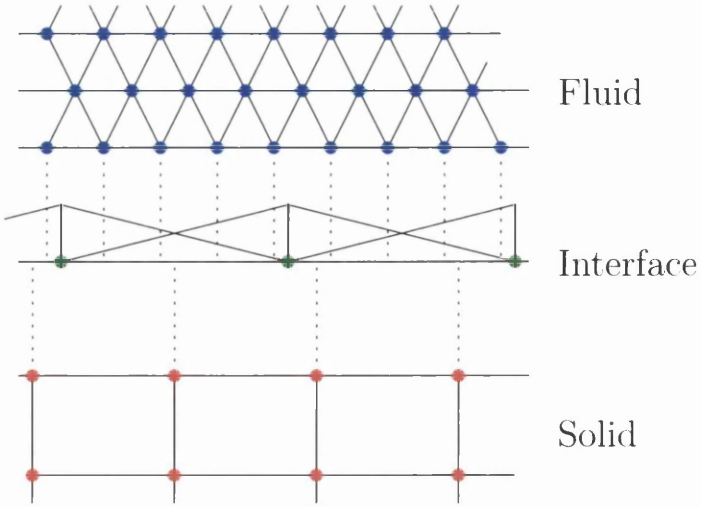

Figure 2.3: Modelling of the interface domain, with transfer based on finite element type interpolation.

In order to describe the different solution strategies, the interface domain is introduced [32]. The interface domain degrees of freedom describe the configuration of the interface, using linear finite element type interpolation based on nodes and shape functions. The decomposition of the problem into the subdomains fluid, interface and solid is illustrated in Figure 2.2. Appropiate transfer operators account for the relation between the degrees of freedom of the interface domain and the degrees of freedom on the boundaries of the fluid and solid domain. The vectors $\mathbf{u}^f$ and $\mathbf{d}^s$ consist of all internal degrees of freedom of the fluid and the solid domain respectively.

The nodes of the interface domain have a configuration independent from the fluid and solid interface configurations, as is shown in Figure 2.3. The interpolation algorithm described in Section 2.4.1 is therefore applied between the interface domain and the fluid domain and also between the interface domain and the solid domain. This increases the flexibility and modularity of the computer program.

To show the differences between the strongly coupled strategies considered in this work, the coupled problem is described with the following set of equations

$$\mathbf{r}^f(\mathbf{u}^f, \mathbf{u}^i) = \mathbf{0} \quad \text{(fluid)} \tag{2.48}$$

$$\mathbf{r}^i(\mathbf{u}^f, \mathbf{u}^i, \mathbf{d}^s) = \mathbf{0} \quad \text{(interface)} \tag{2.49}$$

$$\mathbf{r}^s(\mathbf{u}^i, \mathbf{d}^s) = \mathbf{0} \quad \text{(solid)} \tag{2.50}$$

This is a simplification of the overall problem, which also includes equations for the movement of the mesh as described in previous sections.

Monolithic strategy

For a monolithic strategy the total system matrix is assembled, including the different domain solvers, and then solved using a Newton-Raphson procedure, see *e. g.* [12]. This leads to a stiffness matrix of the structure as shown in Figure 2.4(a). To solve the coupled problem the entire set of equations is solved simultaneously:

1. Guess $\mathbf{u}^f$, $\mathbf{u}^i$ and $\mathbf{d}^s$
2. $$\begin{bmatrix} \mathbf{K}_{ff} & \mathbf{K}_{fi} & \mathbf{0} \\ \mathbf{K}_{if} & \mathbf{K}_{ii} & \mathbf{K}_{is} \\ \mathbf{0} & \mathbf{K}_{si} & \mathbf{K}_{ss} \end{bmatrix} \cdot \begin{Bmatrix} \Delta\mathbf{u}^f \\ \Delta\mathbf{u}^i \\ \Delta\mathbf{u}^s \end{Bmatrix} = - \begin{Bmatrix} \mathbf{r}^f(\mathbf{u}^f, \mathbf{u}^i) \\ \mathbf{r}^i(\mathbf{u}^f, \mathbf{u}^i, \mathbf{u}^s) \\ \mathbf{r}^s(\mathbf{u}^i, \mathbf{u}^s) \end{Bmatrix} \tag{2.51}$$
$$\begin{Bmatrix} \mathbf{u}^f \\ \mathbf{u}^i \\ \mathbf{d}^s \end{Bmatrix} \leftarrow \begin{Bmatrix} \mathbf{u}^f \\ \mathbf{u}^i \\ \mathbf{d}^s \end{Bmatrix} + \begin{Bmatrix} \Delta\mathbf{u}^f \\ \Delta\mathbf{u}^i \\ \Delta\mathbf{d}^s \end{Bmatrix} \tag{2.52}$$
3. If no convergence, go back to 2

Partitioned Newton-Raphson strategy

The partitioned Newton-Raphson strategies have been developed as a result of limitations of other partioned strategies and can be divided into "exact" and "inexact" block Newton methods ((see [1, 3, 4, 6, 32] for the former and [7–11] for the latter)). The main difference between the partitioned Newton scheme and the monolithic strategy is the elimination of the solid domain, which is illustrated in Figure 2.4(b). Elimination of the solid reduces the size of the assembled stiffness matrix. The algorithm for the partioned Newton strategy is as follows

1. Guess $\mathbf{u}^f$ and $\mathbf{u}^i$

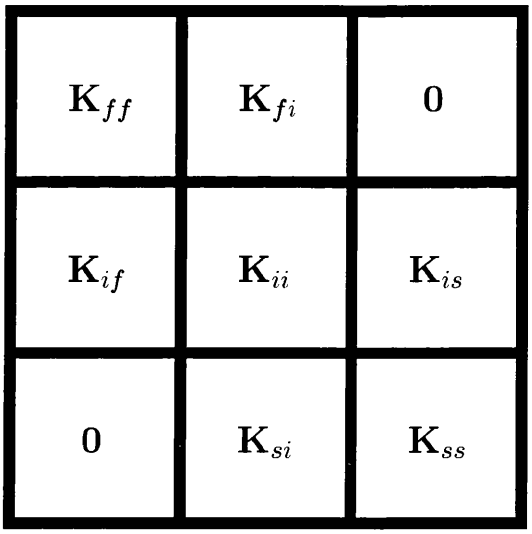

(a) Stiffness matrix for the monolithic strategy.

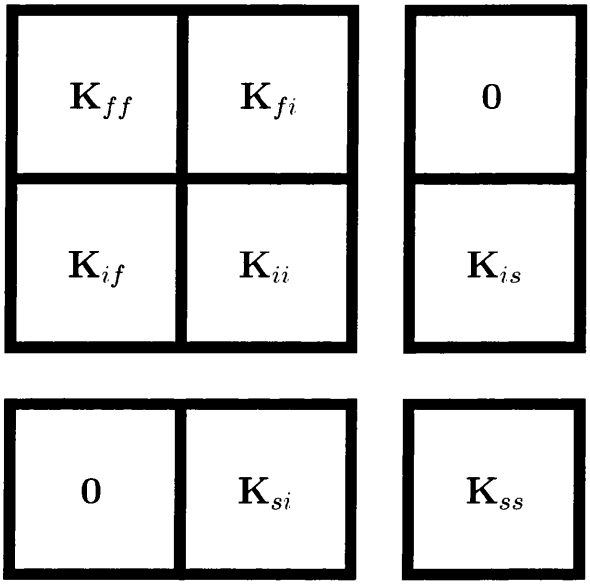

(b) Stiffness matrix decomposition for the partitioned Newton strategy.

Figure 2.4: Stiffness matrix decompositions for different solution strategies.

2.

$$\mathbf{K}_{ss}\Delta\mathbf{d}^s = -\mathbf{r}^s(\mathbf{u}^i, \mathbf{d}^s) \tag{2.53}$$

$$\mathbf{d}^s \leftarrow \mathbf{d}^s + \Delta\mathbf{d}^s \tag{2.54}$$

3. If no convergence, go back to 2

4.

$$\mathbf{S} = \mathbf{K}_{ii} - \mathbf{K}_{is}\mathbf{K}_{ss}^{-1}\mathbf{K}_{si} \tag{2.55}$$

$$\begin{bmatrix} \mathbf{K}_{ff} & \mathbf{K}_{fi} \\ \mathbf{K}_{if} & \mathbf{S} \end{bmatrix} \cdot \begin{Bmatrix} \Delta\mathbf{u}^f \\ \Delta\mathbf{u}^i \end{Bmatrix} = \begin{Bmatrix} r^f(\mathbf{u}^f, \mathbf{u}^i) \\ r^i(\mathbf{u}^f, \mathbf{u}^i, \mathbf{d}^s) \end{Bmatrix} \tag{2.56}$$

$$\begin{Bmatrix} \mathbf{u}^f \\ \mathbf{u}^i \end{Bmatrix} \leftarrow \begin{Bmatrix} \mathbf{u}^f \\ \mathbf{u}^i \end{Bmatrix} + \begin{Bmatrix} \Delta\mathbf{u}^f \\ \Delta\mathbf{u}^i \end{Bmatrix} \tag{2.57}$$

5. If no convergence, go back to 2

Here, $\mathbf{S}$ denotes the so-called Schur complement matrix. For matrices in block form, the Schur complement is the result of eliminating a block using the block Gaussian elimination with reference to another block. For more details about the Schur complement see *e.g.* [33].

Gauß-Seidel solution strategy

The Gauß-Seidel strategy is another partitioned strategy. However, for this strategy there is no need to assemble the entire stiffness matrix and the interface domain acts merely as a data transfer operator. The fluid and solid domains are solved separately and data is transferred in between them. The strategy, also referred to as Dirichlet-Neumann coupling, is widely used for the resolution of the strong coupling between the fluid and the solid domains [16, 17]. It corresponds to the classical Gauß-Seidel scheme for the iterative solution of systems of linear equations. The reason for the popularity of the strategy lies in its high degree of modularity. It allows for the relatively straightforward combination of existing fluid and solid solvers without requiring significant modifications or even the full understanding of the two solvers. The Gauß-Seidel solution strategy has been investigated in the past in the context of coupled physical problems, by, amongst others, Turska and Schrefler [20] for convergence analysis of a block Gauß- Seidel method for consolidation problems, Armero and Simo [21] for analysis of thermo-mechanical problems, Schrefler et. al. [34] for analysis of thermo-hydro-mechanical problems, Vijalapura and Govindjee [35] for analysis of

diffusion-deformation-reaction problems and Felippa et al [14] for the analysis of generic coupled problems.

A detailed discussion of the Gauß-Seidel solution strategy and its stability and accuracy properties is given in Chapter 5.

2.4.4 Comparison of the solution strategies

In Chapter 6, numerical examples are used to compare some of the solution strategies. The solution strategies considered are partitioned Newton-Raphson strategy, the monolithic strategy and the Gauß-Seidel strategy. To evaluate the performance of the solution strategies the following criteria are relevant.

- Accuracy and stability: Solution strategies may give inaccurate results, or instabilities may occur which means failure to give any results at all.
- Robustness: For any reasonable time step size the strategies will need to converge to a solution.
- Computational time: Some strategies are computationally expensive which obviously is a disadvantage.
- Suitability for parallelisation: To improve the computational time, it may be beneficial to parallelise the solution strategy.
- Complexity of computer implementation: Some of the solution strategies discussed require the development of a complex computer program, which may not be desirable.

These criteria will be addressed in Chapter 6, when different numerical examples are solved using the different solution strategies.

Chapter 3

Stability and accuracy of time integration schemes

In this chapter the stability and accuracy of different time integration schemes is discussed. The chapter gives an overview of available schemes for the time integration procedures for the stabilised finite element formulation given in the previous chapter. A number of model problems are used to illustrate characteristics of the schemes and introduce terminology concerned with stability and accuracy.

Regarding the discrete time integration schemes that are considered in this chapter, it is chosen to restrict the focus to single step time integration schemes. They are the trapezoidal rule, the backward Euler method, the generalised midpoint rule and the generalised-α method. The trapezoidal rule and the backward Euler method are chosen as they only depend on time discretisation parameter Δt and therefore allow for the detailed analysis of a solution procedure for coupled problems in a later chapter. The generalised midpoint rule and the generalised-α method have been shown to perform well when applied to incompressible fluid flow governed by the Navier-Stokes equations [36] and are therefore used in later examples. For structural dynamics problems the generalised-α method has been shown to give accurate results and has the benefit of user controlled high frequency damping [37,38].

Other procedures to solve for the integration in time are the time finite element methods. When the finite element method is used for both the space and time domains, this results in the so-called space-time finite element methods, as opposed to semi-discrete solution procedures where the

finite element method in the space domain is combined with a discrete time integration scheme. In Dettmer and Perić [36] the performance of a number of time finite element methods are compared with discrete time integration schemes. Especially the linear discontinuous in time space-time finite element method has shown good results, however, [36] compares the method with the generalised-α method for first order systems and motivates why the latter is the preferred time integration scheme when modelling fluid mechanics.

In this chapter first a number of time integration schemes will be introduced (backward Euler method, trapezoidal rule and generalised midpoint rule), followed by an analysis of their stability and accuracy based on a selection of one dimensional model problems. For the mathematical analysis of the time integration schemes and computing the data for the eigenvalue plots, symbolic software is used.

3.1 Backward Euler method

The first time integration scheme considered is the backward Euler (BE) method. The backward Euler method is an implicit time integration scheme where the derivatives are evaluated at time instant t_{n+1}. For linear problems, this method is first order accurate and unconditionally stable, as is shown in Section 3.4. Its major drawback is the relatively large amount of numerical damping. For a second order problem, the backward Euler method is defined by the following expressions

$$u_{n+1} = u_n + \Delta t\, \dot{u}_{n+1} \tag{3.1}$$

$$\dot{u}_{n+1} = \dot{u}_n + \Delta t\, \ddot{u}_{n+1} \tag{3.2}$$

where u_n and u_{n+1} are scalar variables at respectively time instant t_n and time instant t_{n+1}, $\dot{u}_n$ and $\dot{u}_{n+1}$ are the time derivatives at respectively time instant t_n and time instant t_{n+1} and $\ddot{u}_{n+1}$ is the second derivative in time at time instant t_{n+1}. The time step size is denoted by $\Delta t = t_{n+1} - t_n$ and the problem is to be solved at time instant t_{n+1}.

3.2 Trapezoidal rule

The trapezoidal rule (TR) is another implicit method and is different from the backward Euler method in that the derivatives are evaluated at time

instant $t_{n+\frac{1}{2}}$. In Section 3.4, the trapezoidal rule is shown to be second order accurate and unconditionally stable for a linear problem. The method does not exhibit any numerical damping. The expressions that define the trapezoidal rule method for a second order problem are as follows

$$u_{n+\frac{1}{2}} = \frac{u_n + u_{n+1}}{2} \tag{3.3}$$

$$\dot{u}_{n+\frac{1}{2}} = \frac{\dot{u}_n + \dot{u}_{n+1}}{2} \tag{3.4}$$

$$\ddot{u}_{n+\frac{1}{2}} = \frac{\ddot{u}_n + \ddot{u}_{n+1}}{2} \tag{3.5}$$

$$u_{n+1} = u_n + \Delta t\, \dot{u}_{n+\frac{1}{2}} \tag{3.6}$$

$$\dot{u}_{n+1} = \dot{u}_n + \Delta t\, \ddot{u}_{n+\frac{1}{2}} \tag{3.7}$$

with $u_{n+\frac{1}{2}}$, $\dot{u}_{n+\frac{1}{2}}$ and $\ddot{u}_{n+\frac{1}{2}}$ being respectively a scalar variable, its time derivative and its second time derivative at time instant $t_{n+\frac{1}{2}}$.

3.3 Generalised midpoint rule

The difference between the backward Euler method and the trapezoidal rule is the time instant at which the time derivatives are evaluated. To allow the user to control the time instant, and therefore the amount of numerical damping, the generalised midpoint rule (GM) is often used. The time derivative will now be evaluated at time instant $t_{n+\gamma}$, where $0 \leq \gamma \leq 1$. This leads to the following expressions for a second order problem

$$u_{n+\gamma} = \gamma\, u_{n+1} + (1-\gamma)\, u_n \tag{3.8}$$

$$\dot{u}_{n+\gamma} = \gamma\, \dot{u}_{n+1} + (1-\gamma)\, \dot{u}_n \tag{3.9}$$

$$\ddot{u}_{n+\gamma} = \gamma\, \ddot{u}_{n+1} + (1-\gamma)\, \ddot{u}_n \tag{3.10}$$

$$u_{n+1} = u_n + \Delta t\, \dot{u}_{n+\gamma} \tag{3.11}$$

$$\dot{u}_{n+1} = \dot{u}_n + \Delta t\, \ddot{u}_{n+\gamma} \tag{3.12}$$

where $u_{n+\gamma}$, $\dot{u}_{n+\gamma}$ and $\ddot{u}_{n+\gamma}$ are respectively a scalar variable, its time derivative and its second time derivative at time instant $t_{n+\gamma}$. It can be easily seen from Equations (3.8) to (3.12) that for $\gamma = 1$ the generalised midpoint rule reduces to the backward Euler method, and that for $\gamma = \frac{1}{2}$ it yields to the trapezoidal rule method. It is shown in Section 3.4 that for $\gamma = \frac{1}{2}$ the integration scheme is second order accurate and that for other values of γ the generalised midpoint rule is first order accurate.

3.4 Stability and accuracy

For a better understanding of the stability and accuracy of discrete time integration schemes, a number of linear model problems are considered. The model problems are used to introduce terms as truncation error, of order accuracy and amplification matrix. Also, eigenvalue plots are introduced for presentation of the stability conditions. The model problems considered are a one degree of freedom first order problem, a one degree of freedom second order problem and a two degrees of freedom second order problem.

3.4.1 One degree of freedom first order problem

A first order initial value problem with one degree of freedom is considered. The problem is described by the following equations

$$\dot{u}(t) - \lambda\, u(t) = 0 \tag{3.13}$$

$$u(0) = u_0 \tag{3.14}$$

where $u(t)$ and $\dot{u}(t)$ are a time dependent scalar variable and its time derivative respectively, u_0 is the value of u at time instant $t = 0$ and λ is a model parameter which is assumed to be complex and given as

$$\lambda = -\xi + \mathrm{i}\omega. \tag{3.15}$$

Exact solution: The exact solution for this problem can be written as

$$u(t) = u_0\, e^{\lambda t}. \tag{3.16}$$

In order to compute the values of $u(t)$ at given time instants $t = t_0 + k\Delta t,\ k = 1, 2, ..., N$, a recurrence relation between the values of $u(t)$ at t_{n+1} and t_n can be expressed as

$$u(t_{n+1}) = u(t_n)\, e^{\lambda \Delta t},\ n = 0, 1, 2, ..., N-1. \tag{3.17}$$

Characteristic time period: The characteristic time period of the system depends on the frequency ω and is defined as

$$T = \frac{2\pi}{\omega}. \tag{3.18}$$

Exact amplification factor: To assess the stability and accuracy of the time integration schemes, the numerical amplification factor is compared with the exact amplification factor. The exact amplification factor for this problem is as follows

$$\zeta = \frac{u(t_{n+1})}{u(t_n)} = e^{\lambda \Delta t}. \tag{3.19}$$

Numerical amplification factor: For a numerical solution of the model problem, approximations are needed for $u(t)$ and $\dot{u}(t)$. The generalized midpoint rule, which for given values of γ can be reduced to the backward Euler method or the trapezoidal rule, is used for the approximations. Following the definition in Section 3.3, the generalized midpoint rule for a first order problem can be rewritten as

$$u_{n+\gamma} = \gamma\, u_{n+1} + (1-\gamma)\, u_n \tag{3.20}$$

$$\dot{u}_{n+\gamma} = \frac{1}{\Delta t}\, u_{n+1} - \frac{1}{\Delta t}\, u_n \tag{3.21}$$

which leads to the following discretisation of the problem

$$(\frac{1}{\Delta t}\, u_{n+1} - \frac{1}{\Delta t}\, u_n) - \lambda\, (\gamma\, u_{n+1} + (1-\gamma)\, u_n) = 0. \tag{3.22}$$

The numerical amplification factor ζ^h is defined as follows

$$\zeta^h = \frac{u_{n+1}}{u_n} \tag{3.23}$$

which leads to

$$\zeta^h = \frac{(1 + (1-\gamma)\lambda \Delta t)}{(1 - \gamma \lambda \Delta t)} \tag{3.24}$$

or, after substitution of equation (3.15)

$$\zeta^h = \frac{(1 + (1-\gamma)(-\xi + \mathrm{i}\omega)\Delta t)}{(1 - \gamma(-\xi + \mathrm{i}\omega)\Delta t)}. \tag{3.25}$$

Spectral radius: The stability can be assessed based on the spectral radius ρ^h. For a one degree of freedom first order problem, the spectral radius is defined as the absolute value of the amplification factor ζ^h, which, if the amplification factor ζ^h is assumed to be complex, leads to

$$\rho^h = |\zeta^h| = \sqrt{(\mathrm{Re}(\zeta^h))^2 + (\mathrm{Im}(\zeta^h))^2}. \tag{3.26}$$

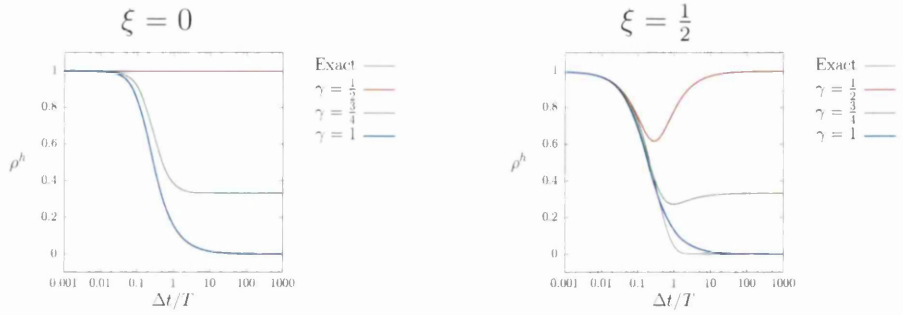

Figure 3.1: Spectral radius for one degree of freedom first order problem discretised with generalised midpoint rule.

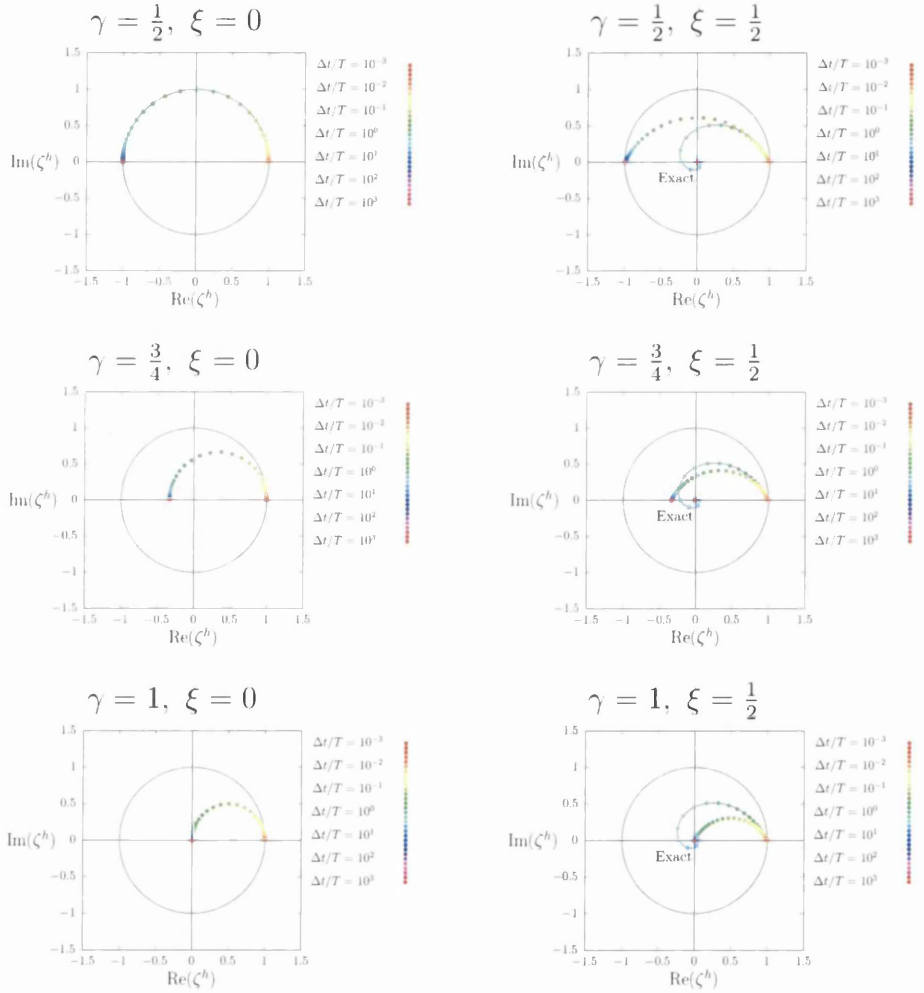

Figure 3.2: Eigenvalues for one degree of freedom first order problem discretised with generalised midpoint rule.

Substitution of Equation (3.25) renders

$$\rho^h = \sqrt{\frac{1 + 2(-1+\gamma)\Delta t\xi + (-1+\gamma)^2\Delta t^2(\xi^2+\omega^2)}{1 + 2\gamma\Delta t\xi + \gamma^2\Delta t^2(\xi^2+\omega^2)}}. \tag{3.27}$$

Stability: For unconditional stability of a time integration scheme it is required that $\rho^h \leq 1$.

For different values of γ the spectral radius ρ^h is compared with the exact spectral radius ρ ($= |\zeta|$), which is shown in Figure 3.1. The spectral radii for $\omega = 1$ and $\xi = 0$ are plotted as a function of $\Delta t/T$. It can be seen that the exact spectral radius and the numerical spectral radius for $\gamma = \frac{1}{2}$ are equal to 1 independent of the time step size Δt. For $\gamma = \frac{3}{4}$ and $\gamma = 1$ numerical damping occurs and a relation between the spectral radius for large time steps and γ can be found

$$\gamma = \frac{1}{1+\rho_\infty^h}. \tag{3.28}$$

This relation is also satisfied in the presence of physical damping, which is shown by plotting the spectral radii for $\omega = 1$ and $\xi = \frac{1}{2}$. The exact spectral radius is no longer equal to one, but now experiences damping and becomes zero for large time steps.

Another way to assess the stability of a time integration scheme is by evaluation of the amplification factor ζ^h for values of $\Delta t/T$ ranging from 10^{-3} to 10^3, by plotting the imaginary parts of the amplification factors against the real parts. The stability requirement stating that $\rho^h \leq 1$ is then represented by a unit circle in the figure. It is straightforward to conclude that if all amplification factors lie within the unit circle, the time integration scheme is unconditionally stable.

Figure 3.2 shows plots for different combinations of time integration parameter γ and model parameter ξ. It can be observed that the generalised midpoint rule is unconditionally stable for all cases. First, the stability plot is shown for $\gamma = \frac{1}{2}$ (trapezoidal rule), $\omega = 1$ and $\xi = 0$ (no physical damping). All amplification factors lie on the unit circle, which means there is no numerical damping. The exact amplification factors lie on the unit circle as well and are therefore not shown in the figure. If there is physical damping the amplification factors are no longer lying on the unit circle as can be seen in the plot where $\gamma = \frac{1}{2}$, $\omega = 1$ and $\xi = \frac{1}{2}$. Both the numerical and the exact amplification factors are shown in the figure. Note that for small and for

large time steps the position of the amplification factors is consistent with their representation in Figure 3.1.

The effect of numerical damping can be observed in the plots for respectively $\gamma = \frac{3}{4}$, $\omega = 1$ and $\xi = 0$ and $\gamma = 1$ (backward Euler), $\omega = 1$ and $\xi = 0$ and the effect of the combination of numerical and physical damping in the plots for respectively $\gamma = \frac{3}{4}$, $\omega = 1$ and $\xi = \frac{1}{2}$ and $\gamma = 1$ (backward Euler), $\omega = 1$ and $\xi = \frac{1}{2}$.

Truncation error: In order to analyse the accuracy of the chosen scheme, the truncation error is derived. The truncation error is defined as (see e.g. [39])

$$u(t_{n+1}) = u_{n+1} + e \tag{3.29}$$

where $u(t_{n+1})$ is the exact value of u at time instant t_{n+1}, u_{n+1} is the approximated value at time instant t_{n+1} and e is the truncation error. To derive e, a Taylor series expansion is performed around the exact and the approximated values.

For the exact value $u(t_{n+1})$ the expression given by Equation (3.17) is expanded, which gives the following result

$$u(t_{n+1}) = u(t_n) + \lambda u(t_n)\ \Delta t + \frac{1}{2}\lambda^2 u(t_n)\ \Delta t^2 + \frac{1}{6}\lambda^3 u(t_n)\ \Delta t^3 + \frac{1}{24}\lambda^4 u(t_n)\ \Delta t^4 + \mathrm{O}[\Delta t^5]. \tag{3.30}$$

The approximation u_{n+1} is derived by a Taylor series expansion of the expression that is given by rearranging Equation (3.22)

$$u_{n+1} = u_n + \lambda u_n\ \Delta t + \gamma\lambda^2 u_n\ \Delta t^2 + \gamma^2\lambda^3 u_n\ \Delta t^3 + \gamma^3\lambda^4 u_n\ \Delta t^4 + \mathrm{O}[\Delta t^5]. \tag{3.31}$$

The truncation error e is obtained by substracting Equation (3.31) from Equation (3.30) and asssuming that $u(t_n) = u_n$ which gives

$$e = \frac{1}{2}(1-2\gamma)\lambda^2 u_n\ \Delta t^2 + \frac{1}{6}(1-6\gamma^2)\lambda^3 u_n\ \Delta t^3 + \frac{1}{24}(1-24\gamma^3)\lambda^4 u_n\ \Delta t^4 + \mathrm{O}[\Delta t^5]. \tag{3.32}$$

This means there is a second order leading truncation error.

Accuracy: The degree of accuracy p of a scheme is defined as follows [39, 40]:

$$u(t_{n+1}) = u_{n+1} + \mathrm{O}[\Delta t^{p+1}] \tag{3.33}$$

where p is the order of accuracy, which means the order of accuracy is one less than the exponent of the time step size in the truncation error. This means that the truncation error is of one order higher than the solution, which shows that when decreasing the time step size the error will reduce faster than the solution increment. For this model problem the generalised midpoint rule is first order accurate, however, when $\gamma = \frac{1}{2}$ (trapezoidal rule) the second order term in the truncation error vanishes, which leaves a third order truncation error and therefore second order accuracy.

Numerical damping: The numerical amplification factor ζ^h can be written in the same form as the exact amplification factor ζ. The exact amplification factor ζ depends on ξ and ω, so analogously the numerical amplification factor ζ^h will be expressed as a function of the numerical equivalents ξ^h and ω^h

$$\zeta^h = e^{\lambda^h \Delta t}, \qquad \lambda^h = -\xi^h + \mathrm{i}\omega^h. \tag{3.34}$$

The amount of numerical damping is defined by the difference between ξ and ξ^h, where based on Equation (3.34) ζ^h can be computed as follows

$$\xi^h = -\frac{1}{\Delta t}\ln(|\zeta^h|) \tag{3.35}$$

which, after a Taylor series expansion, for the model problem leads to

$$\xi^h = \xi - \frac{1}{2}((-1+2\gamma)(\xi^2-\omega^2))\Delta t + \frac{1}{3}(1-3\gamma+3\gamma^2)\xi(\xi^2-2\omega^2)\Delta t^2 + \mathrm{O}[\Delta t^3]. \tag{3.36}$$

This gives first order numerical damping for the generalised midpoint rule and second order numerical damping for the trapezoidal rule in particular.

Numerical dispersion: Numerical dispersion is the difference between ω and ω^h. From Equation (3.34) it can be derived that

$$\omega^h = \frac{1}{\Delta t}\arg(\zeta^h). \tag{3.37}$$

For the model problem this means that ω^h is given as

$$\omega^h = \omega + (1-2\gamma)\xi\omega\Delta t - \frac{1}{3}((1-3\gamma+3\gamma^2)\omega(-3\xi^2+\omega^2))\Delta t^2 + \mathrm{O}[\Delta t^3]. \tag{3.38}$$

Similar to numerical damping, there is first order numerical dispersion for the generalised midpoint rule, which for the trapezoidal rule improves to second order numerical dispersion.

3.4.2 One degree of freedom second order problem

In this section, the stability and accuracy of a second order problem is analysed. There is only one degree of freedom, however the fact that it concerns a second order problem will bring some difficulties when establishing the stability and accuracy as done in the previous section. The problem is described with the following equations

$$\ddot{u}(t) + 2\xi\omega\dot{u}(t) + \omega^2 u(t) = 0 \tag{3.39}$$

$$u(0) = u_0 \tag{3.40}$$

$$\dot{u}(0) = \dot{u}_0 \tag{3.41}$$

where $u(t)$, $\dot{u}(t)$ and $\ddot{u}(t)$ are a time dependent scalar variable, its time derivative and its second time derivative respectively and ω and ξ are the natural frequency and a dimensionless damping ratio respectively. As this is a second order equation, two initial conditions are needed, u_0 is the value of u at time instant $t = 0$ and $\dot{u}_0$ is the time derivative of u at time instant $t = 0$.

Exact solution: The analytical solution can be written as

$$u(t) = e^{-\xi\omega t}\left(u_0 \cos\left(\sqrt{1-\xi^2}\omega t\right) + \frac{\dot{u}_0 + u_0\xi\omega}{\sqrt{1-\xi^2}\omega}\sin\left(\sqrt{1-\xi^2}\omega t\right)\right) \tag{3.42}$$

$$\dot{u}(t) = e^{-\xi\omega t}\left(\frac{\dot{u}_0\sqrt{1-\xi^2}}{\sqrt{1-\xi^2}}\cos\left(\sqrt{1-\xi^2}\omega t\right) - \frac{\dot{u}_0\xi + u_0\omega}{\sqrt{1-\xi^2}\omega}\sin\left(\sqrt{1-\xi^2}\omega t\right)\right) \tag{3.43}$$

A recurrence relation between the values of $u(t)$ and $\dot{u}(t)$ at t_{n+1} and t_n to compute the values of $u(t)$ and $\dot{u}(t)$ at given time instants is then given as

$$u(t_{n+1}) = e^{-\xi\omega\Delta t}\left(u(t_n)\cos\left(\sqrt{1-\xi^2}\omega\Delta t\right) + \frac{\dot{u}(t_n) + u(t_n)\xi\omega}{\sqrt{1-\xi^2}\omega}\sin\left(\sqrt{1-\xi^2}\omega\Delta t\right)\right) \tag{3.44}$$

$$\dot{u}(t_{n+1}) = e^{-\xi\omega\Delta t}\left(\frac{\dot{u}(t_n)\sqrt{1-\xi^2}}{\sqrt{1-\xi^2}}\cos\left(\sqrt{1-\xi^2}\omega\Delta t\right)\right.$$
$$\left. -\frac{\dot{u}(t_n)\xi + u(t_n)\omega}{\sqrt{1-\xi^2}\omega}\sin\left(\sqrt{1-\xi^2}\omega\Delta t\right)\right) \quad (3.45)$$

The characteristic time period of the system is still defined as

$$T = \frac{2\pi}{\omega}. \quad (3.46)$$

Exact amplification factor: For a given time step size Δt, the exact amplification factor is obtained as

$$\zeta = e^{\lambda\Delta t} \quad (3.47)$$

where the factor λ can be found by solving the characteristic equation

$$\lambda^2 + 2\xi\omega\lambda + \omega^2 = 0. \quad (3.48)$$

This results in

$$\lambda_{1,2} = \omega\left(-\xi \pm \sqrt{\xi^2 - 1}\right) \quad (3.49)$$

Amplification matrix: To solve this model problem with the generalised midpoint rule, a formulation of the generalised midpoint rule for second order problems (see Section 3.3) is rewritten as

$$u_{n+\gamma} = \gamma\, u_{n+1} + (1-\gamma)\, u_n \quad (3.50)$$
$$\dot{u}_{n+\gamma} = \frac{1}{\Delta t}\, u_{n+1} - \frac{1}{\Delta t}\, u_n \quad (3.51)$$
$$\ddot{u}_{n+\gamma} = \frac{1}{\gamma\Delta t^2}\, u_{n+1} - \frac{1}{\gamma\Delta t^2}\, u_n - \frac{1}{\gamma\Delta t}\, \dot{u}_n. \quad (3.52)$$

The discretisation of the problem then reads

$$\left(\frac{1}{\gamma\Delta t^2}\, u_{n+1} - \frac{1}{\gamma\Delta t^2}\, u_n - \frac{1}{\gamma\Delta t}\, \dot{u}_n\right) + 2\xi\omega\left(\frac{1}{\Delta t}\, u_{n+1} - \frac{1}{\Delta t}\, u_n\right)$$
$$+ \omega^2(\gamma\, u_{n+1} + (1-\gamma)\, u_n) = 0 \quad (3.53)$$

It can be seen that to calculate u_{n+1}, not just u_n but also $\dot{u}_n$ is needed. It is therefore no longer possible to derive the numerical amplification factor ζ^h by just rearranging the discretised form of the problem. Instead an amplification matrix $\mathbf{A}$ will be derived. Multiplication of the amplification matrix by u_n

and $\dot{u}_n$ leads to u_{n+1} and $\dot{u}_{n+1}$. In order to derive the amplification matrix $\mathbf{A}$, an expression for $\dot{u}_{n+1}$ is needed from the formulation of the generalised midpoint rule

$$\dot{u}_{n+1} = \frac{1}{\gamma \Delta t} u_{n+1} - \frac{1}{\gamma \Delta t} u_n - \frac{(1-\gamma)}{\gamma} \dot{u}_n \tag{3.54}$$

This then leads to the following two equations:

$$\left\{ \begin{array}{c} u_{n+1} \\ \Delta t \dot{u}_{n+1} \end{array} \right\} = \mathbf{A} \left\{ \begin{array}{c} u_n \\ \Delta t \dot{u}_n \end{array} \right\} \tag{3.55}$$

where the amplification matrix $\mathbf{A}$ is given as

$$\mathbf{A} = \begin{bmatrix} 1 - \dfrac{\gamma \Delta t^2 \omega^2}{1 + 2\gamma \Delta t \xi \omega + \gamma^2 \Delta t^2 \omega^2} & \dfrac{1}{1 + 2\gamma \Delta t \xi \omega + \gamma^2 \Delta t^2 \omega^2} \\ -\dfrac{\Delta t^2 \omega}{1 + 2\gamma \Delta t \xi \omega + \gamma^2 \Delta t^2 \omega^2} & \dfrac{1 + 2(-1+\gamma)\Delta t \xi \omega + (-1+\gamma)\gamma \Delta t^2 \omega^2}{1 + 2\gamma \Delta t \xi \omega + \gamma^2 \Delta t^2 \omega^2} \end{bmatrix}. \tag{3.56}$$

Spectral radius: To get the spectral radius ρ^h that is needed to assess the stability of the time integration scheme, the eigenvalues of the amplification matrix are computed by solving

$$\mathrm{P}(\zeta^h) = \det(\mathbf{A} - \zeta^h \mathbf{I}) = 0. \tag{3.57}$$

For a $n \times n$ matrix $\mathbf{A}$, this equation is a polynomial of degree n in ζ^h and is called the characteristic equation of $\mathbf{A}$. The characteristic polynomial for this amplification matrix $\mathbf{A}$ is as follows

$$\begin{aligned} \mathrm{P}(\zeta^h) = & \frac{1 + 2(-1+\gamma)\Delta t \xi \omega + (-1+\gamma)^2 \Delta t^2 \omega^2}{1 + 2\gamma \Delta t \xi \omega + \gamma^2 \Delta^2 \omega^2} \\ & - \frac{2(1 + (-1+2\gamma)\Delta t \xi \omega + (-1+\gamma)\gamma \Delta t^2 \omega^2)}{1 + 2\gamma \Delta t \xi \omega + \gamma^2 \Delta t^2 \omega^2} \zeta^h + (\zeta^h)^2 \end{aligned} \tag{3.58}$$

As a polynomial of degree n has a maximum of n distinct roots, a $n \times n$ matrix has a maximum of n distinct eigenvalues. In this case it concerns a 2×2 amplification matrix, so there are two eigenvalues. The eigenvalues are used to derive the spectral radius ρ^h. As there are two eigenvalues, the spectral radius ρ^h is defined to be equal to the largest of the absolute eigenvalues

$$\rho^h = \max(|\zeta^h_{1,2}|) \tag{3.59}$$

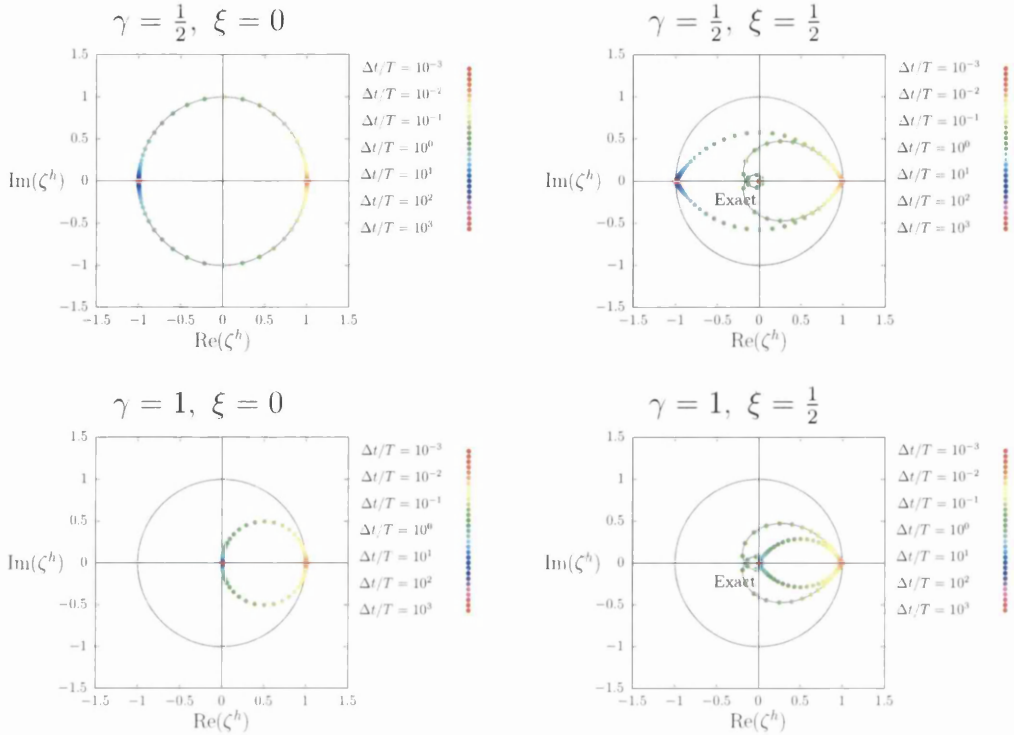

Figure 3.3: Eigenvalues for one degree of freedom second order problem discretised with generalised midpoint rule.

where $\zeta^h_{1,2}$ are the eigenvalues of the amplification matrix, which for the given amplification matrix are

$$\zeta^h_1 = \frac{1 - \Delta t\xi\omega + 2\gamma\Delta t\xi\omega - \gamma\Delta t^2\omega^2 + \gamma^2\Delta t^2\omega^2 - \sqrt{-\Delta t^2\omega^2 + \Delta t^2\xi^2\omega^2}}{1 + 2\gamma\Delta t\xi\omega + \gamma^2\Delta t^2\omega^2} \tag{3.60}$$

$$\zeta^h_2 = \frac{1 - \Delta t\xi\omega + 2\gamma\Delta t\xi\omega - \gamma\Delta t^2\omega^2 + \gamma^2\Delta t^2\omega^2 + \sqrt{-\Delta t^2\omega^2 + \Delta t^2\xi^2\omega^2}}{1 + 2\gamma\Delta t\xi\omega + \gamma^2\Delta t^2\omega^2} \tag{3.61}$$

Stability: The stability requirement is still valid, which means that the largest of the absolute eigenvalues has to be equal or smaller than 1.

To determine whether this requirement holds for a given range of time step sizes the eigenvalues are plotted. Both eigenvalues will be plotted in the same figure for a range of values for $\Delta t/T$, as can be seen in Figure 3.3. Again the imaginary parts of the eigenvalues are plotted against the real parts. When comparing Figure 3.3 with Figure 3.2, it can be seen that one

of the two eigenvalues follows the same pattern as the amplification factor in the previous section. The other eigenvalue is the negative equivalent. Both eigenvalues satisfy the stability requirement and thus, again, it is shown that the generalised midpoint rule is unconditionally stable.

For the cases with damping the exact amplification factor is shown again too, which allows for comparison of the amount of damping between the exact amplification factor and the numerical amplification factor for different values of γ.

Truncation error: To derive the truncation error e, the numerical solution is again compared with the exact solution. As the scalar variable $u(t)$ and its time derivative $\dot{u}(t)$ depend on each other (see Equations (3.42) and (3.43)), an error in one of them will affect the accuracy of the other. It is therefore important to look at the truncation errors for both $u(t)$ and $\dot{u}(t)$, respectively denoted by e_u and $e_{\dot{u}}$.

For the exact solution a Taylor series expansion is performed around $u(t_{n+1})$ and $\dot{u}(t_{n+1})$, as given by Equations (3.44) and (3.45)

$$u(t_{n+1}) = u(t_n) + \dot{u}(t_n)\ \Delta t - \frac{1}{2}(\omega(2\dot{u}(t_n)\xi + u(t_n)\omega))\ \Delta t^2 + \frac{1}{6}\omega^2(\dot{u}(t_n)(-1+4\xi^2) + 2u(t_n)\xi\omega)\ \Delta t^3 + \mathrm{O}[\Delta t^4] \quad (3.62)$$

$$\dot{u}(t_{n+1}) = \dot{u}(t_n) - \omega(2\dot{u}(t_n)\xi + u(t_n)\omega)\ \Delta t + \frac{1}{2}\omega^2(\dot{u}(t_n)(-1+4\xi^2) + 2u(t_n)\xi\omega)\ \Delta t^2 + \frac{1}{6}\omega^3(4\dot{u}(t_n)\xi - 8\dot{u}(t_n)\xi^3 + u(t_n)\omega - 4u(t_n)\xi^2\omega)\ \Delta t^3 + \mathrm{O}[\Delta t^4]. \quad (3.63)$$

And for the numerical solution, the expressions for u_{n+1} and $\dot{u}_{n+1}$ as given in Equations (3.53) and (3.54) are expanded

$$u_{n+1} = u_n + \dot{u}_n\ \Delta t - \gamma\omega(2\dot{u}_n\xi + u_n\omega)\ \Delta t^2 + \gamma^2\omega^2(\dot{u}_n(-1+4\xi^2) + 2u_n\xi\omega)\ \Delta t^3 + \mathrm{O}[\Delta t^4] \quad (3.64)$$

$$\dot{u}_{n+1} = \dot{u}_n - \omega(2\dot{x}_n\xi + u_n\omega)\ \Delta t + \gamma\omega^2(\dot{u}_n(-1+4\xi^2) + 2u_n\xi\omega)\ \Delta t^2 + \gamma^2\omega^3(4\dot{u}_n\xi - 8\dot{u}_n\xi^3 + u_n\omega - 4u_n\xi^2\omega)\ \Delta t^3 + \mathrm{O}[\Delta t^4]. \quad (3.65)$$

This gives for the truncation errors e_u and $e_{\dot{u}}$, assuming that $u(t_n) = u_n$, the following

$$e_u = \frac{1}{2}(-1+2\gamma)\omega(2\dot{u}_n\xi + u_n\omega)\ \Delta t^2 + \frac{1}{6}(1-6\gamma^2)\omega^2(\dot{u}_n(-1+4\xi^2) + 2u_n\xi\omega)\ \Delta t^3 + \mathrm{O}[\Delta t^4] \quad (3.66)$$

$$e_{\dot{u}} = \frac{1}{2}(1-2\gamma)\omega^2(\dot{u}_n(-1+4\xi^2) + 2u_n\xi\omega)\ \Delta t^2 + \frac{1}{6}(1-6\gamma^2)\omega^3(4\dot{u}_n\xi - 8\dot{u}_n\xi^3 + u_n\omega - 4u_n\xi^2\omega)\ \Delta t^3 + \mathrm{O}[\Delta t^4]. \quad (3.67)$$

For both truncation errors again a second order leading truncation error is derived, which results in first order accuracy for the general form of the generalised midpoint rule and second order accuracy for the trapezoidal rule.

Numerical damping: To derive the amount of numerical damping the absolute value of the complex amplification factors $\zeta^h_{1,2}$ is needed. From Equations (3.60) and (3.61) it can be seen that the real and imaginary parts of the amplification factors depend on the values for ξ, ω and Δt. Since ξ, ω and Δt are all positive, it is found that the real and imaginary part depend only on whether ξ is smaller or larger than 1. Here, only the undercritically damped system ($\xi < 1$) is considered which gives the following real and imaginary parts of the amplification factor ζ^h

$$\mathrm{Re}(\zeta^h_{1,2}) = \frac{2(1+(-1+2\gamma)\Delta t\xi\omega + (-1+\gamma)\gamma\Delta t^2\omega^2)}{2(1+2\gamma\Delta t\xi\omega + \gamma^2\Delta t^2\omega^2)} \quad (3.68)$$

$$\mathrm{Im}(\zeta^h_{1,2}) = \frac{\pm 2\sqrt{\Delta t^2\omega^2 - \Delta t^2\xi^2\omega^2}}{2(1+2\gamma\Delta t\xi\omega + \gamma^2\Delta t^2\omega^2)} \quad (3.69)$$

Based on the expression for $\lambda_{1,2}$ given by Equation (3.49), the numerical equivalent is now given as

$$\lambda^h_{1,2} = \omega^h\left(-\xi^h \pm \sqrt{(\xi^h)^2 - 1}\right) \quad (3.70)$$

which for the numerical damping factor ξ^h leads to

$$\xi^h = -\frac{1}{\omega\Delta t}\ln(|\zeta^h|). \quad (3.71)$$

The amount of numerical damping ξ^h can be calculated for either of the two eigenvalues $\zeta_{1,2}^h$ as they both have the same absolute value. It follows that the amount of numerical damping can be expressed as follows

$$\xi^h = \xi - \frac{1}{2}((-1+\gamma)(-1+2\xi^2)\omega)\ \Delta t + \frac{1}{3}(1-3\gamma+3\gamma^2)\xi(-3+4\xi^2)\omega^2\Delta t^2 - \frac{1}{4}((-1+4\gamma-6\gamma^2+4\gamma^3)(1-8\xi^2+8\xi^4)\omega^3)\ \Delta t^3 + \mathrm{O}[\Delta t^4]. \quad (3.72)$$

As in the previous section is it found that there is first order numerical damping for the generalised midpoint rule and second order numerical damping for the trapezoidal rule in particular.

Numerical dispersion: Using the same formulations for the real and imaginary parts of ζ^h the numerical dispersion ω^h can be found by computing

$$\omega^h = \frac{1}{\pm\sqrt{\xi^2-1}\Delta t}\arg(\zeta^h). \quad (3.73)$$

This leads to

$$\omega_{1,2}^h = \omega - (-1+2\gamma)\xi\omega^2\ \Delta t + \frac{1}{3}((1-3\gamma+3\gamma^2)(-1+4\xi^2)\omega^3)\ \Delta t^2 - (-1+4\gamma-6\gamma^2+4\gamma^3)\xi(-1+2\xi^2)\omega^3\ \Delta t^3 + \mathrm{O}[\Delta t^4] \quad (3.74)$$

which again leads to first order numerical dispersion for the generalised midpoint rule and second order numerical dispersion for the trapezoidal rule.

3.4.3 Two degrees of freedom second order problem

The next problem has two degrees of freedom and is a second order problem. This problem is described with the following set of equations, given in matrix form

$$\mathbf{M}\ddot{\mathbf{u}}(t) + \mathbf{D}\dot{\mathbf{u}}(t) + \mathbf{K}\mathbf{u}(t) = \mathbf{0} \quad (3.75)$$

with

$$\ddot{\mathbf{u}}(t) = \begin{Bmatrix} \ddot{x}(t) \\ \ddot{y}(t) \end{Bmatrix} \qquad \dot{\mathbf{u}}(t) = \begin{Bmatrix} \dot{x}(t) \\ \dot{y}(t) \end{Bmatrix} \qquad \mathbf{u}(t) = \begin{Bmatrix} x(t) \\ y(t) \end{Bmatrix} \quad (3.76)$$

$$\mathbf{M} = \begin{bmatrix} m_1 & 0 \\ 0 & m_2 \end{bmatrix} \qquad \mathbf{D} = \begin{bmatrix} d_1 & -d_1 \\ -d_1 & d_1+d_2 \end{bmatrix} \qquad \mathbf{K} = \begin{bmatrix} k_1 & -k_1 \\ -k_1 & k_1+k_2 \end{bmatrix} \quad (3.77)$$

$$x(0) = x_0 \tag{3.78}$$
$$\dot{x}(0) = \dot{x}_0 \tag{3.79}$$
$$y(0) = y_0 \tag{3.80}$$
$$\dot{y}(0) = \dot{y}_0 \tag{3.81}$$

where $x(t)$ and $y(t)$ are two time dependent scalar variables, $\dot{x}(t)$ and $\dot{y}(t)$ are their respective time derivatives, $\ddot{x}(t)$ and $\ddot{y}(t)$ are their respective second derivatives in time and m_1, m_2, d_1, d_2, k_1 and k_2 are model parameters. For a second order problem with two degrees of freedom, four initial conditions are needed. In this case x_0 is the value of x at time instant $t = 0$, $\dot{x}_0$ is the time derivative of x at time instant $t = 0$, y_0 is the value of y at time instant $t = 0$ and $\dot{y}_0$ is the time derivative of y at time instant $t = 0$.

Exact solution: To get an analytical solution for Equation (3.75), first the eigenvalues $\zeta_{1,2}$ and eigenvectors $\varphi_{1,2}$ of the undamped system ($\mathbf{D} = \mathbf{0}$) are derived. The eigenvalues $\zeta_{1,2}$ are calculated by solving

$$\det(\mathbf{M}^{-1}\mathbf{K} - \zeta\mathbf{I}) = 0 \tag{3.82}$$

From the eigenvalues $\zeta_{1,2}$ the natural frequencies $\omega_{1,2}$ can be derived

$$\omega_{1,2} = \sqrt{\zeta_{1,2}} \tag{3.83}$$

which gives

$$\omega_{1,2} = \frac{1}{\sqrt{2}}\sqrt{\frac{k_2m_1 + k_1(m_1 + m_2) \pm \sqrt{-4k_1k_2m_1m_2 + (k_2m_1 + k_1(m_1 + m_2))^2}}{m_1m_2}}. \tag{3.84}$$

The eigenvectors $\varphi_{1,2}$ corresponding to eigenvalues $\zeta_{1,2}$ denote the modal shapes or modes of vibration of the system and are given as

$$\varphi_{1,2} = \left\{ \begin{array}{c} k_1m_1 + k_2m_1 + k_1m_2 \pm \sqrt{-4k_1k_2m_1m_2 + (k_2m_1 + k_1(m_1 + m_2))^2} \\ 2k_1m_1 \end{array} \right\}. \tag{3.85}$$

Due to the characteristic properties of the modes of vibration of a dynamical system, the solution vector $\mathbf{u}(t)$ can be written as a linear combination of the modal shapes

$$\mathbf{u}(t) = \boldsymbol{\phi}\mathbf{v}(t) \tag{3.86}$$

where the colums of matrix $\boldsymbol{\phi}$ are given by the modal shapes $\varphi_{1,2}$ and $\mathbf{v}(t)$ is given as

$$\mathbf{v}(t) = \left\{ \begin{array}{c} p(t) \\ q(t) \end{array} \right\}. \tag{3.87}$$

The scalar variables $p(t)$ and $q(t)$ can be obtained by substituting Equation (3.86) into Equation (3.75) which leads to

$$m_1^*\ddot{p}(t) + d_1^*\dot{p}(t) + k_1^* p(t) = 0 \tag{3.88}$$

$$m_2^*\ddot{q}(t) + d_2^*\dot{q}(t) + k_2^* q(t) = 0 \tag{3.89}$$

where

$$m_1^* = \varphi_1^T \mathbf{M}\varphi_1, \qquad d_1^* = \varphi_1^T \mathbf{D}\varphi_1, \qquad k_1^* = \varphi_1^T \mathbf{K}\varphi_1, \tag{3.90}$$

$$m_2^* = \varphi_2^T \mathbf{M}\varphi_2, \qquad d_2^* = \varphi_2^T \mathbf{D}\varphi_2, \qquad k_2^* = \varphi_2^T \mathbf{K}\varphi_2. \tag{3.91}$$

The expressions for m_1^*, m_2^*, d_1^*, d_2^*, k_1^* and k_2^* in terms of m_1, m_2, d_1, d_2, k_1 and k_2 are rather lengthy and therefore not given. Equations (3.88) and (3.89) may be rewritten as

$$\ddot{p}(t) + 2\xi_1\omega_1\dot{p}(t) + \omega_1^2 p(t) = 0 \tag{3.92}$$

$$\ddot{q}(t) + 2\xi_2\omega_2\dot{q}(t) + \omega_2^2 q(t) = 0 \tag{3.93}$$

where

$$\omega_1 = \sqrt{\frac{k_1^*}{m_1^*}}, \qquad \xi_1 = \frac{c_1^*}{2m_1^*\omega_1}, \tag{3.94}$$

$$\omega_2 = \sqrt{\frac{k_2^*}{m_2^*}}, \qquad \xi_2 = \frac{c_2^*}{2m_2^*\omega_2}. \tag{3.95}$$

The expressions for ω_1, ω_2, ξ_1 and ξ_2 are again not given due to their length.

Based on Equations (3.92) and (3.93) it is straightforward to express the general form for the solution of equation (3.86)

$$\mathbf{u}(t) = \phi \left\{ \begin{array}{l} e^{-\xi_1\omega_1 t}\left(A\cos\left(\sqrt{1-\xi_1^2}\omega_1 t\right) + B\sin\left(\sqrt{1-\xi_1^2}\omega_1 t\right)\right) \\ e^{-\xi_2\omega_2 t}\left(C\cos\left(\sqrt{1-\xi_2^2}\omega_2 t\right) + D\sin\left(\sqrt{1-\xi_2^2}\omega_2 t\right)\right) \end{array} \right\}. \tag{3.96}$$

For the given initial values the expressions for A, B, C and D can be derived, which is done using a symbolic toolbox.

Characteristic time period: As the model problem now has two natural frequencies $\omega_{1,2}$, there will also be two characteristic time periods. When solving a system with a harmonic response, the time step size should be small enough to capture the highest frequency and therefore the characteristic time period that is used in this section is the smallest one

$$T = \frac{2\pi}{\max(\omega_{1,2})}. \tag{3.97}$$

Amplification matrix: The total set of equations that is needed to derive the amplification matrix that describes the problem when solved with the generalised midpoint rule is as follows

$$\mathbf{u}_{n+\gamma} = \gamma\,\mathbf{u}_{n+1} + (1-\gamma)\,\mathbf{u}_n \tag{3.98}$$

$$\dot{\mathbf{u}}_{n+\gamma} = \frac{1}{\Delta t}\,\mathbf{u}_{n+1} - \frac{1}{\Delta t}\,\mathbf{u}_n \tag{3.99}$$

$$\ddot{\mathbf{u}}_{n+\gamma} = \frac{1}{\gamma\Delta t^2}\,\mathbf{u}_{n+1} - \frac{1}{\gamma\Delta t^2}\,\mathbf{u}_n - \frac{1}{\gamma\Delta t}\,\dot{\mathbf{u}}_n \tag{3.100}$$

$$\dot{\mathbf{u}}_{n+1} = \frac{1}{\gamma\Delta t}\mathbf{u}_{n+1} - \frac{1}{\gamma\Delta t}\mathbf{u}_n - \frac{(1-\gamma)}{\gamma}\dot{\mathbf{u}}_n. \tag{3.101}$$

This leads to the following set of discretised equations

$$\mathbf{M}\left(\frac{1}{\gamma\Delta t^2}\,\mathbf{u}_{n+1} - \frac{1}{\gamma\Delta t^2}\,\mathbf{u}_n - \frac{1}{\gamma\Delta t}\,\dot{\mathbf{u}}_n\right) + \mathbf{D}\left(\frac{1}{\Delta t}\,\mathbf{u}_{n+1} - \frac{1}{\Delta t}\,\mathbf{u}_n\right) + \mathbf{K}(\gamma\,\mathbf{u}_{n+1} + (1-\gamma)\,\mathbf{u}_n) = \mathbf{0} \tag{3.102}$$

The resulting amplification matrix is defined as

$$\begin{Bmatrix} \mathbf{u}_{n+1} \\ \Delta t\dot{\mathbf{u}}_{n+1} \end{Bmatrix} = \mathbf{A} \begin{Bmatrix} \mathbf{u}_n \\ \Delta t\dot{\mathbf{u}}_n \end{Bmatrix}. \tag{3.103}$$

The 4×4 amplification matrix $\mathbf{A}$ consists of long expressions which are not given here. Similar to the previous section, the characteristic polynomial of the amplification matrix is derived and the eigenvalues are computed. The characteristic polynomial is a 4^{th} order polynomial so there will be 4 distinct eigenvalues. The eigenvalues are plotted for a range of time step sizes and for $m_1 = 1$, $m_2 = 2$, $k_1 = 1$ and $k_2 = 1$ in Figure 3.4 for different values of γ, d_1 and d_2. Again it can be seen that for all eigenvalues the generalised midpoint rule is unconditionally stable.

Truncation error: Analogously to the previous section the truncation errors e_x, $e_{\dot{x}}$, e_y and $e_{\dot{y}}$ can be derived. Here, only the leading truncation errors are given.

$$e_x = -\frac{(d_1(\dot{x}_n - \dot{y}_n) + k_1(x_n - y_n))(-1+2\gamma)}{2m_1}\,\Delta t^2 + \mathrm{O}[\Delta t^3] \tag{3.104}$$

$$e_{\dot{x}} = \left(\left((-\dot{x}_n + \dot{y}_n)k_1m_1m_2 + d_1^2(\dot{x}_n - \dot{y}_n)(m_1+m_1) - d_1\left(d_2\dot{y}_nm_1 - k_1(m_1+m_2)(x_n - y_n) + k_2m_1y_n\right)\right)(-1+2\gamma)\right) / \left(2m_1^2m_2\right)\,\Delta t^2 + \mathrm{O}[\Delta t^3] \tag{3.105}$$

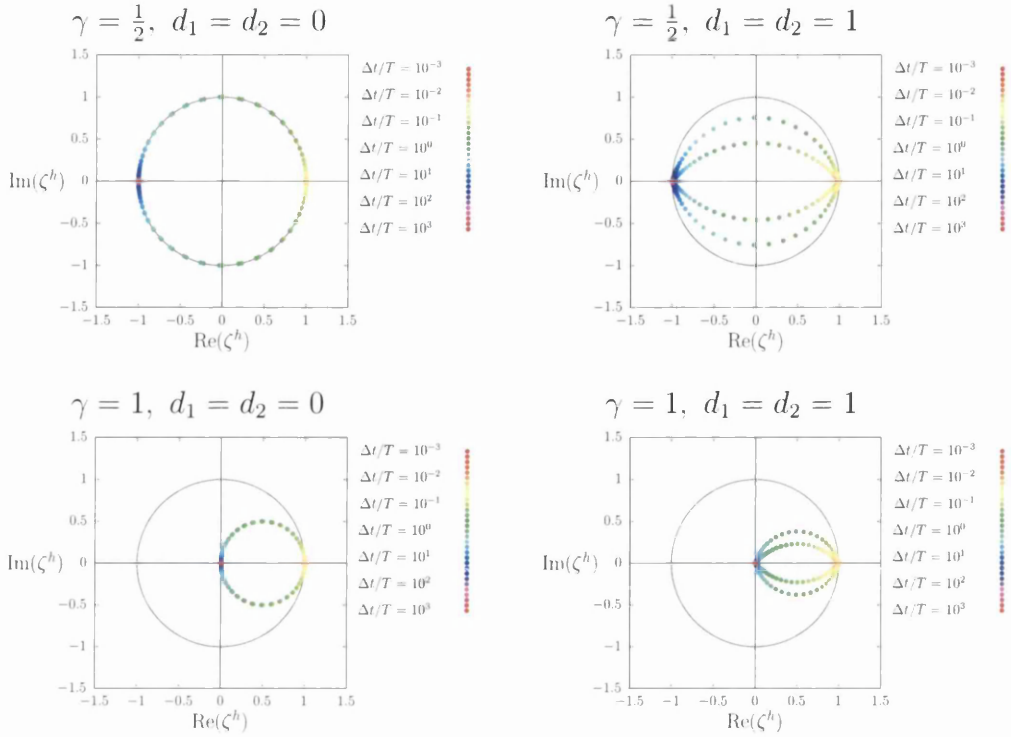

Figure 3.4: Eigenvalues for two degrees of freedom second order problem discretised with generalised midpoint rule.

$$e_y = \frac{(d_1(\dot{x}_n - \dot{y}_n) - d_2\dot{y}_n + k_1x_n - k_1y_n - k_2y_n)(-1+2\gamma)}{2m_2}\,\Delta t^2 + \mathrm{O}[\Delta t^3] \tag{3.106}$$

$$\begin{aligned} e_{\dot{y}} = &-\big(\big(d_1^2(\dot{x}_n - \dot{y}_n)(m_1+m_2) + d_1\,(d_2(\dot{x}_n - 2\dot{y}_n)m_1 \\ &+k_1(m_1+m_2)(x_n - y_n) - k_2m_1y_n) - m_1(d_2^2\dot{y}_n + (\dot{x}_nk_1 - \dot{y}_n(k_1+k_2))m_2 \\ &+d_2(k_2y_n + k_1(-x_n + y_n))))\,(-1+2\gamma)\big) \,/\, \big(2m_1m_2^2\big)\ \Delta t^2 + \mathrm{O}[\Delta t^3] \end{aligned} \tag{3.107}$$

For all truncation errors e_x, $e_{\dot{x}}$, e_y and $e_{\dot{y}}$ the leading term is of order 2, i.e. first order accuracy. Also, it can be seen that all leading truncation errors disappear when $\gamma = \frac{1}{2}$, leaving the trapezoidal rule to be second order accurate.

The investigation of numerical damping and numerical dispersion is rather tedious due to the complexity of the expressions and is therefore omitted.

3.5 Generalised-α method

The generalised-α method was first proposed by Chung and Hulbert [37]. The method allows the user to control numerical damping and makes it possible to achieve high-frequency dissipation while minimising unwanted low-frequency dissipation. For a given set of time integration scheme parameters the generalised-α method is unconditionally stable and second order accurate. For second order problems these parameters are derived by Chung and Hulbert [37], while Jansen et al [38] have derived the conditions for first order problems.

3.5.1 Generalised-α method for first order problems

To control numerical damping, the unknown variable and its time derivatives are evaluated at different time instants and accordingly interpolated. The generalised-α method for first order problems is defined as follows

$$u_{n+\alpha_f} = \alpha_f\, u_{n+1} + (1-\alpha_f)\, u_n \tag{3.108}$$

$$\dot{u}_{n+\alpha_m} = \alpha_m\, \dot{u}_{n+1} + (1-\alpha_m)\, \dot{u}_n \tag{3.109}$$

$$u_{n+1} = u_n + \Delta t\,((1-\gamma)\,\dot{u}_n + \gamma\,\dot{u}_{n+1})\,. \tag{3.110}$$

The quantities $\dot{u}_{n+\alpha_m}$ and $u_{n+\alpha_f}$ are associated with the time instants $t_{n+\alpha_m}$ and $t_{n+\alpha_f}$ respectively. In order to ensure unconditional stability and second order accuracy the time integration parameters α_f, α_m and γ need to satisfy certain conditions. The first order model problem, introduced in Section 3.4.1, is used to derive the parameters. The discretised form of Equation (3.13) becomes

$$\dot{u}_{n+\alpha_m} - \lambda\, u_{n+\alpha_f} = 0. \tag{3.111}$$

Due to the nature of the generalised-α method formulation, it is not possible to derive a numerical amplification factor for this problem like it was done for the generalised midpoint rule in Section 3.4.1. Therefore, instead of an amplification factor, the amplification matrix $\mathbf{A}$ is derived

$$\begin{Bmatrix} u_{n+1} \\ \Delta t\dot{u}_{n+1} \end{Bmatrix} = \mathbf{A} \begin{Bmatrix} u_n \\ \Delta t\dot{u}_n \end{Bmatrix} \tag{3.112}$$

with

$$\mathbf{A} = \begin{bmatrix} \dfrac{\alpha_m - (-1+\alpha_f)\gamma\Delta t\lambda}{\alpha_m - \alpha_f\gamma\Delta t\lambda} & \dfrac{\alpha_m - \gamma}{\alpha_m - \alpha_f\gamma\Delta t\lambda} \\ \dfrac{\Delta t\lambda}{\alpha_m - \alpha_f\gamma\Delta t\lambda} & \dfrac{-1+\alpha_m - \alpha_f(-1+\gamma)\Delta t\lambda}{\alpha_m - \alpha_f\gamma\Delta t\lambda} \end{bmatrix}. \tag{3.113}$$

Due to the fact that the exact solution $u(t_{n+1})$ only depends on $u(t_n)$, but that the numerical solution u_{n+1} depends on both u_n and $\dot{u}_n$, it is no longer possible to calculate the truncation error e as it was done in Section 3.4.1. Another method to establish the accuracy of this system is therefore needed.

For that reason expressions for u_{n+2} and $\dot{u}_{n+2}$ are derived using amplification matrix $\mathbf{A}$, which together with the expressions for u_{n+1} and $\dot{u}_{n+1}$ as given Equation (3.112) are rearranged in such a way that the time derivatives $\dot{u}_{n+2}$, $\dot{u}_{n+1}$ and $\dot{u}_n$ are eliminated. This leads to the following expression for u_{n+2}

$$u_{n+2} = \frac{-1 + 2\alpha_m + \alpha_f(1-2\gamma)\Delta t\lambda + \gamma\Delta t\lambda}{\alpha_m - \alpha_f\gamma\Delta t\lambda}\, u_{n+1} - \frac{-1 + \alpha_m + (-1 + \alpha_f + \gamma - \alpha_f\gamma)\Delta t\lambda}{\alpha_m - \alpha_f\gamma\Delta t\lambda}\, u_n, \quad (3.114)$$

which can be written as

$$P = u_{n+2} - \frac{-1 + 2\alpha_m + \alpha_f(1-2\gamma)\Delta t\lambda + \gamma\Delta t\lambda}{\alpha_m - \alpha_f\gamma\Delta t\lambda}\, u_{n+1} + \frac{-1 + \alpha_m + (-1 + \alpha_f + \gamma - \alpha_f\gamma)\Delta t\lambda}{\alpha_m - \alpha_f\gamma\Delta t\lambda}\, u_n. \quad (3.115)$$

From Section 3.4.1 it is recalled that the exact solution for this problem is given as

$$u(t_n) = e^{\lambda\Delta t}\, u(t_{n-1}) \quad (3.116)$$

which gives a recurrence relation that can be simply repeated to obtain the following expressions for $u(t_{n+1})$ and $u(t_{n+2})$

$$u(t_{n+1}) = e^{2\lambda\Delta t}\, u(t_{n-1}) \quad (3.117)$$

$$u(t_{n+2}) = e^{3\lambda\Delta t}\, u(t_{n-1}). \quad (3.118)$$

If Equation (3.114) would be the exact representation of the solution, then substitution of Equations (3.116), (3.117) and (3.118) into Equation (3.115) would give zero. If not, then an error can be derived, for which the leading term is of one order higher than the accuracy. Substitution of Equations (3.116), (3.117) and (3.118) into Equation (3.115), where $u_{n+2} = u(t_{n+2})$, $u_{n+1} = u(t_{n+1})$, $u_n = u(t_n)$ and and $u_{n-1} = u(t_{n-1})$, gives

$$e_P^* = \frac{(1 - 2\alpha_f + 2\alpha_m - 2\gamma)\lambda^2 u_{n-1}}{2\alpha_m}\, \Delta t^2 + \frac{(12\alpha_m^2 + \alpha_m(4 - 9\alpha_f - 9\gamma) - 3\alpha_f\gamma(-1 + 2\alpha_f + 2\gamma))\lambda^3 u_{n-1}}{6\alpha_m^2}\, \Delta t^3 + \mathrm{O}[\Delta t^4]. \quad (3.119)$$

From Equation (3.119) it follows that the generalised-α method for first order problems is second order accurate when

$$\gamma = \frac{1}{2} + \alpha_m - \alpha_f. \tag{3.120}$$

To assess the stability of the generalised-α method for first order problems, the eigenvalues of amplification matrix $\mathbf{A}$ are computed. The eigenvalues $\zeta_{1,2}$ are given by

$$\zeta_1 = \left(-1 + 2\alpha_m + \alpha_f\Delta t\lambda + \gamma\Delta t\lambda - 2\alpha_f\gamma\Delta t\lambda - \left(4\alpha_m\Delta t\lambda + \alpha_f^2\Delta t^2\lambda^2 + (-1+\gamma\Delta t\lambda)^2 - 2\alpha_f\Delta t\lambda(1+\gamma\Delta t\lambda)\right)^{1/2}\right) / \left(2(\alpha_m - \alpha_f\gamma\Delta t\lambda)\right) \tag{3.121}$$

$$\zeta_2 = \left(-1 + 2\alpha_m + \alpha_f\Delta t\lambda + \gamma\Delta t\lambda - 2\alpha_f\gamma\Delta t\lambda + \left(4\alpha_m\Delta t\lambda + \alpha_f^2\Delta t^2\lambda^2 + (-1+\gamma\Delta t\lambda)^2 - 2\alpha_f\Delta t\lambda(1+\gamma\Delta t\lambda)\right)^{1/2}\right) / \left(2(\alpha_m - \alpha_f\gamma\Delta t\lambda)\right). \tag{3.122}$$

Based on the stability requirement that the absolute value of both eigenvalues has to be less or equal than one, the stability criteria for α_m and α_f can be derived. As the expressions for ζ_1 and ζ_2 are fairly complicated, the eigenvalues for $\Delta t \to 0$ and $\Delta t \to \infty$ are evaluated. The limits of the eigenvalues ζ_1 and ζ_2 when $\Delta t \to 0$ (after substitution of Equation (3.120) are as follows

$$\lim_{\Delta t\to 0} \zeta_1 = 1 - \frac{1}{\alpha_m} \tag{3.123}$$

$$\lim_{\Delta t\to 0} \zeta_2 = 1. \tag{3.124}$$

For unconditional stability it is required that $|1 - \frac{1}{\alpha_m}| \leq 1$, which leads to the following criterion for α_m

$$\alpha_m \geq \frac{1}{2}. \tag{3.125}$$

For large time step sizes (assuming that $\Delta t\lambda \to \infty$) the following limits are obtained

$$\lim_{\Delta t\lambda\to\infty} \zeta_1 = \frac{1 + 2\alpha_f - 2\alpha_m}{1 - 2\alpha_f + 2\alpha_m} \tag{3.126}$$

$$\lim_{\Delta t\lambda\to\infty} \zeta_2 = \frac{1}{\alpha_f} - 1 \tag{3.127}$$

which after computing $|\frac{1}{\alpha_f}-1| \leq 1$ and $|\frac{1+2\alpha_f-2\alpha_m}{1-2\alpha_f+2\alpha_m}| \leq 1$, leads to the following criterion for unconditional stability

$$\alpha_m \geq \alpha_f \geq \frac{1}{2}. \tag{3.128}$$

In order to be able to control high frequency damping the parameters α_m and α_f are chosen such that both eigenvalues approach the same prescribed value when $\Delta t \to \infty$. In Section 3.4.1 the spectral radius was derived as $\rho^h = \max(|\zeta_{1,2}^h|)$, which results in the following spectral radius for $\Delta t \to \infty$

$$\rho_\infty^h = \lim_{\Delta t \to \infty} \max(|\zeta_{1,2}^h|). \tag{3.129}$$

From Equations (3.126) and (3.127) it then can be derived that

$$\alpha_f = \frac{1}{1+\rho_\infty}, \qquad \alpha_m = \frac{1}{2}\frac{3-\rho_\infty}{1+\rho_\infty} \tag{3.130}$$

with $0 \leq \rho_\infty^h \leq 1$ representing the user controlled spectral radius for an infinite time step. It is noted that when $\rho_\infty^h = 1$ the generalised-α method reduces to the trapezoidal rule, which is also second order accurate and unconditionally stable.

When applying the derivations for γ, α_m and α_f, the eigenvalues depend on time step size Δt, model parameters ω and ξ and time integration scheme parameter ρ_∞^h. For different combinations of ξ and ρ_∞^h the eigenvalues are plotted for a range of time step sizes $10^{-3} \leq \Delta t/T \leq 10^3$. This can be seen in Figure 3.5. First of all it can be noticed that for $\rho_\infty^h = 1$ the generalised-α method indeed leads to the trapezoidal rule (see Figure 3.2 in Section 3.4.1). For smaller values of ρ_∞^h it can be seen clearly that the spectral radius ρ^h approaches ρ_∞^h for large time steps. For small time steps it can be observed that the maximum of the absolute eigenvalues is always equal to 1, and that the other eigenvalue starts at $1 - \frac{1}{\alpha_m}$, as is given by Equation (3.123).

3.5.2 Generalised-α method for second order problems

The generalised-α method for second order problems is given as

$$u_{n+\alpha_f} = \alpha_f\, u_{n+1} + (1-\alpha_f)\, u_n \tag{3.131}$$

$$\dot{u}_{n+\alpha_f} = \alpha_f\, \dot{u}_{n+1} + (1-\alpha_f)\, \dot{u}_n \tag{3.132}$$

$$\ddot{u}_{n+\alpha_m} = \alpha_m\, \ddot{u}_{n+1} + (1-\alpha_m)\, \ddot{u}_n \tag{3.133}$$

$$u_{n+1} = u_n + \Delta t\, \dot{u}_n + \Delta t^2 \left(\left(\frac{1}{2} - \beta \right) \ddot{u}_n + \beta\, \ddot{u}_{n+1} \right) \tag{3.134}$$

$$\dot{u}_{n+1} = \dot{u}_n + \Delta t \left((1-\gamma)\, \ddot{u}_n + \gamma\, \ddot{u}_{n+1} \right) \tag{3.135}$$

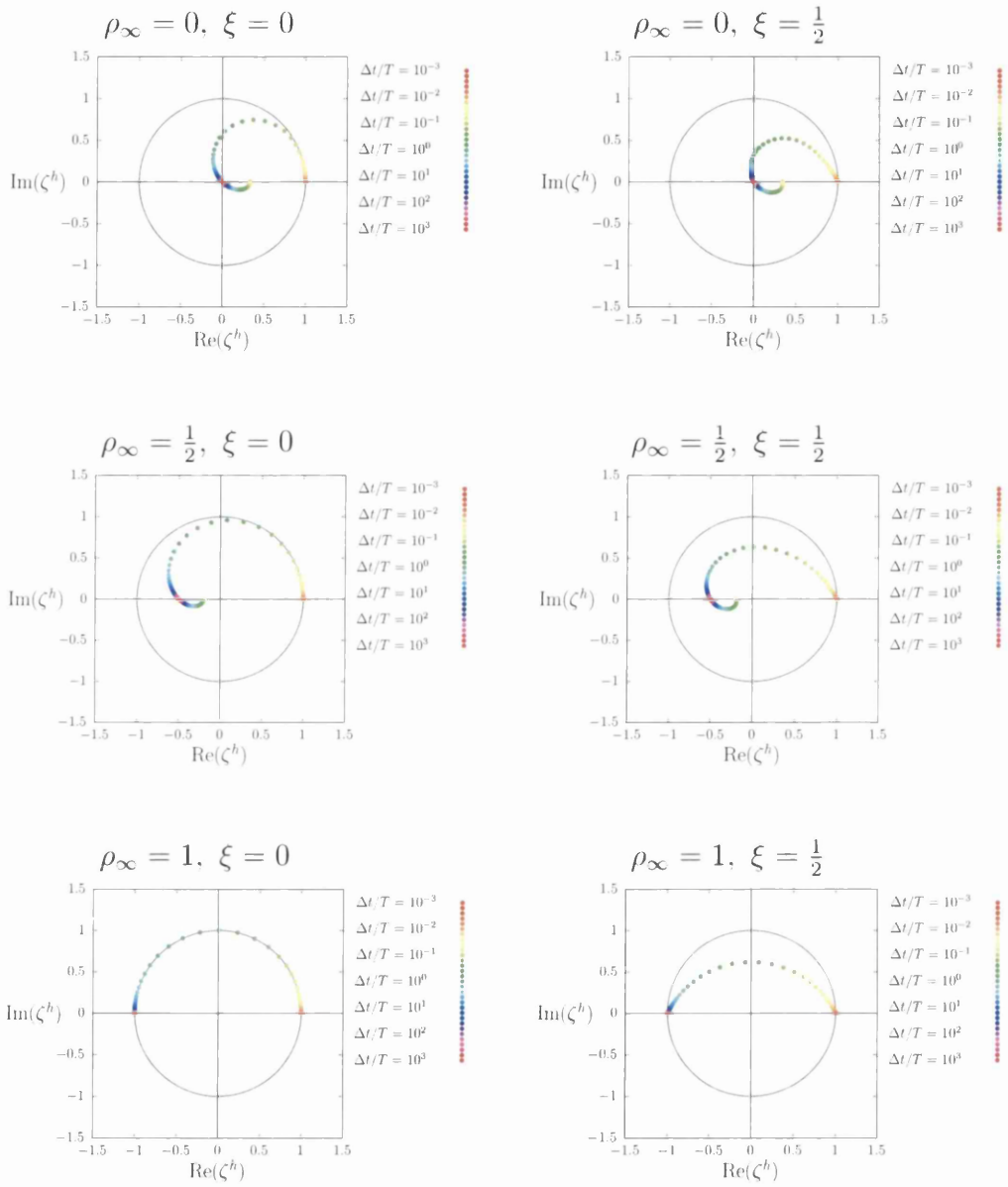

Figure 3.5: Eigenvalues for first order problem discretised with generalised-α method.

where the scalar variable $u_{n+\alpha_f}$, its time derivative $\dot{u}_{n+\alpha_f}$ and its second time derivative $\ddot{u}_{n+\alpha_m}$ are evaluated at respectively time instants $t_{n+\alpha_f}$, $t_{n+\alpha_f}$ and $t_{n+\alpha_m}$. The scalar quantities α_f, α_m, β and γ are time integration parameters. To establish the requirements for which the time integration parameters lead to unconditional stability and second order accuracy, the second order problem that was introduced in Section 3.4.2 is solved with the generalised-α method

$$\ddot{u}_{n+\alpha_m} + 2\xi\omega\dot{u}_{n+\alpha_f} + \omega^2 u_{n+\alpha_f} = 0. \tag{3.136}$$

After substitution of Equations (3.131), (3.132) and (3.133) the problem can be rewritten in the following form

$$\begin{Bmatrix} u_{n+1} \\ \Delta t\dot{u}_{n+1} \\ \Delta t^2\ddot{u}_{n+1} \end{Bmatrix} = \mathbf{A} \begin{Bmatrix} u_n \\ \Delta t\dot{u}_n \\ \Delta t^2\ddot{u}_n \end{Bmatrix}. \tag{3.137}$$

Due to its length, the amplificaiton matrix $\mathbf{A}$ is not given here. Again the accuracy will be determined using the exact amplification factor. Based on the analytical solution that was given in Section 3.4.2, it can be derived that

$$u(t_{n+k}) = e^{(k+1)\lambda\Delta t} u(t_{n-1}), \qquad k = 0, 1, 2, 3 \tag{3.138}$$

where λ was given as

$$\lambda_{1,2} = \omega\left(-\xi \pm \sqrt{\xi^2 - 1}\right). \tag{3.139}$$

Replacement of u_{n+k} with $u(t_{n+k})$ for $k = 0, 1, 2, 3$ followed by a Taylor series expansion gives the following error e_P^*

$$e_P^* = \Big((-1 + 2\alpha_f - 2\alpha_m + 2\gamma)\omega^2(-3\xi\omega + 4\xi^3\omega \pm \sqrt{(-1+\xi^2)\omega^2} \\ \pm 4\xi^2\sqrt{(-1+\xi^2)\omega^2})\Big) / (2\alpha_m)\ \Delta t^3 + \mathrm{O}[\Delta t^4]. \tag{3.140}$$

The leading error is a third order term. However, as it concerns a second order problem, this only leads to first order accuracy (see [37]). It follows that the generalised-α method for second order problems is second order accurate when

$$\gamma = \frac{1}{2} + \alpha_m - \alpha_f \tag{3.141}$$

which is the exact same condition that was found for the generalised-α method for first order problems.

To find the conditions for unconditional stability the eigenvalues of amplification matrix $\mathbf{A}$ are derived. As the eigenvalues are very lengthy they will not be given here. The eigenvalues for $\Delta t \to 0$ are given as

$$\lim_{\Delta t \to 0} \zeta_1 = 1 - \frac{1}{\alpha_m} \tag{3.142}$$

$$\lim_{\Delta t \to 0} \zeta_2 = 1 \tag{3.143}$$

$$\lim_{\Delta t \to 0} \zeta_3 = 1. \tag{3.144}$$

With the stability condition that the absolute value of every eigenvalue has to less or equal than one, it can again be derived that

$$\alpha_m \geq \frac{1}{2}. \tag{3.145}$$

For large time steps the following limits are found

$$\lim_{\Delta t\omega \to \infty} \zeta_1 = 1 - \frac{1}{\alpha_f} \tag{3.146}$$

$$\lim_{\Delta t\omega \to \infty} \zeta_2 = \frac{-1 + \alpha_f - \alpha_m - \sqrt{1 - 2\alpha_f + \alpha^2 + 2\alpha_m - 2\alpha_f\alpha_m + \alpha_m^2 - 4\beta} + 2\beta}{2\beta} \tag{3.147}$$

$$\lim_{\Delta t\omega \to \infty} \zeta_3 = \frac{-1 + \alpha_f - \alpha_m + \sqrt{1 - 2\alpha_f + \alpha^2 + 2\alpha_m - 2\alpha_f\alpha_m + \alpha_m^2 - 4\beta} + 2\beta}{2\beta}. \tag{3.148}$$

Similar to the generalised-α method for first order problems, the time integration parameters α_m, α_f and β are expressed in terms of ρ_∞^h

$$\alpha_f = \frac{1}{\rho_\infty + 1}, \qquad \alpha_m = \frac{2 - \rho_\infty}{1 + \rho_\infty}, \qquad \beta = \frac{(1 + \alpha_m - \alpha_f)^2}{4}. \tag{3.149}$$

For the given expressions for γ, α_m, α_f and β the real and imaginary parts of the eigenvalues are plotted in Figure 3.6. It is observed that again for large time steps the eigenvalues approach the value of ρ_∞^h and for small time steps two of the eigenvalues approach 1 and the other one $1 - \frac{1}{\alpha_m}$. Also, when $\rho_\infty^h = 1$ (trapezoidal rule) the plots are similar to the ones in Section 3.4.2.

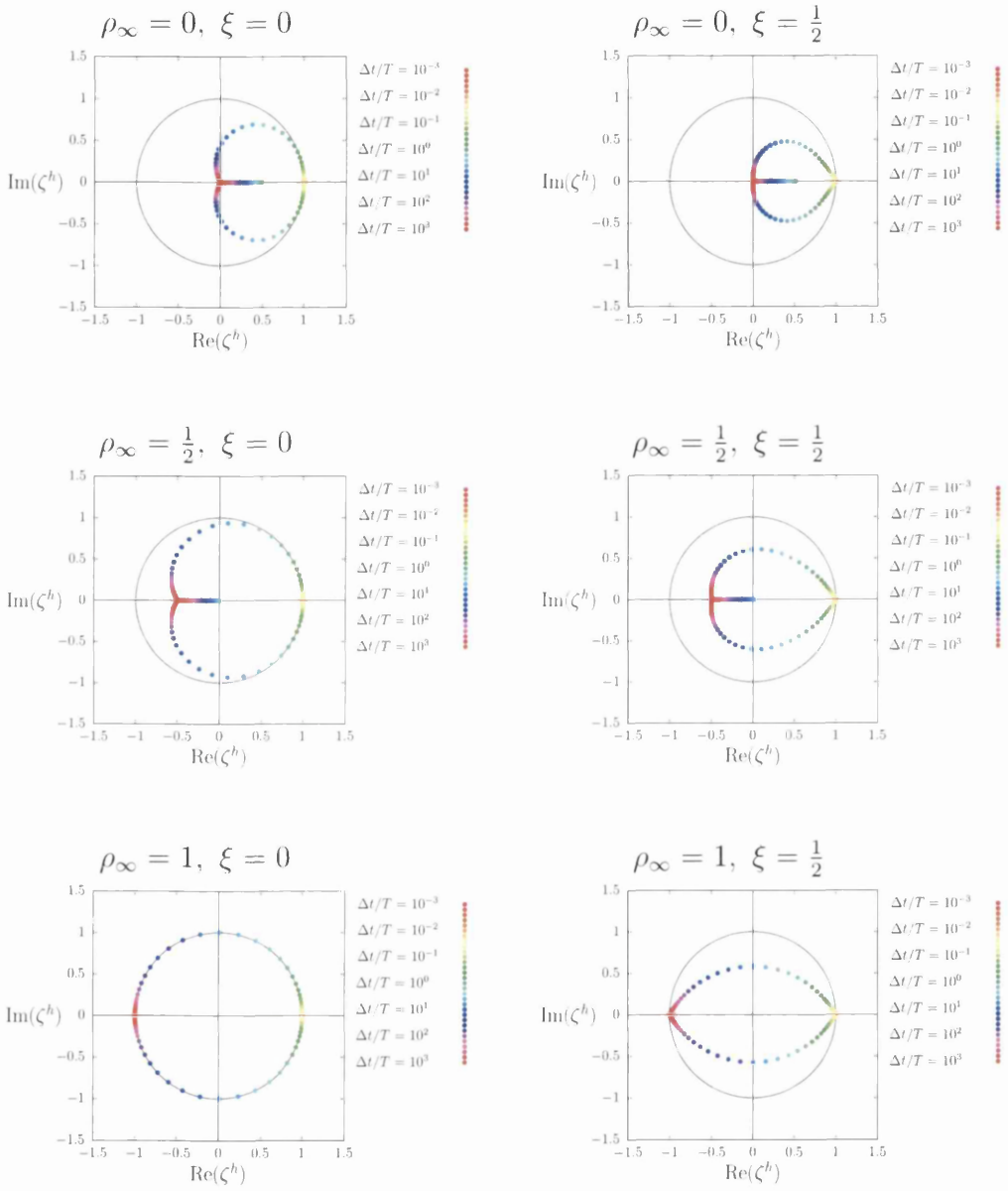

Figure 3.6: Eigenvalues for second order problem discretised with generalised-α method.

Chapter 4

Time integration schemes for coupled problems

4.1 Combining two different schemes in FSI

In this chapter the performance of time integration schemes when used in coupled problems is discussed and a solution that prevents stability and accuracy problems is presented. A 1D model problem is used to illustrate the difficulties that arise when using two different time integration schemes for the different domains.

Coupled problems, consisting of two or more domains which interact at common boundaries, are often discretised by using different time integration schemes for the different domains. Especially in partitioned solution strategies for fluid-structure interaction, it is common practise to employ one time integration scheme for the first order problem of fluid dynamics and another for the second order problem of solid dynamics. It is clearly desirable to use the most appropriate time integration scheme for each individual sub-problem. However, this approach may lead to a loss of stability and accuracy of the overall problem unless special measures are taken.

Such problems do not arise if the same time integration scheme is applied to the overall problem. In [41], a space-time finite element method is employed for the discretisation of the solid dynamics sub-problem, which had originally been developed in the context of fluid mechanics. Bazilevs et al. [42] have addressed the issue of time discretisation in fluid-structure

interaction systems. The generalised-α method for second order problems is used for discretisation of the solid and the mesh part and the generalised-α method for first order problems is used for discretisation of the fluid part. The problem that arises when two different time integration schemes are used is solved by applying the expression for α_m derived in [38] for first order problems to all domains in the fluid-structure interaction system. This makes the fluid part of the problem optimally damped. It is shown in [42] that when the expression for α_m as derived in [38] is applied to the formulation of the generalised-α method for second order problems, second-order accuracy and unconditional stability are maintained. However, with this solution it is no longer possible to optimally damp both domains separately. Note that both [41] and [42] employ monolithic solution strategies.

The publications [1,3,4,7,8,11,16,17,24,32,43–46] and several references therein describe different computational strategies for fluid-structure interaction and involve either one or more time integration schemes. It is noted that the information provided on the integration of time and the temporal matching of kinematic quantities at the interface is often vague or missing.

In order to investigate what happens to the stability and accuracy properties when two different time integration schemes are used, a one dimensional linear model problem is analysed in detail. The two versions of the generalised-α method for first and second order systems are applied to the model problem to find out whether second order accuracy and unconditional stability are still maintained.

4.1.1 The model problem

The model problem considered is the one dimensional damped spring-mass system shown in Figure 4.1. One domain is represented by a point mass and a spring, the other domain is represented by a point mass and a dashpot. At the interface between the two domains the traction forces are in equilibrium and the displacements are equal. This leads to the following equations

$$(1-\alpha)\,\ddot{u}^s + \omega^2 u^s = -\alpha\ddot{u}^f - 2\xi\omega\dot{u}^f, \qquad u^s = u^f \tag{4.1}$$

with

$$\alpha = \frac{m^f}{m}, \qquad 1-\alpha = \frac{m^s}{m}, \qquad m^f + m^s = m,$$
$$\omega = \sqrt{k/m}, \qquad \xi = \frac{c}{2\sqrt{km}}$$

where m is the total mass of the system, m^f and m^s are respectively the mass of domain f and domain s, k is the spring stiffness and c is the damping coefficient, ω is the natural frequency of the system and ξ a dimensionless damping ratio. Furthermore, $\ddot{u}^s$ and u^s are respectively the acceleration and displacement of m^s, while $\ddot{u}^f$ and $\dot{u}^f$ are respectively the acceleration and velocity of m^f.

The standard analytical solution of this system is found by solving

$$\ddot{u} + 2\xi\omega\dot{u} + \omega^2 u = 0. \tag{4.2}$$

The solution of this problem is given in Section 3.4.2. In Figure 4.2 the displacement u is displayed against time for $\xi = 0.01$, $\omega = 1$, $u_0 = 0.1$ and $\dot{u}_0 = 0$. The characteristic time period T and exact amplification factor ζ are given in Section 3.4.2 as well.

Both domains of the coupled problem are solved using the generalised-α method. The formulation of the generalised-α method and its stability and accuracy properties, are given in Section 3.5. Equation (4.1) contains $\ddot{u}^s$, u^s, $\ddot{u}^f$ and $\dot{u}^f$. Thus the left-hand side is a second order expression in terms of u^s whereas the right-hand side is a first order expression in terms of $\dot{u}^f$. Therefore, the right-hand side is discretised with the generalised-α method as given in Section 3.5.1 and the left-hand side is discretised with the integration scheme given in Section 3.5.2.

As one of the interface conditions states that $\dot{u}^s = \dot{u}^f$, Equations (3.108) to (3.110) and Equations (3.131) to (3.135) are rewritten in such a way that

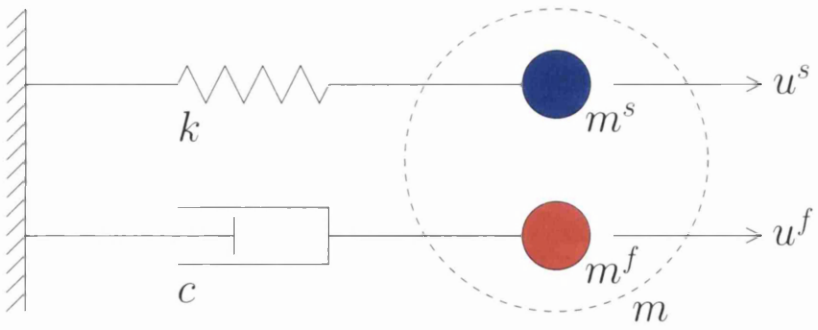

Figure 4.1: The model problem.

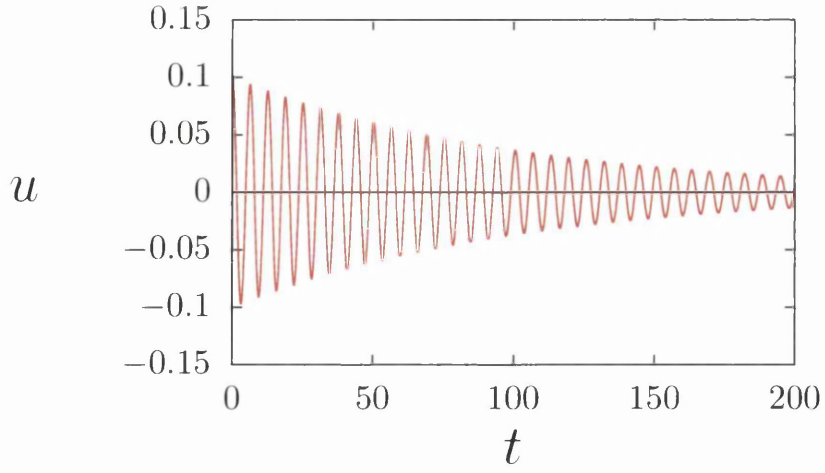

Figure 4.2: Response of the spring-mass system for $\xi = 0.01$, $\omega = 1$, $u_0 = 0.1$ and $\dot{u}_0 = 0$.

the quantities at time instants $t_{n+\alpha_m}$, $t_{n+\alpha_f}$ and t_{n+1} are only depending on $\dot{u}_{n+1}$, $\ddot{u}_n$, $\dot{u}_n$, and u_n. Rewriting equations (3.131) to (3.135) leads to

$$\ddot{u}^s_{n+\alpha^s_m} = \frac{\alpha^s_m}{\Delta t \gamma^s}\left(\dot{u}^s_{n+1} - \dot{u}^s_n\right) + \left(1 - \frac{\alpha^s_m}{\gamma^s}\right)\ddot{u}^s_n \tag{4.3}$$

$$u^s_{n+\alpha^s_f} = \frac{\alpha^s_f \Delta t \beta^s}{\gamma^s}\dot{u}^s_{n+1} + u^s_n + \alpha^s_f \Delta t\left(1 - \frac{\beta^s}{\gamma^s}\right)\dot{u}^s_n \tag{4.4}$$

$$+\alpha^s_f \Delta t^2\left(\frac{1}{2} - \frac{\beta^s}{\gamma^s}\right)\ddot{u}^s_n \tag{4.5}$$

$$\ddot{u}^s_{n+1} = \frac{1}{\Delta t \gamma^s}\left(\dot{u}^s_{n+1} - \dot{u}^s_n\right) - \frac{1-\gamma^s}{\gamma^s}\ddot{u}^s_n \tag{4.6}$$

$$u^s_{n+1} = \frac{\Delta t \beta^s}{\gamma^s}\dot{u}^s_{n+1} + u^s_n + \Delta t\left(1 - \frac{\beta^s}{\gamma^s}\right)\dot{u}^s_n + \Delta t^2\left(\frac{1}{2} - \frac{\beta^s}{\gamma^s}\right)\ddot{u}^s_n \tag{4.7}$$

with $\ddot{u}^s_{n+1}$, $\dot{u}^s_{n+1}$ and u^s_{n+1} representing respectively the acceleration, velocity and displacement of m^s at time instant t_{n+1} whereas $\ddot{u}^s_n$, $\dot{u}^s_n$ and u^s_n respectively denote the acceleration, velocity and displacement of m^s at time instant t_n. The acceleration at $t_{n+\alpha^s_m}$ and the displacement at $t_{n+\alpha^s_f}$ are represented respectively by $\ddot{u}^s_{n+\alpha^s_m}$ and $u^s_{n+\alpha^s_f}$.

Equations (3.108) to (3.110) are being rewritten as follows

$$\ddot{u}^f_{n+\alpha^f_m} = \frac{\alpha^f_m}{\Delta t \gamma^f}\left(\dot{u}^f_{n+1} - \dot{u}^f_n\right) + \left(1 - \frac{\alpha^f_m}{\gamma^f}\right)\ddot{u}^f_n \tag{4.8}$$

$$\dot{u}^f_{n+\alpha^f_f} = \alpha^f_f \dot{u}^f_{n+1} + \left(1 - \alpha^f_f\right)\dot{u}^f_n \tag{4.9}$$

$$\ddot{u}^f_{n+1} = \frac{1}{\Delta t \gamma^f}\left(\dot{u}^f_{n+1} - \dot{u}^f_n\right) - \frac{1-\gamma^f}{\gamma^f}\ddot{u}^f_n. \tag{4.10}$$

Here, $\ddot{u}^f_{n+1}$ and $\dot{u}^f_{n+1}$ represent respectively the acceleration and velocity of m^f at time instant t_{n+1}, while $\ddot{u}^f_n$ and $\dot{u}^f_n$ denote the acceleration and velocity of m^f at time instant t_n. The quantities $\ddot{u}^f_{n+\alpha^f_m}$ and $\dot{u}^f_{n+\alpha^f_f}$ are associated with the time instants $t_{n+\alpha^f_m}$ and $t_{n+\alpha^f_f}$ respectively.

4.1.2 Stability

In order to solve the coupled problem with the generalised-α method for both domains, equation (4.1) is discretised as follows

$$(1-\alpha)\,\ddot{u}^s_{n+\alpha^s_m} + \omega^2 u^s_{n+\alpha^s_f} = -\alpha\ddot{u}^f_{n+\alpha^f_m} - 2\xi\omega\dot{u}^f_{n+\alpha^f_f} \tag{4.11}$$

with

$$\dot{u}^s_{n+1} = \dot{u}^f_{n+1} = \dot{u}^i_{n+1} \tag{4.12}$$

$$\dot{u}^s_n = \dot{u}^f_n = \dot{u}^i_n. \tag{4.13}$$

The quantities $\dot{u}^i_{n+1}$ and $\dot{u}^i_n$ represent the interface velocity for the current and the previous time step respectively. After substitution of equations (4.3), (4.5), (4.8) and (4.10) into equation (4.11), and combining this with equations (4.6), (4.7), (4.10), (4.12) and (4.13), the total set of equations to describe the problem can be written as follows

$$\begin{Bmatrix} u^s_{n+1} \\ \Delta t\dot{u}^i_{n+1} \\ \Delta t^2\ddot{u}^s_{n+1} \\ \Delta t^2\ddot{u}^f_{n+1} \end{Bmatrix} = \begin{bmatrix} A_{11} & A_{12} & A_{13} & A_{14} \\ A_{21} & A_{22} & A_{23} & A_{24} \\ A_{31} & A_{32} & A_{33} & A_{34} \\ A_{41} & A_{42} & A_{43} & A_{44} \end{bmatrix} \begin{Bmatrix} u^s_n \\ \Delta t\dot{u}^i_n \\ \Delta t^2\ddot{u}^s_n \\ \Delta t^2\ddot{u}^f_n \end{Bmatrix} \tag{4.14}$$

where $\mathbf{A}$ is the amplification matrix of the system. The expressions for A_{11} to A_{44} are lengthy and therefore not given here. Calculating the response of the model problem by solving equation (4.14) gives a stable result only if the

absolute values of all eigenvalues ζ_i^h of amplification matrix $\mathbf{A}$ are less than or equal to 1, as was shown in Section 3.4.2.

The amplification matrix $\mathbf{A}$, and thus the eigenvalues, depend on the dimensionless problem variables ω, ξ and α, the generalised-α method parameters ρ_∞^s and ρ_∞^f and the ratio $\Delta t/T$. Note that it is common practise in computational fluid-structure interaction, especially in the context of partitioned solution strategies, to enforce the equality of velocity and displacement at the interface, while the accelerations are allowed to evolve independently.

For the eigenvalue analysis of the amplification matrix the absolute value of the largest eigenvalue $|\zeta^h|_{max}$ is plotted as a function of α and $\Delta t/T$ for a range of values for ξ, ω, ρ_∞^s and ρ_∞^f. The plots can be found in Appendix A. For certain combinations of ξ, ω, ρ_∞^s and ρ_∞^f the plots show areas where $|\zeta^h|_{max} > 1$. It can be seen that there is a relation between plots with $|\zeta^h|_{max} > 1$ and the combination of ρ_∞^s and ρ_∞^f and therefore the eigenvalue analysis of the amplification matrix is performed for three different cases: $\rho_\infty^s = \rho_\infty^f$, $\rho_\infty^s < \rho_\infty^f$ and $\rho_\infty^s > \rho_\infty^f$.

Case 1: $\rho_\infty^s = \rho_\infty^f$.

Figure 4.3 shows a contour plot of the absolute value of the largest eigenvalue $|\zeta^h|_{max}$ as a function of α and $\Delta t/T$ for $\rho_\infty^s = \rho_\infty^f = 0.3$, $\xi = 0.01$ and $\omega = 1.0$. It can be seen that the value of $|\zeta^h|_{max}$ never exceeds 1. The figures in the appendix for other values of $\rho_\infty^s = \rho_\infty^f$ show similar behaviour of $|\zeta^h|_{max}$, which in none of these cases exceeds 1. This is also shown in Figure 4.3 where the value of $|\zeta^h|_{max}$ for a fixed value of α is plotted as a function of $\Delta t/T$ for different values of ρ_∞^s and ρ_∞^f. This plot clearly shows that $|\zeta^h|_{max}$ never exceeds 1. Therefore the system is unconditionally stable.

It can also be seen that for small time steps the value of $|\zeta^h|_{max}$ approaches 1 and the value of $|\zeta^h|_{max}$ for large $\Delta t/T$ approaches the value for ρ_∞^s and ρ_∞^f. It can, in fact, be shown that for any $0 \leq \rho_\infty^s = \rho_\infty^f \leq 1$

$$\lim_{\frac{\Delta t}{T} \to 0} |\zeta^h|_{max} = 1 \tag{4.15}$$

$$\lim_{\frac{\Delta t}{T} \to \infty} |\zeta^h|_{max} = \rho_\infty^s = \rho_\infty^f. \tag{4.16}$$

For fixed values of α it is possible to present the eigenvalues in the same way as in Section 3.4. In Figure 4.4 the imaginary parts of the eigenvalues

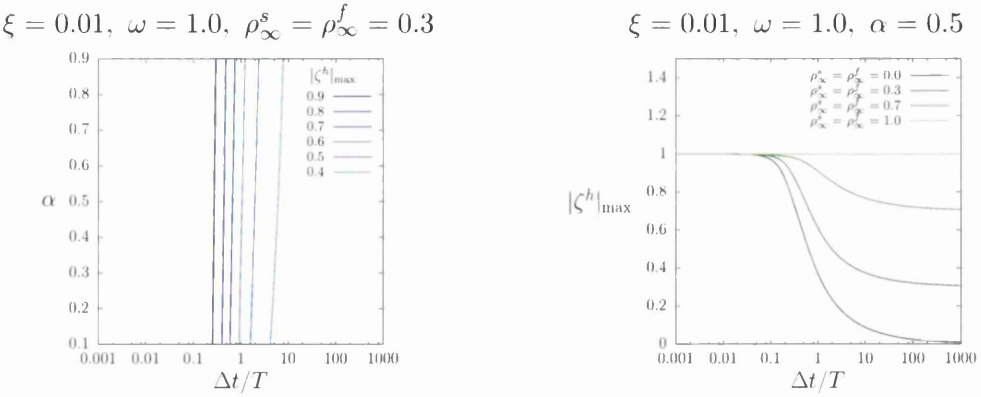

Figure 4.3: Contour and line plot of the spectral radius $|\zeta^h|_{\max}$ for a coupled one degree of freedom second order problem, solved with the same time integration scheme for both domains.

of amplification matrix $\mathbf{A}$ are shown against the real parts for a range of time step sizes from 10^{-3} to 10^3. The first plot shows the eigenvalues for $\xi = 0$, $\omega = 1$, $\alpha = 0.5$ and $\rho^s_\infty = \rho^f_\infty = 1$. As the generalised-$\alpha$ method for $\rho_\infty = 1$ reduces to the trapezoidal rule, which is known to cause no numerical damping, and as the physical damping parameter ξ is set to zero, it is expected that all eigenvalues lie on the unit circle. It can be seen that the plot is the same as the corresponding plot in Figure 3.6 in Section 3.5.2. The eigenvalues for $\xi = 0.01$, $\omega = 1$, $\alpha = 0.5$, $\rho^s_\infty = 0.3$ and $\rho^f_\infty = 0.3$ are shown in Figure 4.4 as well. It can be seen that all four eigenvalues approach 0.3 for large time steps. Two of the eigenvalues seem to follow a similar pattern as two of the eigenvalues in Figure 3.6, however, the other two eigenvalues create a new pattern that replaces the pattern of the third eigenvalue in Figure 3.6.

Case 2: $\rho^s_\infty < \rho^f_\infty$**.**

A contour plot of $|\zeta^h|_{max}$ for $\rho^s_\infty = 0.3$ and $\rho^f_\infty = 0.7$ and a plot of the value of $|\zeta^h|_{max}$ for a fixed value of α and different combinations of ρ^s_∞ and ρ^f_∞ are shown in Figure 4.5. Plots for other combinations of ρ^s_∞ and ρ^f_∞ for which $\rho^s_\infty < \rho^f_\infty$ can be found in Appendix A. It can be seen that the system is again unconditionally stable. Comparing this case with $\rho^s_\infty = \rho^f_\infty$ it is noted that a relative minimum is visible in the contour plot. The minimum seems to be the result of one eigenvalue increasing and another eigenvalue decreasing such that the first one replaces the second one as the maximum eigenvalue.

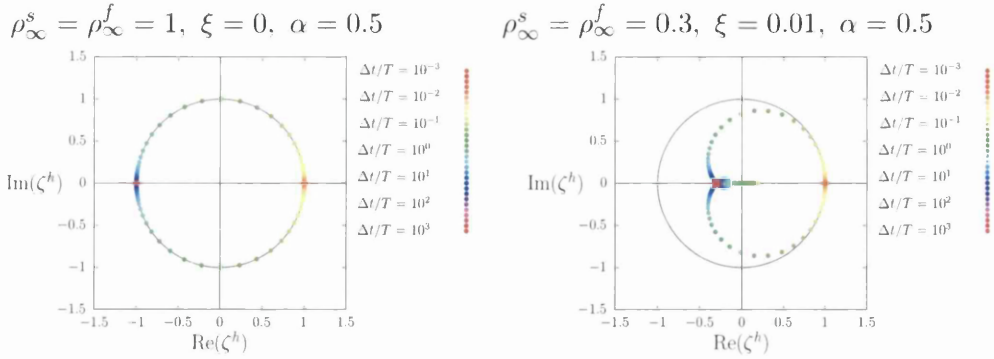

Figure 4.4: Eigenvalues for a coupled one degree of freedom second order problem, solved with the same time integration scheme for both domains.

In general, for $\rho^f_\infty > \rho^s_\infty$, the maximum eigenvalue approaches 1 again for small time steps, but now approaches ρ^f_∞ for large time steps:

$$\lim_{\frac{\Delta t}{T} \to 0} |\zeta^h|_{\max} = 1 \tag{4.17}$$

$$\lim_{\frac{\Delta t}{T} \to \infty} |\zeta^h|_{\max} = \rho^f_\infty \tag{4.18}$$

The limits for $\Delta t/T \to 0$ and $\Delta t/T \to \infty$ can also be observed in Figure 4.6. It can be seen that three eigenvalues approach ρ^s_∞ for large steps, however the fourth and maximum eigenvalue approaches ρ^f_∞. It is clear that the system is unconditionally stable. Also, the eigenvalues in Figure 4.6 confirm the behaviour of $|\zeta^h|_{\max}$ in Figure 4.5 as, at one point, the eigenvalue that approaches ρ^f_∞ indeed becomes larger than the eigenvalues that approach ρ^s_∞.

Case 3: $\rho^s_\infty > \rho^f_\infty$.

Figure 4.5 also shows the contour plot of $|\zeta^h|_{\max}$ for $\rho^s_\infty = 0.7$ and $\rho^f_\infty = 0.3$ and plots for different combinations of ρ^s_∞ and ρ^f_∞ for $\alpha = 0.8$. More contour plots for the case $\rho^s_\infty > \rho^f_\infty$ can be found in Appendix A again. As opposed to the previous two cases, the contour plot from Figure 4.5 shows an area with $|\zeta^h|_{\max} > 1$. Other plots for this case show similar areas. Therefore the system is no longer unconditionally stable. The following limits are observed

$$\lim_{\frac{\Delta t}{T} \to 0} |\lambda|_{max} = 1 \tag{4.19}$$

$$\lim_{\frac{\Delta t}{T} \to \infty} |\lambda|_{max} = \rho^s_\infty. \tag{4.20}$$

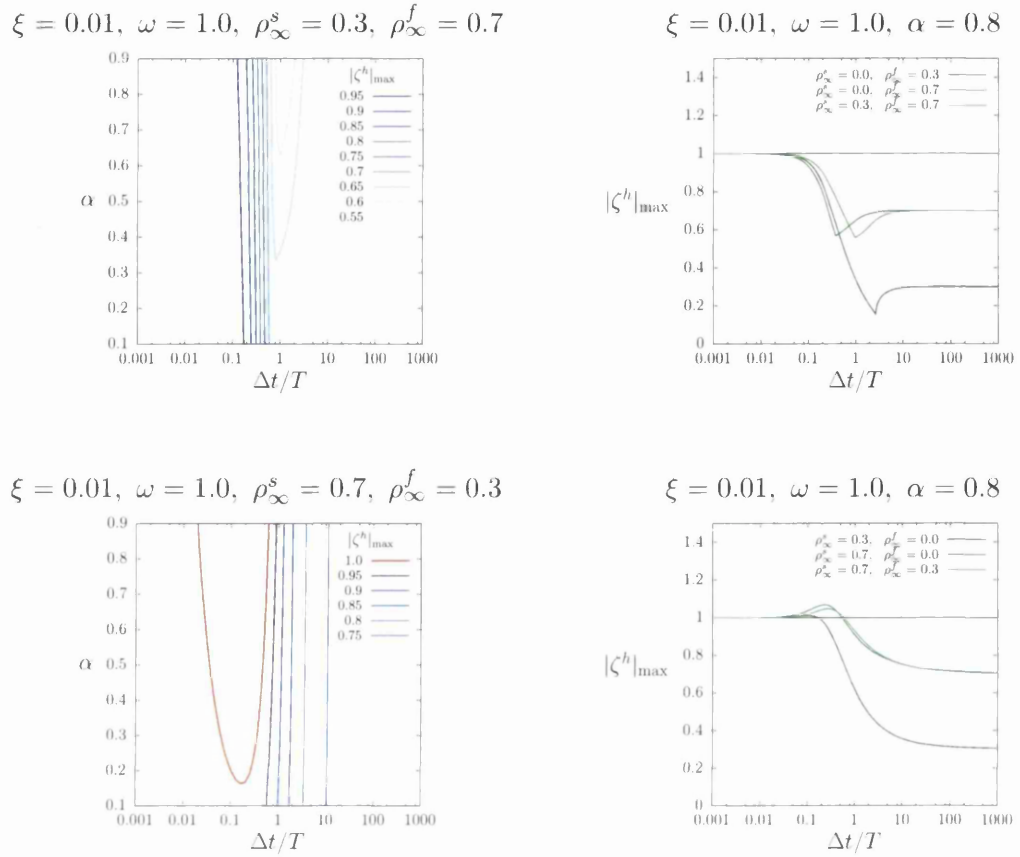

Figure 4.5: Contour and line plots of the spectral radius $|\zeta^h|_{\max}$ for a coupled one degree of freedom second order problem, solved with different time integration schemes for both domains.

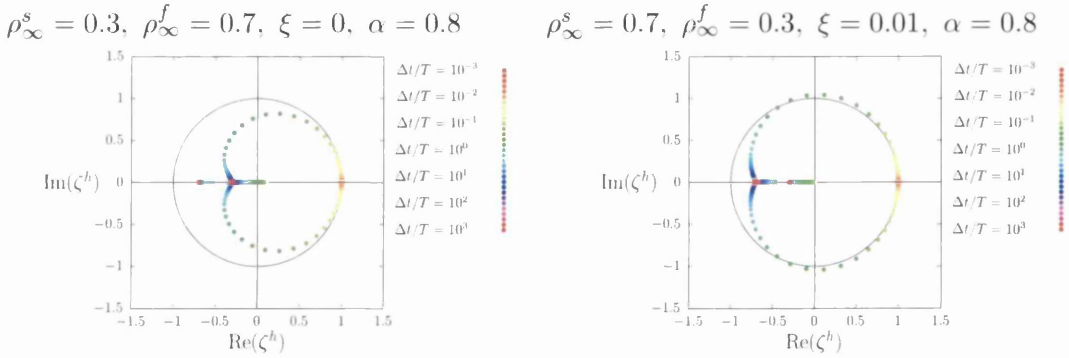

Figure 4.6: Eigenvalues for a coupled one degree of freedom second order problem, solved with different time integration schemes for both domains.

Based on the plots in Appendix A it is noted that a larger value for α reduces the stability of the system. It can also be seen that decreasing the amount of physical damping has the same effect (in Appendix A the value of $|\zeta^h|_{\max}$ for all combinations of ρ_∞^s and ρ_∞^f is shown for both $\xi = 0.01$ and $\xi = 0.001$). Thus, for $\rho_\infty^s > \rho_\infty^f$, the stability improves with smaller α and larger ξ.

The fact that the system is no longer unconditionally stable can also be seen in Figure 4.6, where for some time step sizes the eigenvalues clearly lie outside the unit circle. It can also be noticed that, similar to Case 2, three eigenvalues approach ρ_∞^s and only one eigenvalue approaches ρ_∞^f.

Summarising, the system is unconditionally stable if $\rho_\infty^s = \rho_\infty^f$ or $\rho_\infty^s < \rho_\infty^f$. For small time steps the value for $|\zeta_{\max}^h|$ approaches 1 and for large time steps it approaches $\max(\rho_\infty^s, \rho_\infty^f)$.

4.1.3 Accuracy

Both versions of the generalised-α method can be shown to be second order accurate. In order to analyse the accuracy of the coupled problem where two different time integration schemes are used, the error is obtained. It is recalled from Section 3.5.2 that for a second order problem to be second order accurate, the leading error e^* has to be of the fourth order. For the coupled problem the error e^* is derived as

$$e^* = -\Big(4(\rho_\infty^s - \rho_\infty^f)\omega^2((2-\alpha)\xi\omega + 4(-1+\alpha)\xi^2\omega - \alpha\sqrt{(-1+\xi^2)\omega^2} \\ +4(-1+\alpha)\xi^2\sqrt{(-1+\xi^2)\omega^2})\Big)\ \Delta t^3/\left(8 - 4\rho_\infty^s + \alpha(1+\rho_\infty^s - 3\rho_\infty^f + \rho_\infty^s\rho_\infty^f)\right) \\ + \mathrm{O}[\Delta t^4] \quad (4.21)$$

From Equation (4.21) it can be concluded that the coupled system is only first order accurate when $\rho_\infty^s \neq \rho_\infty^f$. So when the coupled problem is solved with two different time integration schemes the results are no longer second order accurate, even if those time integration schemes are known to the be second order accurate and unconditionally stable. In order to prevent a loss in stability and accuracy properties, the interpolation of the variables at the interface is examined more closely in the next section.

4.2 Interpolation at the interface

4.2.1 Introduction

In the previous section it is shown that applying two different time integration schemes to solve the linear model problem leads to a loss of stability and accuracy. It is thought that this is due to the inaccurate interpolation of the traction force at the interface between the two domains [18]. At the interface, Equation (4.11) requires that the force exerted by m^s on m^f is equal to the force exerted by m^f on m^s. However, if two different time integration schemes are used, the forces are not evaluated at exactly the same time instant within a time step. Therefore an extra equation is added to linearly interpolate between the time instants t_n and t_{n+1} (see Figure 4.7) and thus to allow for equating the traction forces at the same time instant.

Hence, Equation (4.11) is replaced by the following equations

$$F^s_{n+\alpha^s_f} = (1-\alpha)\,\ddot{u}^s_{n+\alpha^s_m} + \omega^2 u^s_{n+\alpha^s_f} \tag{4.22}$$

$$F^f_{n+\alpha^f_f} = -\alpha\ddot{u}^f_{n+\alpha^f_m} - 2\xi\omega\dot{u}^f_{n+\alpha^f_f} \tag{4.23}$$

where

$$F^s_{n+\alpha^s_f} = \alpha^s_f F_{n+1} + \left(1-\alpha^s_f\right) F_n \tag{4.24}$$

$$F^f_{n+\alpha^f_f} = \alpha^f_f F_{n+1} + \left(1-\alpha^f_f\right) F_n. \tag{4.25}$$

With these extra equations, force $F^s_{n+\alpha^s_f}$ is evaluated at time instant $t_{n+\alpha^s_f}$ and force $F^s_{n+\alpha^f_f}$ is evaluated at time instant $t_{n+\alpha^f_f}$. Equations (4.24) and (4.25) take care of linear interpolation between the two forces so the interface condition will be satisfied. For the stability analysis the amplification matrix for the coupled problem is derived again. Equations (4.24) and (4.25) together with Equations (4.3), (4.5), (4.8) and (4.10) are substituted into Equations (4.22) and (4.23), which leads to the following set of equations

$$\begin{Bmatrix} u^s_{n+1} \\ \Delta t\dot{u}^i_{n+1} \\ \Delta t^2\ddot{u}^s_{n+1} \\ \Delta t^2\ddot{u}^f_{n+1} \\ \Delta t^2 F_{n+1} \end{Bmatrix} = \begin{bmatrix} A_{11} & A_{12} & A_{13} & A_{14} & A_{15} \\ A_{21} & A_{22} & A_{23} & A_{24} & A_{25} \\ A_{31} & A_{32} & A_{33} & A_{34} & A_{35} \\ A_{41} & A_{42} & A_{43} & A_{44} & A_{45} \\ A_{51} & A_{52} & A_{53} & A_{54} & A_{55} \end{bmatrix} \begin{Bmatrix} u^s_n \\ \Delta t\dot{u}^i_n \\ \Delta t^2\ddot{u}^s_n \\ \Delta t^2\ddot{u}^f_n \\ \Delta t^2 F_n \end{Bmatrix}. \tag{4.26}$$

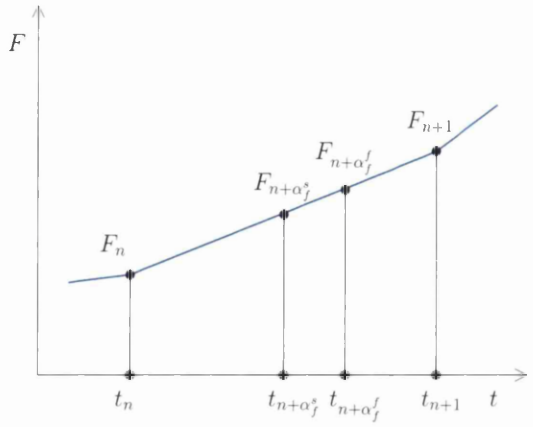

Figure 4.7: Interpolation of the traction force between time instants t_n and t_{n+1}.

The new amplification matrix $\mathbf{A}$ is used for the eigenvalue analysis for the coupled problem with linear interpolation of the traction forces at the interface. Contour plots of the absolute value of the largest eigenvalue $|\zeta^h|_{\max}$ as a function of α and $\Delta t/T$ for a range of values for ξ, ω, ρ_∞^s and ρ_∞^f can be found in Appendix B. It can be instantly noticed that the plots do not show any areas where $|\zeta^h|_{\max} > 1$.

If $\rho_\infty^s = \rho_\infty^f$, then also $\alpha_f^s = \alpha_f^f$. This means that for this case interpolation of the forces at the interface is not needed as the forces will already be evaluated at the same time instant within the time step. As a result, the contour plots for this case are exact copies of the plots shown in Appendix A. For the other two cases ($\rho_\infty^s < \rho_\infty^f$ and $\rho_\infty^s > \rho_\infty^f$) the contour plots are examined more closely.

4.2.2 Stability and accuracy for the coupled problem with traction force interpolation

Figure 4.8 shows respectively a contour plot of $|\zeta^h|_{\max}$ for $\rho_\infty^s = 0.3$ and $\rho_\infty^f = 0.7$ and a plot of $|\zeta^h|_{\max}$ for different cases of $\rho_\infty^s < \rho_\infty^f$ for a fixed value of $\alpha = 0.5$. When the contour plot in Figure 4.8 is compared with the corresponding one in Figure 4.5 from the previous section, it can be seen that the contour plot has only slightly changed. It can also be observed that the plots for $|\zeta^h|_{\max}$ show the same trends. There are no values of $|\zeta^h|_{\max}$

that exceed the critical value of 1, and thus for this case the system is still unconditionally stable.

A contour plot of $|\zeta^h|_{\max}$ for $\rho_\infty^s = 0.7$ and $\rho_\infty^f = 0.3$ is also shown in Figure 4.8. It can be seen immediately that the area for which $|\zeta^h|_{\max} > 1$ that was visible in Figure 4.5 has completely disappeared. The same can be concluded from the plot where $|\zeta^h|_{\max}$ is shown for different cases of $\rho_\infty^s > \rho_\infty^f$ with a fixed value of $\alpha = 0.5$, which does not show any values of $|\zeta^h|_{\max}$ exceeding 1. Thus, unlike the original approach, the system with interpolation of the traction force at the interface is unconditionally stable independently from the values of ρ_∞^s and ρ_∞^f.

The behaviour of the maximum eigenvalue $|\zeta^h|_{\max}$ for small and large time steps is similar to the system without interpolation of the traction force. The following expressions still hold

$$\lim_{\frac{\Delta t}{T} \to 0} |\zeta^h|_{\max} = 1 \tag{4.27}$$

$$\lim_{\frac{\Delta t}{T} \to \infty} |\zeta^h|_{\max} = \max\left(\rho_\infty^f, \rho_\infty^s\right). \tag{4.28}$$

The limits can also be seen in Figure 4.9, where the eigenvalues of the amplification matrix $\mathbf{A}$ are plotted for $\rho_\infty^s = 0.3$ and $\rho_\infty^f = 0.7$ and for $\rho_\infty^s = 0.7$ and $\rho_\infty^f = 0.3$. As $\mathbf{A}$ is a 5×5 matrix there are 5 eigenvalues plotted in the figures. It can be seen that in both figures three eigenvalues approach ρ_∞^s and two eigenvalues approach ρ_∞^f. All eigenvalues in both plots lie within the unit circle, which confirms the conclusion that when the traction forces at the interface are interpolated within the time step, the system is unconditionally stable, even when two different time integration schemes are used.

In order to analyse the accuracy of the system with interpolation of the force at the interface, the error e^* of the algorithm is calculated again. This

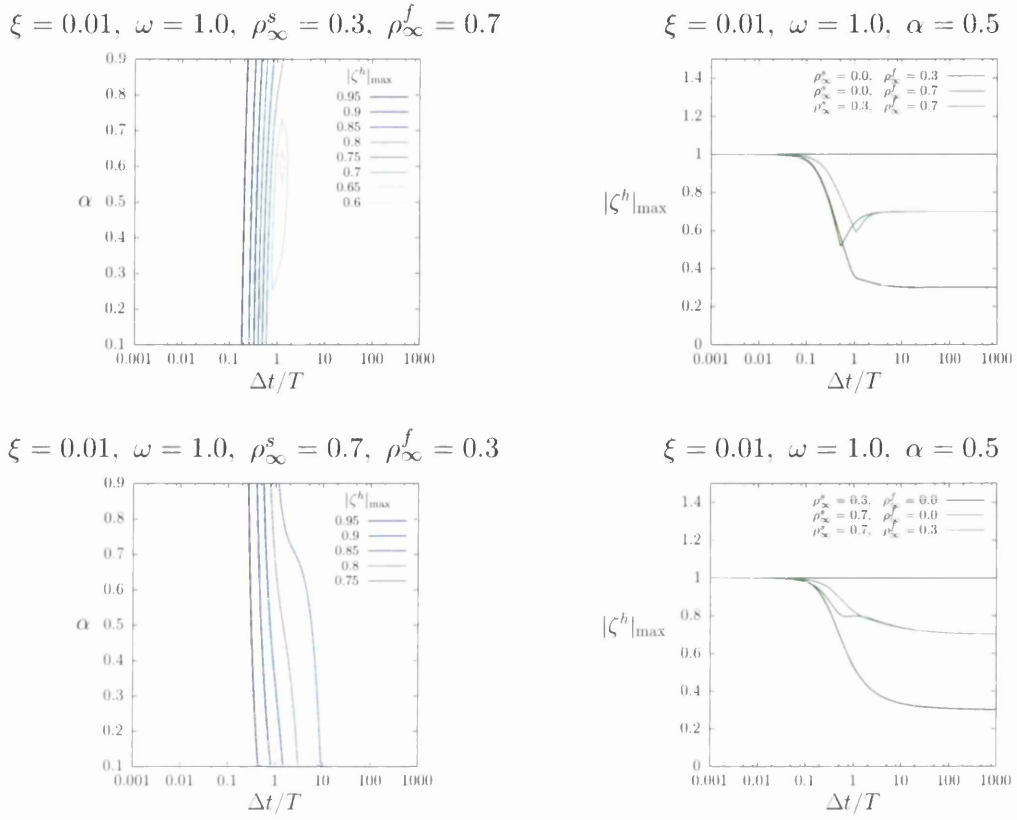

Figure 4.8: Contour and line plots of the spectral radius $|\zeta^h|_{\max}$ for a coupled one degree of freedom second order problem, solved with different time integration schemes for both domains with traction force interpolation at the interface.

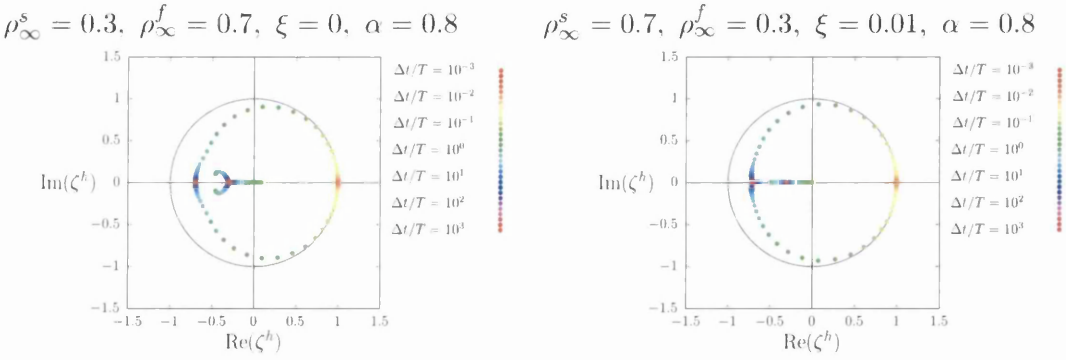

Figure 4.9: Eigenvalues for a coupled one degree of freedom second order problem, solved with different time integration schemes for both domains with traction force interpolation at the interface.

	Without force interpolation		With force interpolation	
	Stability	Accuracy	Stability	Accuracy
$\rho_\infty^s = \rho_\infty^f$	unconditionally stable	$O(\Delta t^2)$	unconditionally stable	$O(\Delta t^2)$
$\rho_\infty^s < \rho_\infty^f$	unconditionally stable	$O(\Delta t)$	unconditionally stable	$O(\Delta t^2)$
$\rho_\infty^s > \rho_\infty^f$	conditionally stable	$O(\Delta t)$	unconditionally stable	$O(\Delta t^2)$
$\lim_{\frac{\Delta t}{T}\to 0} \lvert\zeta^h\rvert_{\max} = 1$				
$\lim_{\frac{\Delta t}{T}\to \infty} \lvert\zeta^h\rvert_{\max} = \max(\rho_\infty^f, \rho_\infty^s)$				

Table 4.1: Summary of conclusions

results in a fourth order leading error for all combinations of ρ_∞^s and ρ_∞^f:

$$\begin{aligned} e^* = \big(\omega^3 \big(\big(\big(11 - 14\rho_\infty^s + 11(\rho_\infty^s)^2 + 8\xi^4 \left(7 - 10\rho_\infty^s + 7(\rho_\infty^s)^2\right) \\ -8\xi^2 \left(8 - 11\rho_\infty^s + 8(\rho_\infty^s)^2\right)\big) \left(1 - \rho_\infty^f\right)^2 - 3\alpha \left(1 - 8\xi^2 + 8\xi^4\right) \\ \left(1 + 6\rho_\infty^f + (\rho_\infty^f)^2 + (\rho_\infty^s)^2 \left(1 + 6\rho_\infty^f + (\rho_\infty^f)^2\right)\right. \\ \left.-2\rho_\infty^s \left(3 + 2\rho_\infty^f + 3(\rho_\infty^s)^2\right)\big)\big) \omega - 4\xi \big(-\big(-9 + 12\rho_\infty^s - 9(\rho_\infty^s)^2 \\ +2\xi^2 \left(7 - 10\rho_\infty^s + 7(\rho_\infty^s)^2\right)\big) \left(1 + \rho_\infty^f\right)^2 + 3\alpha \left(-1 + 2\xi^2\right) \\ \left(1 + 6\rho_\infty^f + (\rho_\infty^f)^2 + (\rho_\infty^s)^2 \left(1 + 6\rho_\infty^f + (\rho_\infty^f)^2\right)\right. \\ \left.\left.-2\rho_\infty^s \left(3 + 2\rho_\infty^f + 3(\rho_\infty^f)^2\right)\big) \sqrt{\left(-1 + \xi^2\right)\omega^2}\right)\big) / \\ \big(3 \big(8 + 4\rho_\infty^s - 4(\rho_\infty^s)^2 + \alpha \left(1 + 4(\rho_\infty^s)^2 + 6\rho_\infty^f - 3(\rho_\infty^f)^2\right. \\ \left.+\rho_\infty^s \left(-7 - 2\rho_\infty^f + (\rho_\infty^f)^2\right)\big)\big)\big) \end{aligned} \quad (4.29)$$

For the case where $\rho_\infty^s = \rho_\infty^f$ the interpolation of the force does not have any effect, but for cases where $\rho_\infty^s \neq \rho_\infty^f$ this means an improvement of the accuracy. Thus, for the chosen time integration schemes, the interpolation of the force at the interface not only maintains unconditional stability but also second order accuracy.

An overview of the stability and accuracy of the system with and without interpolation of the interface traction force is given in Table 4.1.

4.3 Numerical solution of the 1D model problem

The coupled model problem is solved with and without interpolation of the traction force at the interface. For different combinations of ρ_∞^s, ρ_∞^f, ξ, ω, α and $\Delta t/T$ the results found without traction force interpolation are compared with the results found with traction force interpolation.

Figure 4.10 shows the numerical and analytical solution of the problem for $\rho_\infty^s = 0.3$, $\rho_\infty^f = 0.7$, $\xi = 0.01$, $\omega = 1$, $\alpha = 0.8$ and $\Delta t/T = 1/10$, for respectively the case without and with traction force interpolation. Without the traction force interpolation the numerical solution is stable as expected. However, it suffers excessively from numerical damping. This is improved significantly by interpolating the force at the interface as can be seen in the figure. The same trend is visible in the plots for a similar case ($\rho_\infty^s = 0.3$, $\rho_\infty^f = 0.7$, $\xi = 0.001$, $\omega = 1$, $\alpha = 0.5$ and $\Delta t/T = 1/30$), again without and with traction force interpolation respectively.

For the case where $\rho_\infty^s > \rho_\infty^f$, results for two different combinations of the problem variables are shown as well. The results for $\rho_\infty^s = 0.7$, $\rho_\infty^f = 0.3$, $\xi = 0.01$, $\omega = 1$, $\alpha = 0.8$ and $\Delta t/T = 1/10$ are shown in Figure 4.10, and the results for $\rho_\infty^s = 0.3$, $\rho_\infty^f = 0.7$, $\xi = 0.001$, $\omega = 1$, $\alpha = 0.5$ and $\Delta t/T = 1/30$ are shown in Figure 4.11. Based on the eigenvalue analysis in Section 4.1.2, for these parameters, the numerical solution is expected to be unstable if the traction force is not interpolated at the interface. It can be seen in the figures that the numerical error steadily increases and renders these simulations useless. The improved stability for these cases is demonstrated in Figures 4.10 and 4.11.

From Figures 4.10 and 4.11 it can be seen that both the stability and the accuracy improve when interpolating the traction force at the interface. The improvement of the accuracy is also demonstrated in Figures 4.11, where for $\rho_\infty^s = 0.3$, $\rho_\infty^f = 0.7$, $\xi = 0.01$, $\omega = 1$, $\alpha = 0.5$ and respectively $\Delta t/T = 1/30$ and $\Delta t/T = 1/100$ the results without and with traction force interpolation are plotted. It can be seen that even for small time steps ($\Delta t/T = 1/100$) interpolation of the traction force improves the accuracy.

without interpolation
$\rho^s_\infty = 0.3,\ \rho^f_\infty = 0.7,\ \xi = 0.01$
$\omega = 1,\ \alpha = 0.8,\ \Delta t/T = 1/10$

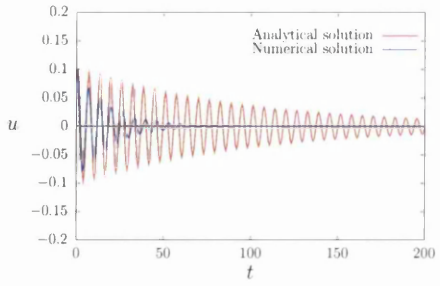

with interpolation
$\rho^s_\infty = 0.3,\ \rho^f_\infty = 0.7,\ \xi = 0.01$
$\omega = 1,\ \alpha = 0.8,\ \Delta t/T = 1/10$

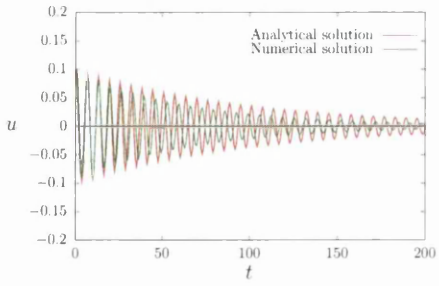

without interpolation
$\rho^s_\infty = 0.3,\ \rho^f_\infty = 0.7,\ \xi = 0.001$
$\omega = 1,\ \alpha = 0.5,\ \Delta t/T = 1/30$

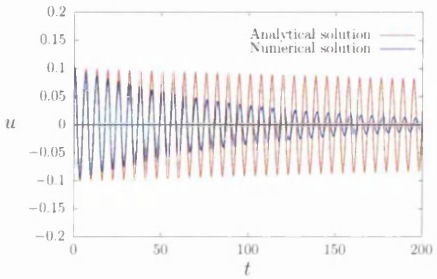

with interpolation
$\rho^s_\infty = 0.3,\ \rho^f_\infty = 0.7,\ \xi = 0.001$
$\omega = 1,\ \alpha = 0.5,\ \Delta t/T = 1/30$

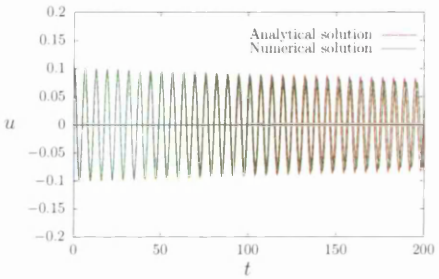

without interpolation
$\rho^s_\infty = 0.7,\ \rho^f_\infty = 0.3,\ \xi = 0.01$
$\omega = 1,\ \alpha = 0.8,\ \Delta t/T = 1/10$

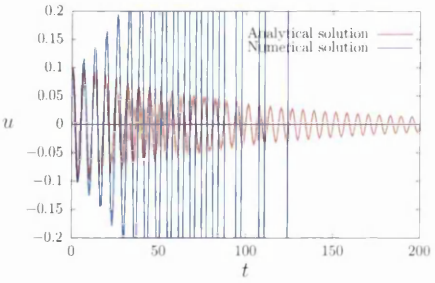

with interpolation
$\rho^s_\infty = 0.7,\ \rho^f_\infty = 0.3,\ \xi = 0.01$
$\omega = 1,\ \alpha = 0.8,\ \Delta t/T = 1/10$

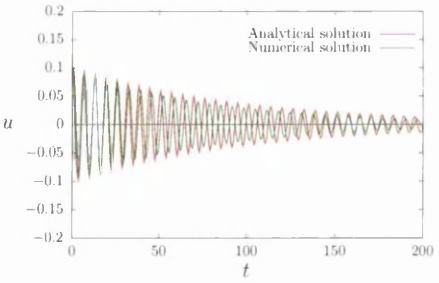

Figure 4.10: Numerical solution of a coupled one degree of freedom second order problem, solved with different time integration schemes for both domains with and without traction force interpolation at the interface.

without interpolation

$\rho^s_\infty = 0.7,\ \rho^f_\infty = 0.3,\ \xi = 0.001$

$\omega = 1,\ \alpha = 0.5,\ \Delta t/T = 1/30$

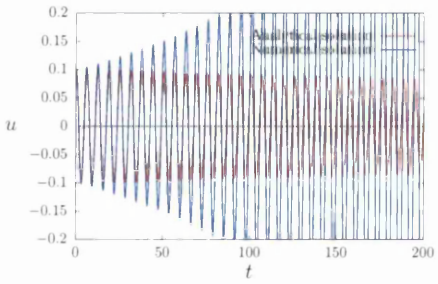

with interpolation

$\rho^s_\infty = 0.7,\ \rho^f_\infty = 0.3,\ \xi = 0.001$

$\omega = 1,\ \alpha = 0.5,\ \Delta t/T = 1/30$

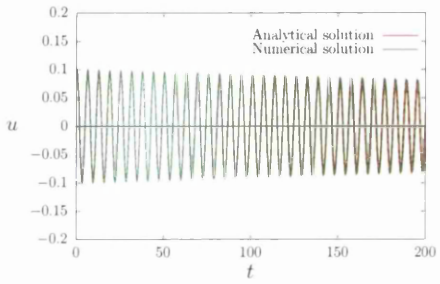

$\rho^s_\infty = 0.3,\ \rho^f_\infty = 0.7,\ \xi = 0.01$

$\omega = 1,\ \alpha = 0.5,\ \Delta t/T = 1/30$

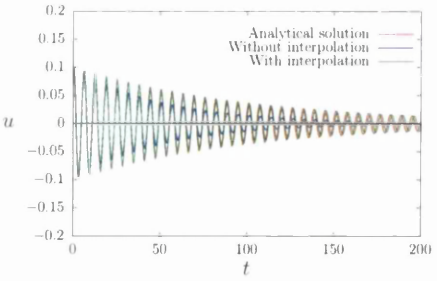

$\rho^s_\infty = 0.3,\ \rho^f_\infty = 0.7,\ \xi = 0.01$

$\omega = 1,\ \alpha = 0.5,\ \Delta t/T = 1/100$

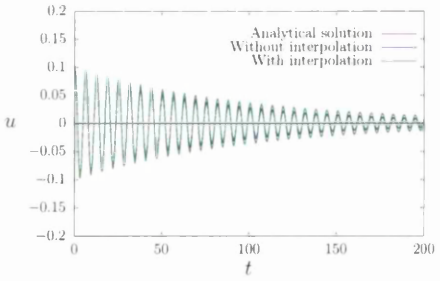

Figure 4.11: Numerical solution of a coupled one degree of freedom second order problem, solved with different time integration schemes for both domains with and without traction force interpolation at the interface.

4.4 Conclusion

It has been shown for a one dimensional model problem that the employment of the two versions of the generalised-α method in a coupled problem can lead to the degrading of accuracy and stability and even failure of the solution strategy. It is believed that such problems are likely to arise in the context of other time integration schemes, too. It has been shown that, for the specific choice of the generalised-α method, unconditional stability and second order accuracy for the linear model problem can be maintained by interpolating the interface traction force within each time step.

Chapter 5

Gauß-Seidel solution procedure for coupled problems

5.1 Introduction

In this chapter the convergence behaviour of the block Gauß-Seidel solution strategy is investigated. The strengths and weaknesses of the Gauß-Seidel strategy are generally well established. However, in this chapter, a simple model problem is used to highlight some aspects which arise in the context of the application of the block Gauß-Seidel method to fluid-structure interaction problems (see also [19, 47–49]). In particular, the failure criteria and the convergence behaviour of the block Gauß-Seidel method are analysed. The benefit that can be derived from relaxation strategies is demonstrated, and the performance of the block Gauß-Seidel method in the presence of physical constraints and nonlinearities is investigated. It is noted that a constraint commonly encountered in the modelling of fluid-structure interaction is the fluid incompressibility. Nonlinearities include the convective acceleration in the balance of momentum of the fluid or nonlinear behaviour of the solid structure.

The model problem is defined in Section 5.2. In Section 5.3, the standard block Gauß-Seidel method is described and its convergence behaviour is analysed. The effects of relaxation and of an incompressibility type constraint are investigated in Sections 5.4 and 5.5, respectively. Finally, the benefits that can be derived from adaptive relaxation for nonlinear problems are demonstrated in Section 5.6.

5.2 The model problem

A one dimensional mass, spring and dashpot system with four degrees of freedom is used to represent a coupled second order initial value problem. Two degrees of freedom represent one domain s and the other two degrees of freedom represent the domain f of the coupled problem. A schematic view of the model problem is shown in Figure 5.1. The interaction of the two domains occurs between the masses that are denoted as m_2^s and m_2^f. Furthermore:

$$k^s = k \,, \qquad k^f = \alpha_k \, k \,, \tag{5.1}$$

and

$$m_1^s = m \,, \qquad m_2^s = \frac{m}{2} \,, \qquad m_1^f = \alpha_m \, m \,, \qquad m_2^f = \frac{\alpha_m \, m}{2} \,. \tag{5.2}$$

Thus, the parameters that define the problem are the stiffness k, the viscosity c, the mass m and the dimensionless parameters α_k and α_m. It follows that α_k and α_m are defined as

$$\alpha_k = \frac{k^f}{k^s}, \qquad \alpha_m = \frac{m_1^f}{m_1^s}. \tag{5.3}$$

The displacements of the mass points m_1^s, m_2^s, m_1^f and m_2^f are represented by respectively u_1^s, u_2^s, u_1^f and u_2^f. The force which is exerted by mass point m_2^f onto m_2^s is represented by F^s. The dynamic behaviour of subsystem s can be described with the following governing equations

$$m_1^s \, \ddot{u}_1^s \; + \; k^s \, u_1^s \; - \; k^s \, (u_2^s - u_1^s) \;\; = \;\; 0 \tag{5.4}$$

$$m_2^s \, \ddot{u}_2^s \; + \; k^s \, (u_2^s - u_1^s) \;\; = \;\; F^s \,. \tag{5.5}$$

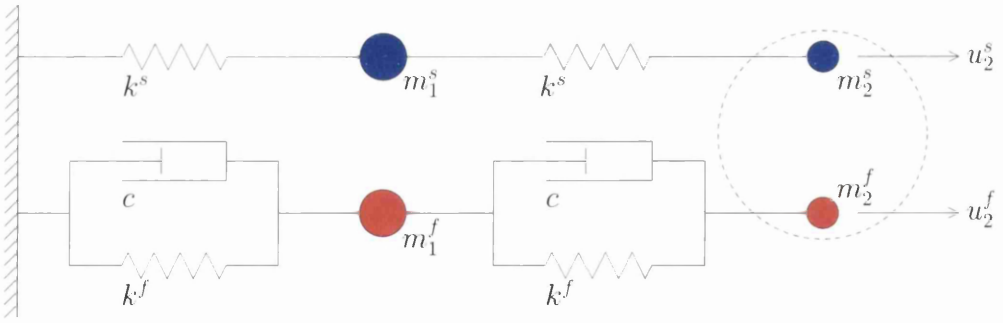

Figure 5.1: The model problem.

For subsystem f, where F^f represents the force exerted by m_2^s onto m_2^f, the governing equations can be written as follows

$$m_1^f \ddot{u}_1^f + c^f \dot{u}_1^f - c^f (\dot{u}_2^f - \dot{u}_1^f) + k^f u_1^f - k^f (u_2^f - u_1^f) = 0 \quad (5.6)$$

$$m_2^f \ddot{u}_2^f + c^f (\dot{u}_2^f - \dot{u}_1^f) + k^f (u_2^f - u_1^f) = F^f . \quad (5.7)$$

Domain s and domain f interact with each other at the interface between mass points m_2^s and m_2^f. To solve the coupled problem interface conditions are needed. Kinematical consistency at the interface requires that

$$u_2^s = u_2^f \quad \forall \quad t \in I , \quad (5.8)$$

whereby I denotes the time interval of interest. Equilibrium of the interface traction forces requires that

$$F^s + F^f = 0 \quad \forall \quad t \in I . \quad (5.9)$$

The uncoupled equivalent of the model problem is used in order to get a reference solution and to obtain the characteristic time periods of the problem. For the uncoupled problem, mass points m_2^s and m_2^f are merged together into mass point m_2^i, which leads to

$$m_2^i = \frac{m + \alpha m}{2}. \quad (5.10)$$

The maximum and minimum characteristic time periods T_{max} and T_{min} are obtained by solving the eigenvalue problem, where

$$T_{max} = \frac{2\pi}{\sqrt{\lambda_{min}}}, \qquad T_{min} = \frac{2\pi}{\sqrt{\lambda_{max}}} \quad (5.11)$$

with λ_{min} and λ_{max} respectively the minimum and maximum eigenvalue.

5.3 Stability analysis

The employment of the block Gauß-Seidel solution strategy for the solution of a coupled problem requires that the domains are solved separately. The interaction between the two domains is achieved by communicating the interface force and the interface displacement. Thus, the algorithm consists of two steps: Based on an estimate of the interface displacement, the domain f

is solved for the interface force, which it exerts onto domain s. Subsequently, this force is applied to domain s as an external load, and domain s is solved for the interface displacement. This is then used as an improved estimate of the interface displacement, and the process is repeated until the desired accuracy is achieved. The algorithm is visualised in Figure 5.2. In the context of fluid-structure interaction, it is normally the fluid which is solved for the interface traction forces (here system f) and the solid which is solved for the interface displacements (here system s).

5.3.1 Generic formulation

To analyse the stability of the coupled problem, the algorithm is captured in one generic expression that can be used to obtain a convergence criterion. Governing Equations (5.4) – (5.9) are solved using an appropiate implicit time integration scheme. It is chosen to consider the single step time integration schemes as described in Chapter 3. Any of these time integration schemes can be written in the following form:

$$u_{n+\gamma} = L^{(0)}(u_{n+1}, u_n, \dot{u}_n, \ddot{u}_n) \tag{5.12}$$
$$\dot{u}_{n+\gamma} = L^{(1)}(u_{n+1}, u_n, \dot{u}_n, \ddot{u}_n) \tag{5.13}$$
$$\ddot{u}_{n+\gamma} = L^{(2)}(u_{n+1}, u_n, \dot{u}_n, \ddot{u}_n) \tag{5.14}$$
$$\dot{u}_{n+1} = L^{(3)}(u_{n+1}, u_n, \dot{u}_n, \ddot{u}_n) \tag{5.15}$$
$$\ddot{u}_{n+1} = L^{(4)}(u_{n+1}, u_n, \dot{u}_n, \ddot{u}_n)\ . \tag{5.16}$$

where u represents any of the solution variables, the subscripts n and $n+1$ denote quantities associated with the time instances t_n and t_{n+1}, respectively,

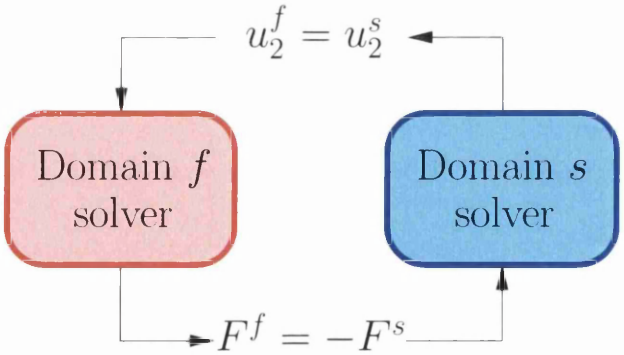

Figure 5.2: Schematic representation of the block Gauß-Seidel procedure.

and $L^{(i)}(\bullet)$, $i = 0, 1, 2, ...$ are linear combinations of their arguments. The parameter γ satisfies $0 < \gamma \leq 1$, and therefore, $t_{n+\gamma}$ denotes a time instance between t_n and t_{n+1}.

The time discretisation as given by (5.12) – (5.16) is applied to all degrees of freedom of the model problem. Given the solution at time instant t_n, the Equations (5.4) – (5.7) may then be formulated at $t_{n+\gamma}$ in terms of the unknowns $u^s_{1,n+1}$, $u^s_{2,n+1}$, $u^f_{1,n+1}$ and $u^f_{2,n+1}$. This leads to, respectively,

$$R^s_1(u^s_{1,n+1}, u^s_{2,n+1}) = 0 \tag{5.17}$$

$$R^s_2(u^s_{1,n+1}, u^s_{2,n+1}) = F^s_{n+\gamma} \tag{5.18}$$

$$R^f_1(u^f_{1,n+1}, u^f_{2,n+1}) = 0 \tag{5.19}$$

$$R^f_2(u^f_{1,n+1}, u^f_{2,n+1}) = F^f_{n+\gamma}\,. \tag{5.20}$$

With Equations (5.8) and (5.9), it follows that

$$u^s_{2,n+1} = u^f_{2,n+1} \qquad \text{and} \qquad F^s_{n+\gamma} = -F^f_{n+\gamma}\,. \tag{5.21}$$

The Equations (5.17) and (5.18) represent the fully discretised subsystem s, whereas (5.19) and (5.20) represent subsystem f and $(5.21)_1$ and $(5.21)_2$ describe the strong coupling.

Given the solution at t_n, the block Gauß-Seidel procedure may then be described by the following algorithm:

- guess the displacement $u^s_{2,n+1}$
- set $u^f_{2,n+1} = u^s_{2,n+1}$ and solve system f [Eqs.(5.19),(5.20)] for $u^f_{1,n+1}$ and $F^f_{n+\gamma}$
- set $F^s_{n+\gamma} = -F^f_{n+\gamma}$ and solve system s [Eqs.(5.17),(5.18)] for $u^s_{1,n+1}$ and $u^s_{2,n+1}$
- if the desired accuracy is not met, *i. e.* $|u^s_{2,n+1} - u^f_{2,n+1}| > tol$, go to step 2
- perform time updates [Eqs.(5.15),(5.16)] and proceed with next time step

The simplicity of the Equations (5.17) - (5.21) allows for the analysis of this procedure by eliminating $u^s_{1,n+1}$ from the subsystem (5.17),(5.18). Similarly, $u^f_{1,n+1}$ is eliminated from (5.19) and (5.20). Thus, the following is obtained:

$$\widetilde{s}(u^s_{2,n+1}) \;=\; F^s_{n+\gamma} \qquad \text{and} \qquad \widetilde{f}(u^f_{2,n+1}) \;=\; F^f_{n+\gamma}\,, \tag{5.22}$$

where $\widetilde{s}$ and $\widetilde{f}$ represent linear functions of their arguments. If $\widetilde{s}^{\text{inv}}$ denotes the inverse function of $\widetilde{s}$, the algorithm that describes the block Gauß-Seidel procedure may be summarised briefly as

$$u^{s\ (i+1)}_{2,n+1} \;=\; \widetilde{s}^{\text{inv}}\left(-\,\widetilde{f}\left(u^{s\ (i)}_{2,n+1}\right)\right)\,. \tag{5.23}$$

where the superscripts i and $i+1$ represent the iteration counter of the Gauß-Seidel procedure. Due to the linearity of the problem the expression in (5.23) is found to have the following format

$$u^{s\ (i+1)}_{2,n+1} \;=\; A\,u^{s\ (i)}_{2,n+1} + \;\mathbf{B}\,\mathbf{u}_n\,. \tag{5.24}$$

The scalar coefficient A, which is also known as the growth factor, depends exclusively on the time step size $\Delta t = t_{n+1} - t_n$ and the problem parameters k, c, m and α_k and α_m. The same holds for the coefficients of the vector $\mathbf{B}$. The vector $\mathbf{u}_n$ contains all solution variables of the previous time instant t_n.

Clearly, for convergence of a system that can be described by an expression of the form of Equation (5.24), only the value of A is important. Convergence is obtained only if $|A| < 1$ (see also Theorem 5.1-1 in [50]). Provided that this is the case, any error in $u^{s\ (i)}_{2,n+1}$ is reduced from one iteration step to the next, and linear convergence is achieved. In particular, for $-1 < A < 0$, the sequence of solution variables represents a damped oscillation which converges towards the exact solution of the discretised problem. For $0 < A < 1$, the sequence of solution variables follows monotonic decay. Finally, for $A = 0$, the exact solution is obtained within one iteration step. The coefficients of $\mathbf{B}$ are not relevant for the convergence behaviour, but they determine the solution value. By setting $u^{s\ (i+1)}_{2,n+1} = u^{s\ (i)}_{2,n+1}$ and manipulating (5.24) it can be easily shown that the solution converges to

$$\lim_{i\to\infty} u^{s\ (i)}_{2,n+1} = \frac{\mathbf{B}\,\mathbf{u}_n}{1-A}, \quad \text{if} \quad |A| < 1\,. \tag{5.25}$$

In the following two subsections expressions for the coefficient A are derived for two standard time integration schemes, which differ in terms of accuracy and numerical damping.

5.3.2 Backward Euler

To derive the expression for the coefficient A for the Backward Euler method, Equation (3.1) and (3.2) from Section 3.1 are rewritten in the following form

$$\dot{u}_{n+1} = \frac{1}{\Delta t}(u_{n+1} - u_n) \tag{5.26}$$

$$\ddot{u}_{n+1} = \frac{1}{\Delta t^2}(u_{n+1} - u_n) - \frac{1}{\Delta t}\dot{u}_n \tag{5.27}$$

Applying (5.26) and (5.27) to all solution variables, the governing equations (5.4) - (5.9) can then be formulated at the time instance t_{n+1} with the displacements and forces at t_{n+1} as the only unknowns.

Next, the procedure outlined in Section 5.3.1 is followed to obtain an expression in the format of (5.24). The growth factor A may then be written as

$$A = -\frac{(m + 2k\Delta t^2)\left(m^2\alpha_m^2 + 4m\alpha_m\Delta t\,(c + k\alpha_k\Delta t) + 2\Delta t^2\,(c + k\alpha_k\Delta t)^2\right)}{(m^2 + 4km\Delta t^2 + 2k^2\Delta t^4)\,(m\alpha_m + 2\Delta t\,(c + k\alpha_k\Delta t))}. \tag{5.28}$$

The value of A depends on Δt and on all problem parameters m, c, k, α_m and α_k. With all these quantities being non-negative, it follows from (5.28) that the coefficient A is always negative. Therefore, the sequence of solution values oscillates as it approaches the final solution. The value of A for a range of $\Delta t/T$ for $\alpha_m = 0.25$, $\alpha_m = 0.5$, $\alpha_m = 1.0$ and $\alpha_m = 2.0$ is shown in Figure 5.3.

Since small time steps are needed to ensure a certain accuracy of the simulations, we determine the limit of A as Δt tends to zero. The following simple expression is obtained:

$$\lim_{\Delta t \to 0} A = -\alpha_m \tag{5.29}$$

Interestingly, the limit for $\Delta t \to \infty$ is obtained as

$$\lim_{\Delta t \to \infty} A = -\alpha_k \tag{5.30}$$

Thus, for small time steps, the convergence properties of the iterative scheme depend only on the value of α_m, which represents the ratio between the mass of system f and the mass of the system s. For convergence, $|A| < 1$ is required. Therefore, it is concluded that, for small time steps, the block

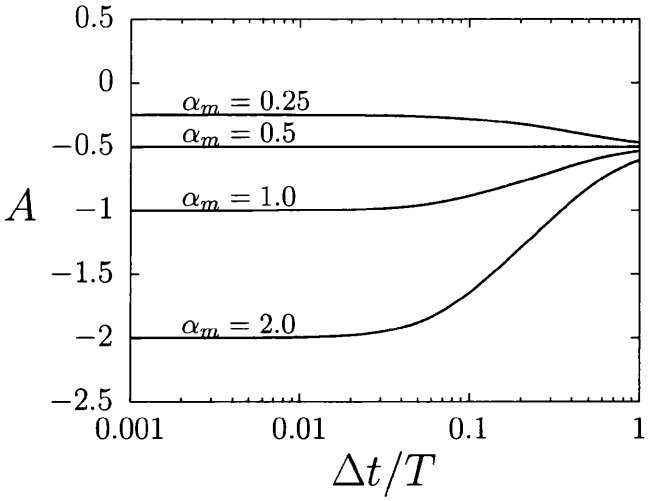

Figure 5.3: Dependency of the convergence factor A on the time step size Δt for the backward Euler method.

Gauß-Seidel scheme is convergent only if $\alpha_m < 1$, *i. e.* if the masses in system f (solved for the interface force) are smaller than those of system s (solved for the interface displacement). For larger time steps it may be expected the ratio of the stiffnesses α_k to gain influence. This explains the observation that convergence is sometimes obtained for larger rather than smaller time steps.

5.3.3 Trapezoidal rule

The trapezoidal rule, defined in Section 3.2 by equations 3.3 to 3.7, is rewritten as follows:

$$u_{n+\frac{1}{2}} = \frac{1}{2}(u_{n+1} + u_n) \tag{5.31}$$

$$\dot{u}_{n+\frac{1}{2}} = \frac{1}{\Delta t}(u_{n+1} - u_n) \tag{5.32}$$

$$\ddot{u}_{n+\frac{1}{2}} = \frac{2}{\Delta t^2}(u_{n+1} - u_n) - \frac{2}{\Delta t}\dot{u}_n \tag{5.33}$$

$$\dot{u}_{n+1} = \frac{2}{\Delta t}(u_{n+1} - u_n) - \dot{u}_n \,. \tag{5.34}$$

The Equations (5.31) – (5.34), which correspond to the generic expressions (5.12) – (5.15), may be employed to integrate all solution variables over the

time domain. The procedure outlined in Section 5.3.1 can then be followed and applied to the formulation based on the backward Euler scheme in Section 5.3.2 to derive an expression for the growth factor A, which leads to

$$A = -\frac{(2m + k\Delta t^2)\left(8m^2\alpha_m^2 + 8m\alpha_m\Delta t\,(2c + k\alpha_k\Delta t) + \Delta t^2\,(2c + k\alpha_k\Delta t)^2\right)}{(8m^2 + 8km\Delta t^2 + k^2\Delta t^4)\,(2m\alpha_m + \Delta t\,(2c + k\alpha_k\Delta t))} \,. \tag{5.35}$$

This expression differs from the one in (5.28) only in terms of some numerical coefficients. The value of A as a function of $\Delta t/T$ for different values of α_m is shown in Figure 5.4. Similar to (5.29) and (5.30) it is found that

$$\lim_{\Delta t \to 0} A \;=\; -\,\alpha_m \tag{5.36}$$

and

$$\lim_{\Delta t \to \infty} A \;=\; -\,\alpha_k \,. \tag{5.37}$$

Thus, the same qualitative convergence behaviour can be expected as for the formulation based on the backward Euler time integration scheme.

5.3.4 Numerical example

The model problem is solved numerically for the backward Euler method and the trapezoidal rule, in order to compare the analytical value of A with numerical results. The problem parameters are chosen as

$$m = 40\,, \qquad c = 0.05\,, \qquad k = 80\,, \qquad \alpha_k = 0.5\,. \tag{5.38}$$

Four different values of α_m are considered. Based on this set of parameters, the highest eigenfrequency $\omega_{\max}$ of the model problem can be calculated. The associated time periods are obtained as $T = 2\,\pi\,/\,\omega_{\max} = \pi/\sqrt{2}$ for $\alpha_m = 0.25$ and $T = \pi$ for $\alpha_m = 0.5$, $\alpha_m = 1$ and $\alpha_m = 2$. The initial displacements and velocities are all set to zero except for $u^s_{1,0} = 1$. The problem can then be simulated for different values of α_m and different ratios $\Delta t/T$. The accuracy of a set of solution variables is measured in terms of the difference of the interface forces, *i. e.* the forces $F^s_{n+\gamma}$ and $F^f_{n+\gamma}$, as obtained from an interface displacement $u^s_{2,n+1} = u^f_{2,n+1}$. Table 5.1 shows the average number of iterations required to achieve

$$|\,F^s_{n+\gamma} \;-\; F^f_{n+\gamma}\,| < 10^{-6} \tag{5.39}$$

during the time interval $[0, T_{\max}]$ with $T_{\max} = 3\pi$, $T_{\max} = 3\pi$, $T_{\max} = 3\sqrt{2}\pi$ and $T_{\max} = 6\pi$ for $\alpha_m = 0.25$, $\alpha_m = 0.5$, $\alpha_m = 1$ and $\alpha_m = 2$, respectively.

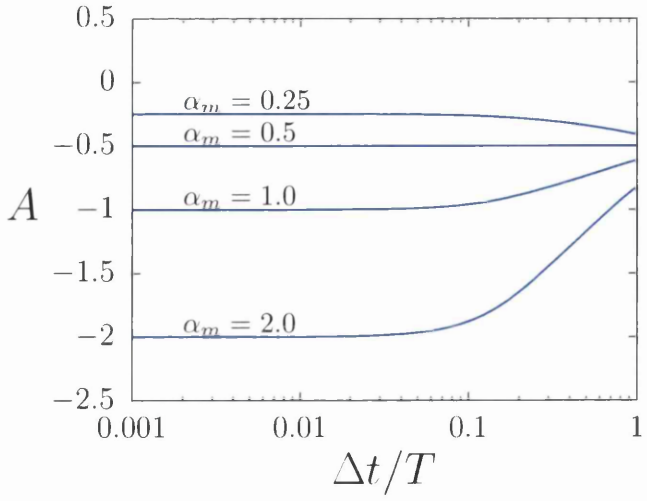

Figure 5.4: Dependency of the convergence factor A on the time step size Δt for the trapezoidal rule.

The time interval corresponds to three time the time period associated with the lowest eigenfrequency. The failure to achieve Equation (5.39) within 5000 iteration steps is regarded as failure of the algorithm. The predicted limit behaviour of A based on Figures 5.3 and 5.4 is clearly visible. The comparison of the diagrams based on the two different time integration schemes shows that, for the trapezoidal rule, the transition of A from $-\alpha_m$ to $-\alpha_k$ is slightly shifted towards larger values of Δt. This is due to the higher order of accuracy of the method. The diagram is consistent with Table 5.1 in the sense that convergence is fast when $|A|$ is small and fails when $|A|$ is larger or equal to one.

α_m	$\Delta t/T$								
	1/1000			1/100			1/10		
	BE		TR	BE		TR	BE		TR
0.25	15.7	<	16.3	13.9	<	14.5	13.0	<	13.4
0.5	31.8	<	32.9	27.8	<	29.6	23.5	<	26.3
1	x		x	x		x	129.8	<	440.4
2	x		x	x		x	x		x

Table 5.1: Average number of iterations for the standard block Gauß-Seidel strategy.

5.3.5 Reverse order of subsystems

As stated above, convergence of the block Gauß-Seidel method is conditional on $|A| < 1$. In the previous subsections it has been shown that, for the standard version of the methodology, the limits of $|A|$ for small and for large time steps are α_m and α_k, respectively. Therefore, these parameters (most importantly α_m) need to be smaller than one. Reversing the order of the subsystems, *i. e.* solving system s for the interface force and solving system f for the interface displacement, corresponds to inverting α_m and α_k. This renders the well known result that the order of the subsystems or equations in a Gauß-Seidel procedure is essential to determine the efficiency or even the success or failure of the method (see *e. g.* [11]). In the next section, the improvement of the methodology by means of relaxation is discussed, which can be used to achieve and enhance convergence even in cases where the systems are "in the wrong order".

5.4 Relaxation

The simplest form of relaxation consists in a modified update of the solution variable between two iteration cycles. Rather than using the most recent value of the solution variable, a specified proportion of the increment is added to the previous value of the solution variable. In terms of the model problem, an additional step is inserted

$$u^s_{2,n+1} \leftarrow (1-\beta)\, u^s_{2,n+1} + \beta\, u^f_{2,n+1}\,, \tag{5.40}$$

where β is a scalar parameter which needs to be chosen appropriately. Clearly, for $\beta = 0$, the algorithm is unchanged. With (5.40), Equation (5.23) becomes

$$u^{s\ (i+1)}_{2,n+1} = (1-\beta)\ \widetilde{s}^{\mathrm{inv}}\Big(-\widetilde{f}\Big(u^{s\ (i)}_{2,n+1}\Big)\Big) + \beta\, u^{s\ (i)}_{2,n+1}, \tag{5.41}$$

and Equation (5.24) transforms to

$$\begin{aligned} u^{s\ (i+1)}_{2,n+1} &= (1-\beta)\ \Big(A\, u^{s\ (i)}_{2,n+1} + \mathbf{B}\,\mathbf{u}_n\Big) + \beta\, u^{s\ (i)}_{2,n+1} \\ &= ((1-\beta)\,A + \beta)\ u^{s\ (i)}_{2,n+1} + (1-\beta)\,\mathbf{B}\,\mathbf{u}_n\,. \end{aligned} \tag{5.42}$$

By setting $u^{s\ (i+1)}_{2,n+1} = u^{s\ (i)}_{2,n+1}$ and manipulating (5.42) it is confirmed that the limit of the solution value is the same as in Equation (5.25), convergence provided. The criteria for convergence now reads

$$|A_{\mathrm{relax}}| < 1 \qquad \text{with} \qquad A_{\mathrm{relax}} = (1-\beta)\,A + \beta\,. \tag{5.43}$$

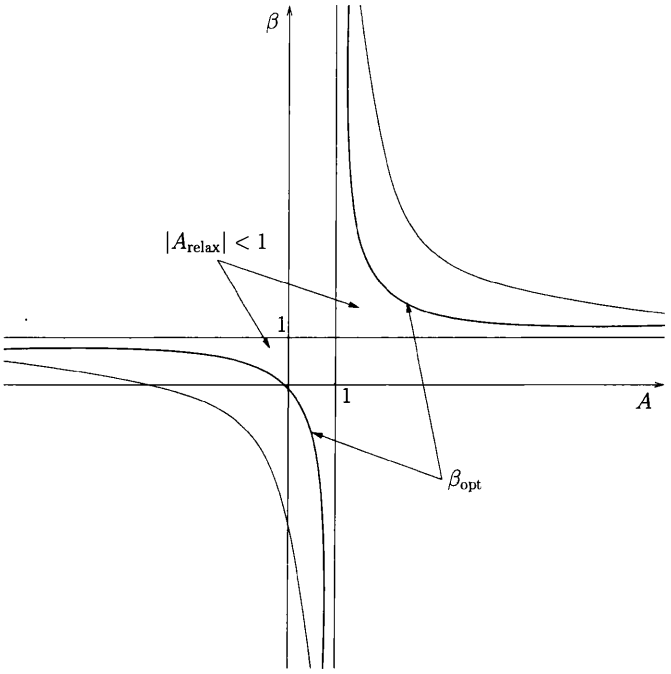

Figure 5.5: Convergence regions for the relaxation parameter.

It follows from (5.43) that, for the convergent solution, it is necessary that

$$\begin{aligned} \tfrac{A+1}{A-1} < \beta < 1 \qquad &\text{for} \qquad A < 1 \\ \text{and} \qquad 1 < \beta < \tfrac{A+1}{A-1} \qquad &\text{for} \qquad A > 1\,. \end{aligned} \tag{5.44}$$

Thus, for any $A \neq 1$, there exists a range of values β such that (5.43) is satisfied and convergence is guaranteed (see Figure 5.5). Furthermore, it is noted that it follows with (5.36) and (5.37), respectively, that

$$\lim_{\Delta t \to 0} A_{\text{relax}} = (1-\beta)(-\alpha_m) + \beta \tag{5.45}$$

and

$$\lim_{\Delta t \to \infty} A_{\text{relax}} = (1-\beta)(-\alpha_k) + \beta\,. \tag{5.46}$$

The value of A_{relax} for different values of α_m and relaxation parameter $\beta = 0.5$ is calculated and shown in Figure 5.6. Also, the model problem is again solved numerically, for the same problem parameters as in the previous

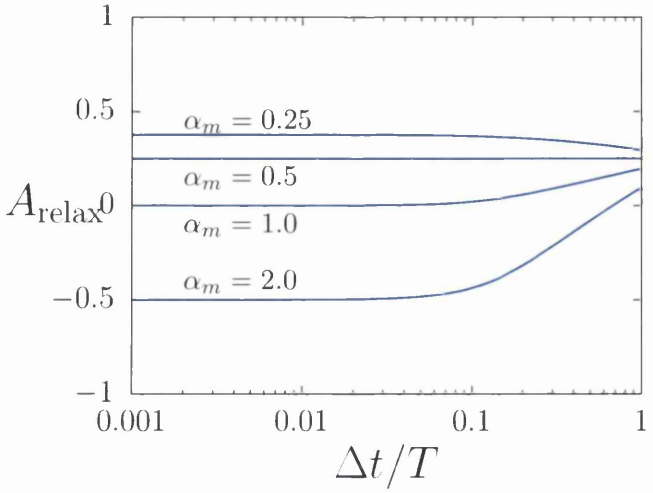

Figure 5.6: The coefficient A_{relax} for different values of α_m based on the trapezoidal rule with constant relaxation $\beta = 0.5$.

section, using the trapezoidal rule time integration scheme. By following the same procedure as described in the previous numerical example, the results displayed in Table 5.2 are obtained. Clearly, convergence is now achieved for all values of α_m. Note from Figure 5.6 that A_{relax} is positive in some cases and therefore the convergence of the associated solution sequences is monotonic. For $\alpha_m = 1$, A_{relax} is approximately equal to zero over a wide range of Δt. This renders the converged solution value after only one or two iterations.

α_m	$\Delta t/T$		
	1/1000	1/100	1/10
0.25	23.1	20.8	18.0
0.5	16.2	14.6	12.9
1	1.0	2.0	4.3
2	33.3	29.9	22.2

Table 5.2: Results of the simulations for the trapezoidal rule with relaxation ($\beta = 0.5$)

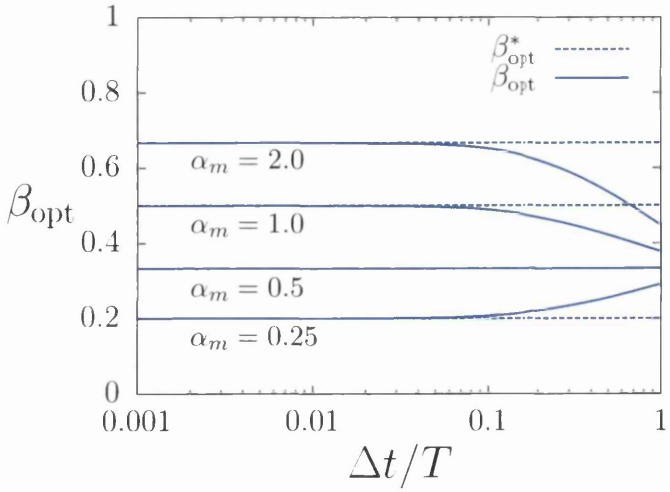

Figure 5.7: Dependency of β_{opt} on $\Delta t/T$.

5.4.1 Optimal relaxation parameter

For $A \neq 1$, there exists a value β_{opt} such that $A_{\text{relax}} = 0$. Thus, the choice $\beta = \beta_{\text{opt}}$ renders the exact solution after one iteration step. From Equation $(5.43)_2$ the following can be obtained:

$$\beta_{\text{opt}} = \frac{A}{A-1} , \tag{5.47}$$

which is illustrated in Figure 5.5. The exact expression for A is generally not available unless a simple model problem is considered. Therefore, β^*_{opt} is introduced, which is based on the limit of A as $\Delta t \to 0$ (see Eq.(5.36)), *i. e.*

$$\beta^*_{\text{opt}} = \frac{\alpha_m}{\alpha_m + 1} . \tag{5.48}$$

It is expected that setting $\beta = \beta^*_{\text{opt}}$ requires a small number of iteration steps to achieve a high degree of accuracy.

The example is based on the trapezoidal rule and employs the problem parameters used in the previous examples. The diagram in Figure 5.7 illustrates the variation of β_{opt} with the time step size $\Delta t/T$. Within the range of reasonable time step sizes $\Delta t/T < 1/30$, the coefficient β^*_{opt} represents an excellent approximation of the exact value β_{opt}. The diagrams in Figure 5.8 show the variation of A_{relax} with the relaxation parameter β for $\Delta t/T = 1/30$.

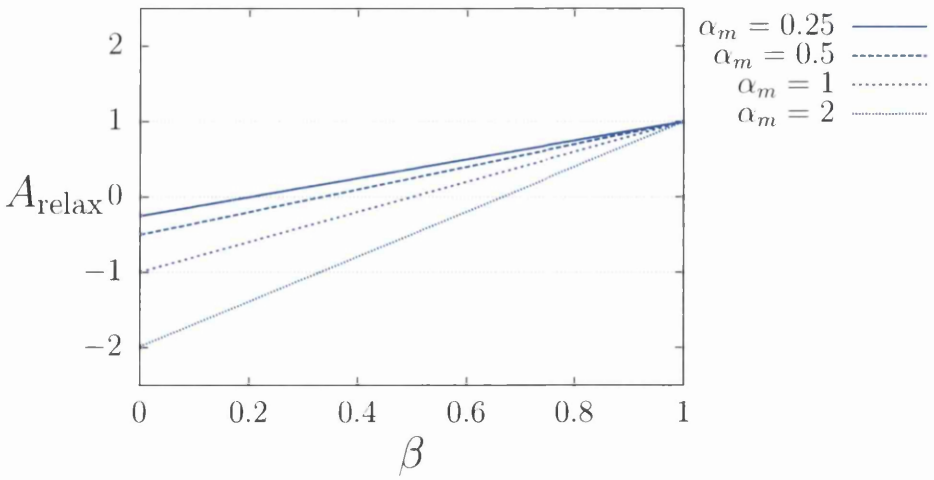

Figure 5.8: Dependency of A_{relax} on the relaxation factor β for $\Delta t/T = 1/30$.

The numbers of iterations required to achieve the accuracy defined by (5.39) are shown in Table 5.3. As expected, the choice $\beta = \beta_{\text{opt}}$ renders the converged solution after one step, whereas $\beta = \beta^*_{\text{opt}}$ requires a small number of iteration steps.

α_m	β_{opt}	n	β^*_{opt}	n
0.25	0.200923	1.0	1/5	2.4
0.5	0.33339	1.0	1/3	1.8
1	0.498684	1.0	1/2	2.9
2	0.664876	1.0	2/3	3.0

Table 5.3: Values of β_{opt} and β^*_{opt} and associated numbers of iterations for $\Delta t/T = 1/30$.

5.5 Convergence in the presence of a constraint

In this section the convergence behaviour of the block Gauß-Seidel method in the presence of a physical constraint imposed on the solution variables is investigated. In realistic fluid-structure interaction simulations, a constraint such as the incompressibility of the fluid is often accounted for by employing

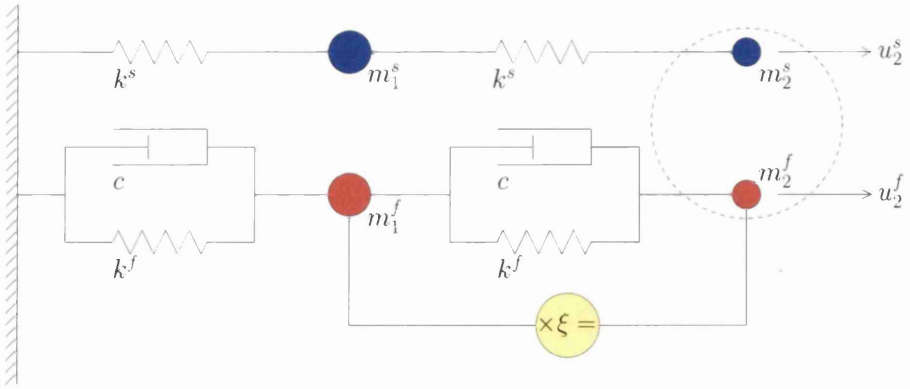

Figure 5.9: The model problem with constraint $u_2^f = \xi u_1^f$.

Lagrangian multipliers. The equations which describe the solution in the subdomain where the constraint is active may then be rephrased as the following variational problem: In the appropriate mathematical spaces, find u and λ such that, for all admissible δu and $\delta\lambda$,

$$a(\delta u, u) \; + \; b(\delta u, \lambda) \; + \; b(u, \delta\lambda) \; = \; F(\delta u) \tag{5.49}$$

is satisfied. The expression $a(\delta u, u) = F(\delta u)$ corresponds to the unconstrained problem. The Lagrangian multiplier is denoted by λ, while δu and $\delta\lambda$ represent the variational counterparts of u and λ, respectively. The term $b(\bullet, \bullet)$ is defined as

$$b(u, \lambda) \; = \; \int_\Omega \mathcal{L}(u)\, \lambda \, \mathrm{d}v \; , \tag{5.50}$$

where $\mathcal{L}(u) = 0$ is the original constraint imposed on the solution variable u, and Ω represents the respective subdomain of the problem.

The constraint that is chosen and imposed on the model problem is

$$\xi \; u_1^f \; - \; u_2^f \; = \; 0 \quad \forall \; t \in I \; , \tag{5.51}$$

where ξ is a known scalar parameter and I is the time interval of interest. The constraint is visualised in Figure 5.9. It is noted that the nature of this constraint corresponds to incompressibility in the sense that any motion of mass point m_2^f causes motion of mass point m_1^f, *i. e.* a wave travels without any delay between m_2^f on m_1^f, similarly to pressure waves in an incompressible fluid.

Following the strategy based on Lagrangian multipliers a set of three equations which govern the modified subsystem f is obtained

$$m_1^f \ddot{u}_1^f + c^f \dot{u}_1^f - c^f(\dot{u}_2^f - \dot{u}_1^f) + k^f u_1^f - k^f(u_2^f - u_1^f) + \xi\lambda = 0 \quad (5.52)$$

$$m_2^f \ddot{u}_2^f + c^f(\dot{u}_2^f - \dot{u}_1^f) + k^f(u_2^f - u_1^f) - \lambda = F^f \quad (5.53)$$

$$\xi u_1^f - u_2^f = 0. \quad (5.54)$$

These equations replace (5.6) and (5.7) such that the problem is now described by (5.4), (5.5), (5.8), (5.9) and (5.52) – (5.54), where λ is an additional unknown. After the discretisation of the time domain, this may be written, instead of (5.19) and (5.20),

$$R_1^f(u_{1,n+1}^f, u_{2,n+1}^f, \lambda) = 0 \quad (5.55)$$

$$R_2^f(u_{1,n+1}^f, u_{2,n+1}^f, \lambda) = F_{n+\gamma}^f \quad (5.56)$$

$$R_3^f(u_{1,n+1}^f, u_{2,n+1}^f) = 0\,, \quad (5.57)$$

which follow from (5.52) – (5.54), respectively. Thus, the second step in the algorithm for the block Gauß-Seidel method, as given in Section 5.3.1, now reads

- set $u_{2,n+1}^f = u_{2,n+1}^s$ and solve system f [Eqs.(5.55) – (5.57)] for λ, $u_{1,n+1}^f$ and $F_{n+\gamma}^f$

An elimination process similar to the one described in Section 5.3.1 can be used to derive a counterpart of Equation (5.24). The following is obtained

$$u_{2,n+1}^{s\ (i+1)} = \widehat{A}\, u_{2,n+1}^{s\ (i)} + \widehat{\mathbf{B}}\, \mathbf{u}_n\,, \quad (5.58)$$

or, with relaxation, similar to (5.42)

$$u_{2,n+1}^{s\ (i+1)} = \left((1-\beta)\,\widehat{A} + \beta\right)\, u_{2,n+1}^{s\ (i)} + (1-\beta)\,\widehat{\mathbf{B}}\,\mathbf{u}_n\,. \quad (5.59)$$

It is rather tedious, but straightforward to derive expressions for the coefficient $\widehat{A}$ based on the backward Euler and the trapezoidal rule time integration schemes. The resulting terms are lengthy and therefore not presented here. However, similarly to the situation without the constraint, the limits of $\widehat{A}$ associated with $\Delta t \to 0$ and with $\Delta t \to \infty$, respectively, are identical for the two time integration schemes considered. It is obtained that

$$\lim_{\Delta t \to 0} \widehat{A} = -\alpha_m \frac{2+\xi^2}{\xi^2} = \left(\lim_{\Delta t \to 0} A\right) \frac{2+\xi^2}{\xi^2} \quad (5.60)$$

and

$$\lim_{\Delta t \to \infty} \widehat{A} \;=\; -\,\alpha_k \,\frac{2+\xi^2}{\xi^2} \;=\; \Big(\lim_{\Delta t \to \infty} A\Big)\,\frac{2+\xi^2}{\xi^2}\,, \tag{5.61}$$

where (5.36) and (5.37) have been recalled. Thus, the limits of the coefficient $\widehat{A}$ are equal to those associated with the unconstrained problem multiplied by the term $(2+\xi^2)/\xi^2$. Interestingly, it is noted that, for any scalar ξ,

$$\frac{2+\xi^2}{\xi^2} \;>\; 1\,. \tag{5.62}$$

It is concluded that, at least in the limits considered above, $|\widehat{A}| > |A|$ for any value of ξ. Therefore, the presence of the constraint (5.51) has a detrimental effect on the convergence properties of the scheme for any value of ξ. In many cases, $|\widehat{A}| > 1$, even though $|A| < 1$, and thus, the constraint causes the convergence failure. The careful choice of the relaxation parameter β is even more important than it is for the unconstrained problem. Hence, for the scheme with relaxation, we obtain

$$\lim_{\Delta t \to 0} \widehat{A}_{\text{relax}} \;=\; (1-\beta)\,(-\alpha_m)\,\frac{2+\xi^2}{\xi^2} \;+\; \beta \tag{5.63}$$

and

$$\lim_{\Delta t \to \infty} \widehat{A}_{\text{relax}} \;=\; (1-\beta)\,(-\alpha_k)\,\frac{2+\xi^2}{\xi^2} \;+\; \beta \tag{5.64}$$

It is straightforward to derive expressions for β_{opt} and β^*_{opt} which account for the constraint. The effect of using these values for the model problem is equally beneficial as demonstrated in Section 5.4.1 for the unconstrained problem.

For the numerical solution of the model problem, the parameter ξ is set to $\xi = 2$ and otherwise the same parameters as in the previous examples are chosen. The constraint changes the eigenfrequencies of the model problem. The highest eigenfrequency is now associated with $T = \sqrt{5/3}\,\pi$ for all values α_m considered. Relaxation with $\beta = 0.5$ is employed and the trapezoidal rule for the integration of time is used. The simulation is performed for different ratios $\Delta t/T$. The numbers of iterations required to achieve the desired accuracy as given by (5.39) are presented in Table 5.4. The diagrams in Figure 5.10 show $\widehat{A}_{\text{relax}}$ as a function of $\Delta t/T$. The limit behaviour as described by (5.63) and (5.64) is easily observed.

$\Delta t/T$	$\Delta t/T$		
	1/1000	1/100	1/10
0.25	19.5	17.5	15.8
0.5	10.8	9.8	9.8
1	7.6	9.8	8.9
2	x	x	87.9

Table 5.4: Number of iterations for model problem with constraint; $\xi = 2$ and $\beta = 0.5$.

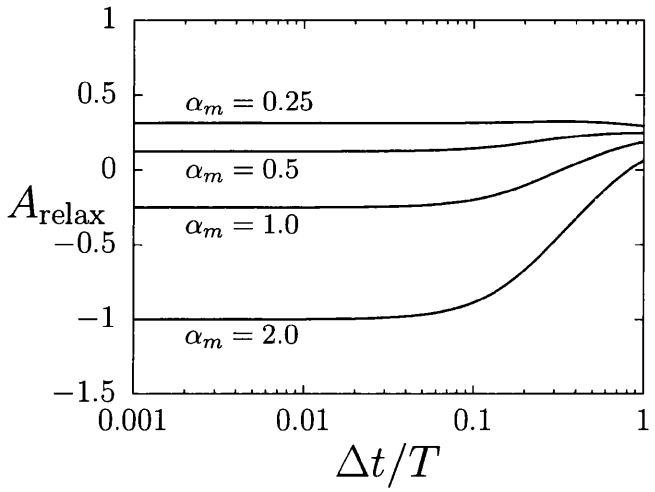

Figure 5.10: The coefficient A_{relax} for $\xi = 2$ and $\beta = 0.5$.

5.6 Convergence in the presence of non-linearities

In this section, the unconstrained model problem as introduced in Section 5.2 is considered, but the linear elastic springs are replaced by nonlinear springs, such that the force set up in one of the springs is calculated as

$$F_{\text{spring}}(\Delta u) \;=\; k\,l\,\ln\left(\frac{l+\Delta u}{l}\right)\,, \tag{5.65}$$

whereby l denotes the length of the undeformed spring and Δu is the difference between the length of the deformed and the undeformed spring. The governing Equations (5.4) – (5.7) are changed accordingly and, based on an appropriate time integration scheme, the system can be discretised and solved by means of a block Gauß-Seidel strategy along the lines of Section 5.3.1.

5.6.1 Adaptive relaxation

For the linear problem, it was possible to calculate the optimal relaxation factor β_{opt} independently of the solution variables, which renders the converged solution after one iteration step. For nonlinear problems (or for problems with multiple interface degrees of freedom) no such relaxation factor exists. However, given an initial relaxation parameter β_0 for the first iteration, the value of β may be adaptively improved for each step of the iteration by means of the so-called "Aitken acceleration" method. This strategy is based on linear interpolation between two successive trial solution values and was originally proposed in [51] and described by *e.g.* [52].

The Aitken relaxation method aims to get an improved guess for the next iteration, based on the outcome of the two previous iterations. Here, x and x^* denote respectively the value at the start of an iteration and the value at the end of that iteration, and $f(x)$ is a function of x. Figure 5.11 shows the relation between the improved guess and the two previous ones. In the figure, a and b indicate the starting values for respectively the first and second iteration, and a^* and b^* are the corresponding values at the end of the first and second iteration. For the third iteration, the starting value c is found by linearly interpolating between (a, a^*) and (b, b^*), and then looking for the value for which $y = x$, or $c^* = c$. From the figure it can be seen that c^*, and thus c, can be derived as follows:

$$c = a^* + (b^* - a^*)\frac{c - a}{b - a} \tag{5.66}$$

This can be rewritten as:

$$c = \frac{ab^* - a^*b}{a - a^* - b + b^*} \tag{5.67}$$

This equation is now split in two, by introducing a relaxation parameter. There are different ways to define the relaxation parameter. In [51], (5.67) is split as follows:

$$c = (1 - \beta_b)b^* + \beta_b b \qquad \text{with} \quad \beta_b = \frac{b^* - a^*}{a - a^* - b + b^*} \tag{5.68}$$

As this is inconvenient to compute due to the difference $b^* - a^*$, the next iteration will be considered:

$$d = (1 - \beta_c)c^* + \beta_c c \qquad \text{with} \quad \beta_c = \frac{c^* - b^*}{b - b^* - c + c^*} \tag{5.69}$$

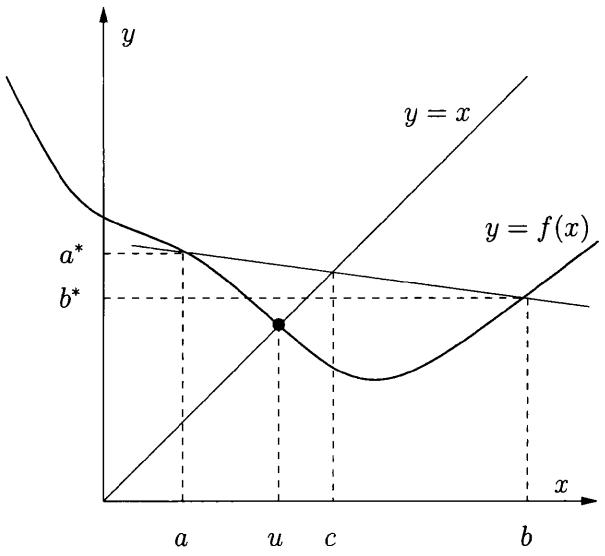

Figure 5.11: The relation between the improved guess c and the two previous ones a and b, where u is the solution.

Now the following relation can be derived for updating the relaxation parameter:

$$\beta_c = \beta_b + (\beta_b - 1)\frac{c - c^*}{b - b^* - c + c^*} \tag{5.70}$$

In a vector iteration process the computation of (5.70) will be impossible, due to division by a vector. Therefore, [51] suggests to multiply by the vector inverse $(\mathbf{b} - \mathbf{b}^* - \mathbf{c} + \mathbf{c}^*)/|\mathbf{b} - \mathbf{b}^* - \mathbf{c} + \mathbf{c}^*|^2$, which leads to:

$$\beta_c = \beta_b + (\beta_b - 1)\frac{(\mathbf{c} - \mathbf{c}^*)(\mathbf{b} - \mathbf{b}^* - \mathbf{c} + \mathbf{c}^*)}{|\mathbf{b} - \mathbf{b}^* - \mathbf{c} + \mathbf{c}^*|^2} \tag{5.71}$$

The resulting modified algorithm is as follows

- guess the displacement $u^P_{2,n+1}$
- set $u^Q_{2,n+1} = u^P_{2,n+1}$ and solve system Q [Eqs.(5.19),(5.20)] for $u^Q_{1,n+1}$ and $F^Q_{n+\gamma}$
- set $F^P_{n+\gamma} = -F^Q_{n+\gamma}$ and solve system P [Eqs.(5.17),(5.18)] for $u^P_{1,n+1}$ and $u^P_{2,n+1}$

- update the relaxation factor $\beta \leftarrow \beta + (\beta - 1) \frac{u^P_{2,n+1} - u^Q_{2,n+1}}{\Delta U - (u^P_{2,n+1} - u^Q_{2,n+1})}$
- update $\Delta U = u^P_{2,n+1} - u^Q_{2,n+1}$
- update the solution variable $u^P_{2,n+1} \leftarrow (1 - \beta)\, u^P_{2,n+1} + \beta\, u^Q_{2,n+1}$
- if the desired accuracy is not met, *i. e.* $|u^P_{2,n+1} - u^Q_{2,n+1}| > tol$, go to step 2
- perform time updates [Eqs.(5.15),(5.16)] and proceed with next time step

For the first iteration step, the last value of β of the previous time step may be used and ΔU should be set to zero. The quantity ΔU is the only additional data required by the Aitken acceleration method. It is noted that in higher dimensions, it is common practice to employ the Euclidean norm of the difference vectors in the formula for β.

The same problem parameters as in the previous examples are chosen in order to solve the model problem numerically. Additionally, the lenght of the springs $l = 1.2$ is set. The trapezoidal rule is used for the discretisation in time. The stiffnesses of the nonlinear springs in the undeformed configuration are identical to those in the linear problem. Therefore, the eigenfrequencies in the undeformed configuration coincide, and the values of T calculated for the linear problem are used. Again, the simulations are performed for a range of different values of α_m and different ratios $\Delta t/T$. The numbers of iterations required to achieve the accuracy as defined by (5.39) with different types of relaxation are given in Table 5.5. The numbers of iteration steps required for $\beta = 0$, $\beta = 0.5$ and $\beta = \beta^*_{\text{opt}}$ follow the trends illustrated and explained in the previous sections and examples of this work. The table also clearly shows the benefit of the adaptive relaxation based on the Aitken acceleration. In all cases considered, the Aitken method requires fewer iteration steps than any other relaxation strategy.

5.7 Conclusion

Based on a discrete model problem composed of springs, dashpots and point masses, the Gauß-Seidel solution strategy for a coupled problem has been analysed. The following observations have been made:

α_m	no relaxation, $\beta = 0$			relaxation, $\beta = 0.5$			relaxation, $\beta = \beta^*_{\text{opt}}$			adaptive relaxation		
	$\Delta t/T$			$\Delta t/T$			$\Delta t/T$			$\Delta t/T$		
	1/1000	1/100	1/10	1/1000	1/100	1/10	1/1000	1/100	1/10	1/1000	1/100	1/10
0.25	16.4	14.7	13.5	23.3	21.0	18.3	1.0	1.9	3.5	1.0	1.0	2.3
0.5	33.0	29.7	27.9	16.3	14.6	12.8	1.1	1.9	4.1	1.0	1.2	2.6
1	x	x	689.2	1.1	2.1	4.4	1.1	2.1	4.4	1.0	1.3	2.7
2	x	x	x	33.4	30.0	21.7	1.3	2.3	5.8	1.0	1.4	2.9

Table 5.5: Numbers of iteration steps for the model problem with nonlinear springs.

- The factor A as defined by Eq. (5.24) is decisive for the success and convergence behaviour of the methodology. For the problem under consideration, it has been shown that

$$\lim_{\Delta t \to 0} A = -\alpha_m \qquad \text{and} \qquad \lim_{\Delta t \to \infty} A = -\alpha_k \,,$$

  where α_m and α_k are the mass and the stiffness ratios of the coupled systems, respectively. Typical values for fluid-structure interaction problems are $\alpha_m < 1$ and $\alpha_k = 0$. The variation of the factor A between these limits explains why the convergence behaviour often deteriorates as Δt is decreased. It is noted that, the more accurate the time integration scheme, the more dominant is the limit $\lim_{\Delta t \to 0} A$. Increased numerical instability resulting from more accurate time integration has also been proven in the context of staggered schemes [49].

- For all values $A \neq 1$ of the linear problem considered, there exists a range of relaxation parameters β including an optimal value β_{opt}, such that convergence can be achieved by employing relaxation.

- The inclusion of an incompressibility type constraint to one of the subsystems invariably jeopardises the convergence behaviour. The incompressibility of the fluid increases the "added mass". Consequently, the mass ratio increases and convergence deteriorates.

- The beneficial effect of adaptive relaxation based on the Aitken acceleration has been demonstrated for the model problem.

Finally, it is pointed out that the model problem considered is computationally "simple" due to the single degree of freedom interface. Long interfaces of real applications may exhibit several length and time scales, which gives rise to additional difficulties even for linear problems.

Chapter 6

Numerical examples

Three numerical examples are considered in order to investigate the relevance of the findings of the previous chapters for 2D fluid-structure interaction problems and to compare the different Newton procedures. The first numerical example is that of flow induced oscillations of a flexible beam, as introduced by Wall [24] and considered by others (see *e. g.* [4, 12, 32]). The second example describes the flow through a channel with a flexible wall, as published by *e. g.* Pedley *et. al.* [53], Heil [54] and Dettmer & Perić [7]. The last example that is considered describes a flow through a flexible tube, see *e. g.* [4].

The finite element meshes, interface discretisations and material properties are the same as in the given references.

6.1 Numerical example 1: Flow induced oscillations of a flexible beam

6.1.1 Introduction

The example of the flow induced oscillating beam was introduced by Wall [24] in order to investigate the coupling between complex fluid flow and large structural deformations, and has since been commonly used as a benchmark problem (see *e. g.* [4, 12, 32]). A flexible beam attached to a square rigid body is placed in a uniform incompressible flow field. For Reynolds numbers

higher than approximately Re = 100 vortices will separate from the rigid square and generate lift forces that cause oscillation of the flexible beam. The geometry of the problem and the boundary conditions are shown in Figure 6.1. The problem parameters are chosen exactly as in [4, 24], which for the fluid gives a fluid density of $\rho^f = 1.18 \cdot 10^{-3}$, a fluid viscosity of $\mu^f = 1.82 \cdot 10^{-4}$ and an inflow velocity of $u_\infty = 51.3$. For the structure a shear modulus of $\mu^s = 9.2593 \cdot 10^5$, a bulk modulus of $K^s = 2.78 \cdot 10^6$ and a density of $\rho^s = 0.1$ is chosen. The given shear modulus and bulk modulus correspond to a Young's modulus of $2.5 \cdot 10^6$ and a Poisson's ratio of 0.35. The Reynold's number is computed as

$$\mathrm{Re} = \frac{\rho^f D\, u_\infty}{\mu^f} \tag{6.1}$$

where $D = 1$ is the diameter of the square rigid body. This results in a Reynold's number of Re = 333 for the given dimensions and material properties.

The fluid mesh consists of 4336 linear triangular equal-order SUPG/PSPG stabilised elements, whereas the elastic beam is discretised with 20 nine-noded fully integrated continuum elements as shown in Figures 6.2 and 6.3. Plane stress conditions are applied to the beam and small strain elastic behaviour is assumed. All solid nodes at the interface are used as interface nodes. The kinematical data of the fluid at the interface is computed by linear interpolation between the fluid nodes that correspond to solid nodes at the interface. The fluid and the solid dynamics are integrated with the generalised-α method for first and for second order systems, respectively. Thus, ρ^s_∞ and ρ^f_∞ can be chosen independently. At the interface, the fluid and solid nodal displacements and velocities associated with the time instants $t_n, t_{n+1}, \ldots$ match exactly, whereas the accelerations are allowed to evolve independently.

The coupled problem is solved using various methods described in Chapter 2. Later in this chapter the methods will be compared and assessed based on their overall performance. The following methods are considered

- Monolithic strategy (MN), as described in Section 2.4.3
- Partitioned Block Newton strategy with elimination of the solid domain (PN), as described in Section 2.4.3
- Gauß-Seidel strategy without relaxation (GS), as described in Section 5.3.1

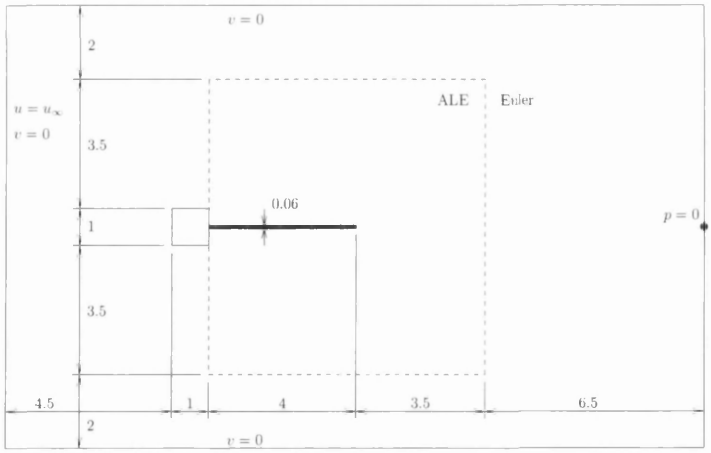

Figure 6.1: Schematic view of the geometry and boundary conditions of the flow induced oscillating beam.

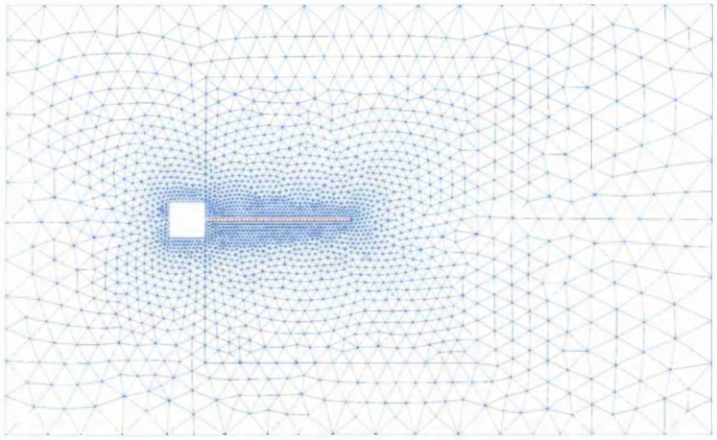

Figure 6.2: Finite element mesh for the flow induced oscillation beam.

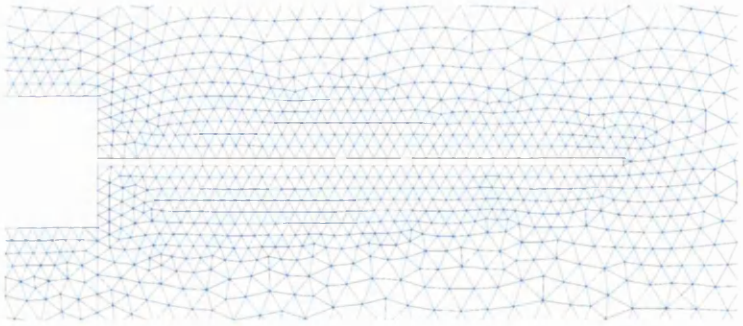

Figure 6.3: A detail of the finite element mesh.

- Gauß-Seidel strategy with fixed relaxation (GS-FR), as described in Section 5.4
- Gauß-Seidel strategy with adaptive relaxation (GS-AR), as described in Section 5.6.1

For equal time step sizes and tolerances all methods give the same result. To show this is the case the vertical displacement of the tip of the beam d is plotted in Figure 6.4 for time integration parameters $\rho_\infty^s = 0.5$ and $\rho_\infty^f = 0.5$, time step size $\Delta t = 0.01$ and interface tolerance tol $= 10^{-7}$. The inflow velocity u_∞ is applied instantaneously at time $t = 0$. To confirm that the solutions that are found with the different strategies are equal, the vertical displacement of the tip of the beam d is plotted for a smaller number of time steps in Figure 6.5. The points A, B, C and D refer to respectively Figures 6.6(a), 6.6(b), 6.6(c) and 6.6(d), where the vorticity of the fluid flow is plotted for the corresponding time instants. The vorticity ranges from -150 (blue) to 150 (red).

From Figure 6.4 it can be observed that the averaged frequency $\bar{f} \approx 3.33$ and that the amplitude $A \approx 1.2$, which corresponds to the findings in [4,12,24]. For the used time step size Δt, the ratio $\Delta t/T$ is approximately $1/30$.

6.1.2 Interpolation of the traction forces at the interface

With this numerical example the influence of traction force interpolation at the interface can now be investigated in the context of a 2D fluid-structure interaction problem. For the 1D model problem it was found that transferring the traction forces without any interpolation, leads to inaccurate and occasionally unstable results. The issue is related to the full set of equations that describe the problem and therefore concerns all strongly coupled strategies. Here it is chosen to perform the analysis of the oscillating beam regarding the interpolation of the forces at the interface using a monolithic solution strategy.

Figure 6.7 shows the vertical displacement of the tip of the beam d for four different combinations of ρ_∞^s and ρ_∞^f, all without any interpolation of the traction forces at the interface. The time step size is set to $\Delta t = 0.01$ and the tolerance is tol $= 10^{-7}$. The first two plots show the response of the system

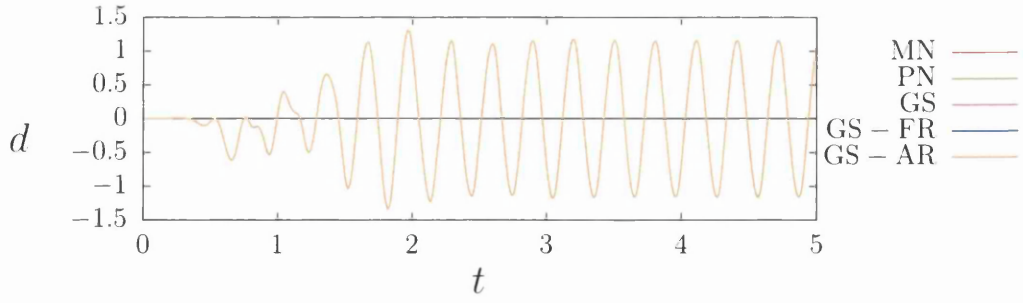

Figure 6.4: Vertical beam tip displacement for different coupling strategies.

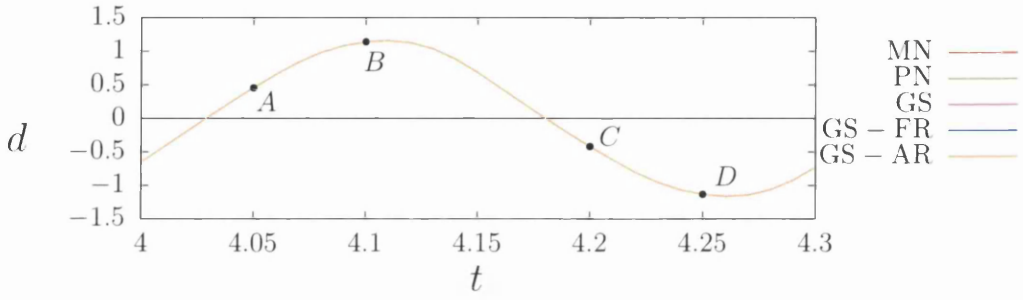

Figure 6.5: Detail of the vertical displacement of the beam tip.

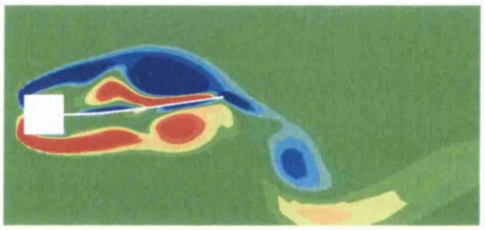

(a) $t = 4.05$ (Point A in Figure 6.5).

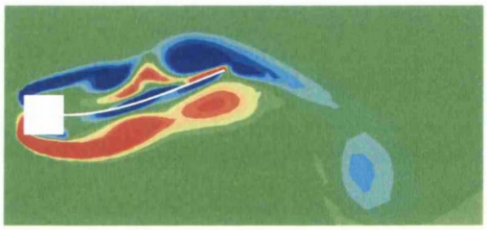

(b) $t = 4.10$ (Point B in Figure 6.5).

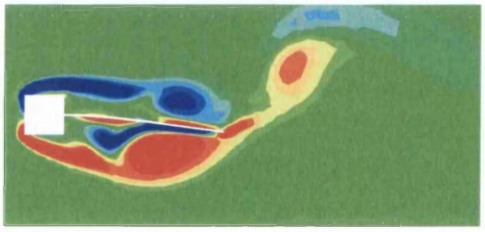

(c) $t = 4.20$ (Point C in Figure 6.5).

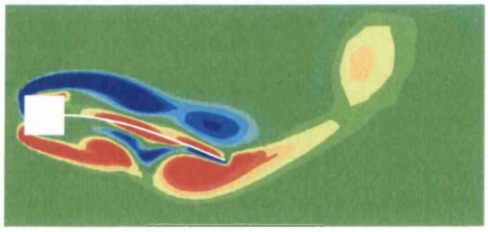

(d) $t = 4.25$ (Point D in Figure 6.5).

Figure 6.6: Vorticity distribution at time instants $t = 4.05$ ((a)), $t = 4.10$ ((b)), $t = 4.20$ ((c)) and $t = 4.25$ ((d)), ranging from -150 (blue) to 150 (red).

for equal time integration parameters ($\rho_\infty^s = \rho_\infty^f = 0.2$ and $\rho_\infty^s = \rho_\infty^f = 0.8$). Also, a reference solution is shown, to compare the different plots and assess the influence of the amount of numerical damping on the response. The reference solution is obtained with the following parameters: $\rho_\infty^s = \rho_\infty^f = 0.5$, $\Delta t = 0.005$ and tol $= 10^{-7}$. It can be seen that the influence of numerical damping is small and that the response for $\Delta t = 0.01$ is relatively accurate. The solution is also shown for unequal values of ρ_∞^s and ρ_∞^f; for $\rho_\infty^s = 0.2$ and $\rho_\infty^f = 0.8$ and for $\rho_\infty^s = 0.8$ and $\rho_\infty^f = 0.2$. For $\rho_\infty^s = 0.2$ and $\rho_\infty^f = 0.8$ the solution is stable, however, for $\rho_\infty^s = 0.8$ and $\rho_\infty^f = 0.2$ the system develops violent high frequency oscillations, which bear resemblance with the second eigenmode of the flexible beam. The energy absorbed by the solid structure is clearly increasing and leads to the failure of the simulation. This suggests the presence of the same instability as observed in Chapter 4.

In Figure 6.8 the oscillations of the beam tip are shown for calculations that take into account the proper interpolation of the traction forces at the interface. As the interpolation does not affect the results when equal time integration parameters are used, only the results obtained with different values of ρ_∞^s and ρ_∞^f are shown. Due to the different time integration parameters (combined with the rather large time step) the systems responds slightly different from the reference solution obtained for $\rho_\infty^s = \rho_\infty^f = 0.5$. However, both plots show stable results and accuracy of the solution has improved. It can therefore be concluded that the findings from Chapter 4 are applicable to 2D fluid-structure interaction problems, which means that when using different time integration schemes interpolation of the forces at the interface is needed to maintain stability and accuracy properties.

6.1.3 Gauß-Seidel procedure for coupled problems

In Chapter 5 the Gauß-Seidel solution strategy was analysed in detail. For the 1D model problem the main conclusions were that the convergence of the method depends on the mass ratio α_m and that the performance of the method can be significantly improved by applying a type of relaxation to the procedure. Whether the conclusions hold for a 2D fluid-structure interaction problem is investigated here. The oscillation of the flexible beam is solved using the Gauß-Seidel solution strategy for different types of relaxation. The number of iterations n that is needed per time step is recorded in order to make a comparison between the different relaxation types. Using the material properties from Section 6.1.1, the problem is solved with $\rho_\infty^s = \rho_\infty^f = 0.5$, $\Delta t = 0.01$ and tol $= 10^{-7}$.

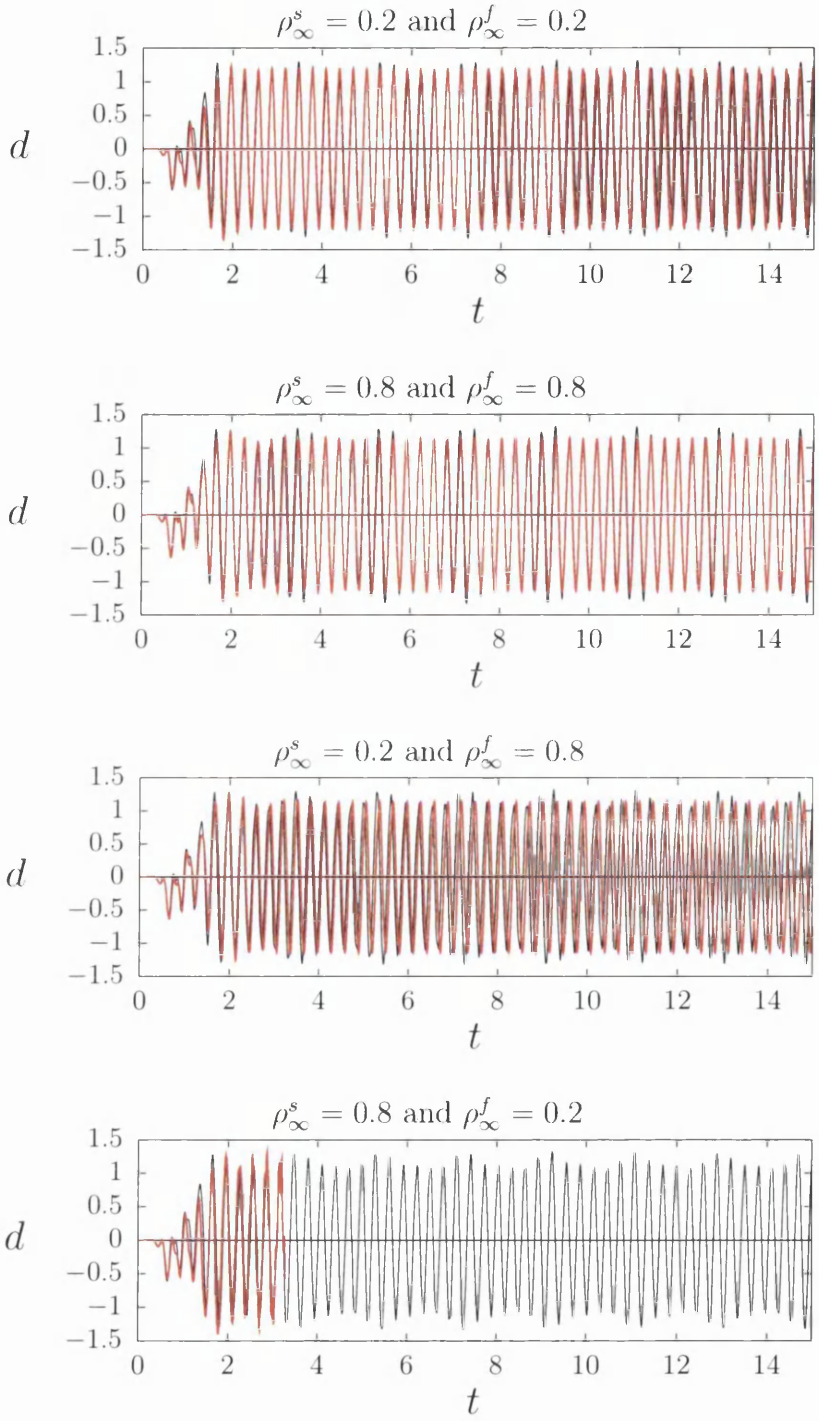

Figure 6.7: The vertical displacement of beam tip for time step size $\Delta t = 0.01$ without interpolation of the traction forces at the interface.

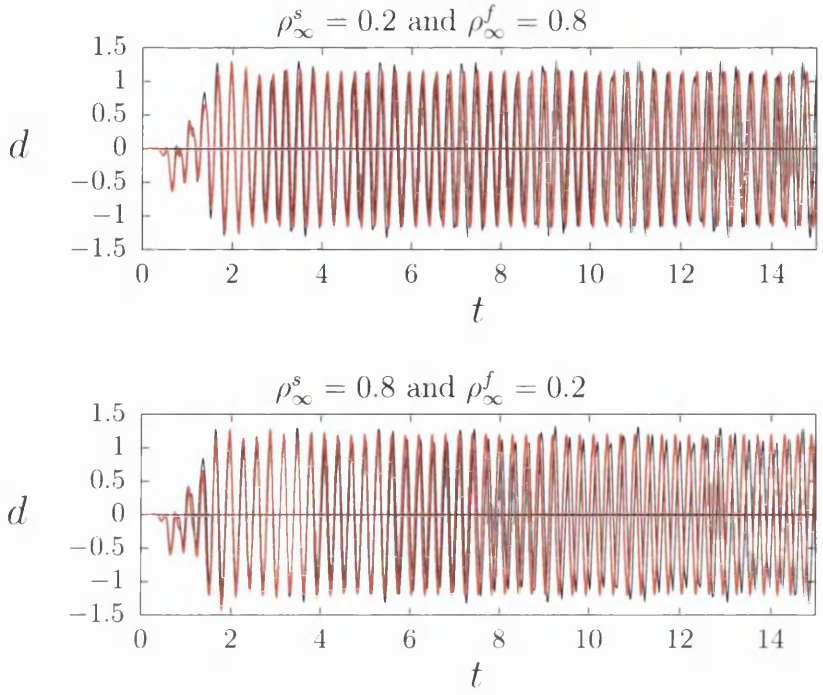

Figure 6.8: The vertical displacement of beam tip for time step size $\Delta t = 0.01$ with interpolation of the traction forces at the interface.

The number of iterations n per time step for the different types of relaxation is shown in Figure 6.9. Firstly, the number of iterations that is needed for convergence using the Gauß-Seidel solution procedure without relaxation is shown. The average number of iterations $\bar{n}$ for the range $3 < t \leq 5$ is $\bar{n} = 81.1$. It can be seen that there are large fluctuations in the number of iterations n. Results found when applying constant relaxation are shown next. It is clear the number of iterations per time step is highly dependent on the relaxation parameter β. The average number of iterations corresponding to the different relaxation parameters is as follows: $\bar{n} = 55.0$ for $\beta = 0.2$, $\bar{n} = 25.4$ for $\beta = 0.4$, $\bar{n} = 15.0$ for $\beta = 0.6$ and $\bar{n} = 24.1$ for $\beta = 0.8$. Thus, for the current material properties, when using constant relaxation, the Gauß-Seidel solution procedure performs best if $\beta \approx 0.6$. When using adaptive relaxation the starting value of β_0 appears not to be as important. The average number of iterations is found as $\bar{n} = 12.4$ for $\beta_0 = 0.2$, $\bar{n} = 11.8$ for $\beta_0 = 0.4$, $\bar{n} = 11.3$ for $\beta_0 = 0.6$ and $\bar{n} = 10.9$ for $\beta_0 = 0.8$. The fluctuations that were observed in the case for no relaxation have disappeared and the number of iterations n is more constant.

To compare the different types of relaxation, the best performing cases of

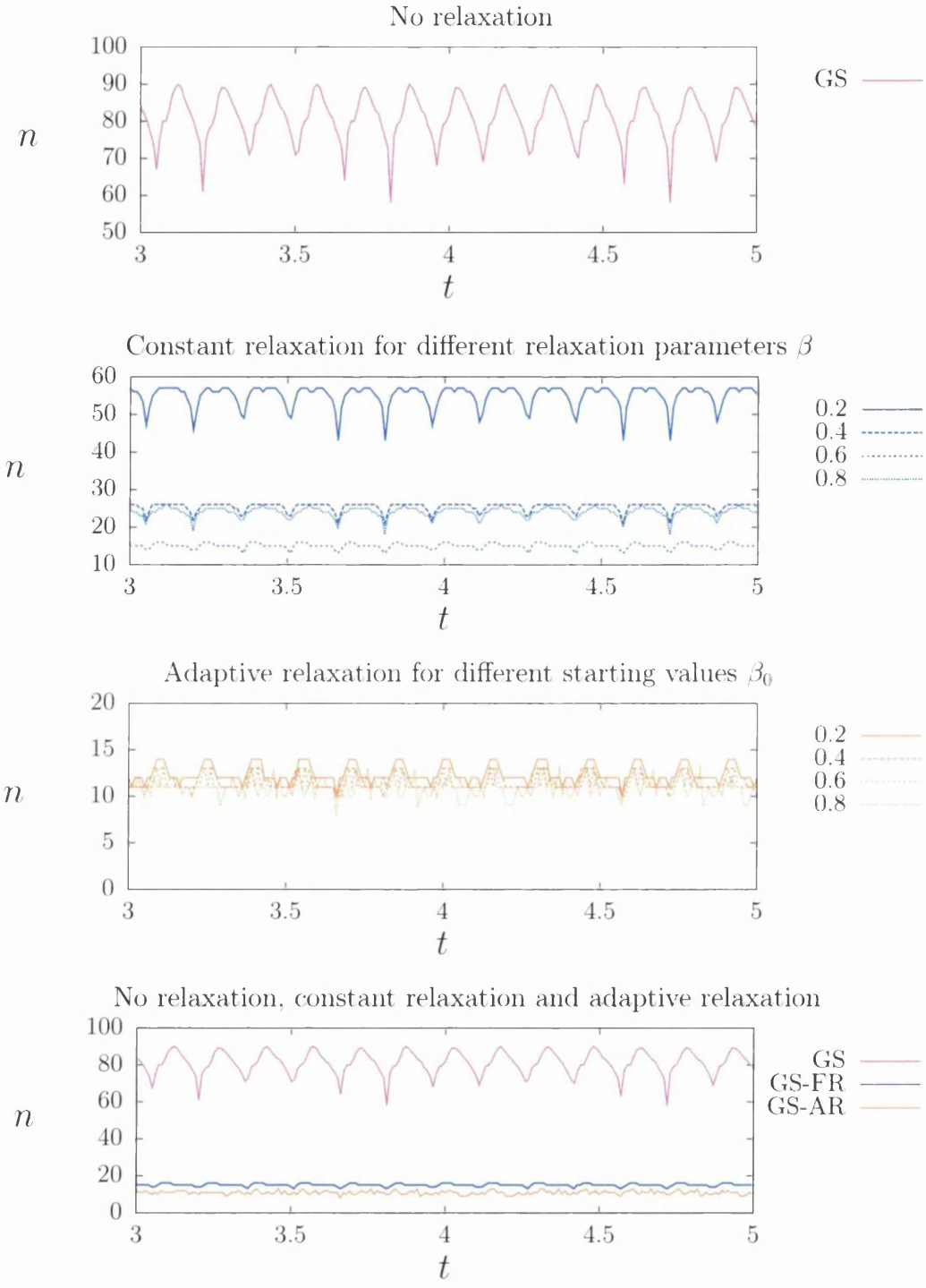

Figure 6.9: Oscillating flexible beam: The number of iterations n per time step needed for convergence using the Gauß Seidel solution procedure without relaxation, with constant relaxation, with adaptive relaxation and a comparison.

each type of relaxation are shown again. This means that for constant relaxation it is chosen to use $\beta = 0.6$ and for adaptive relaxation it is chosen to use $\beta_0 = 0.8$. It is observed that applying relaxation improves the performance of the solution strategy significantly. Adaptive relaxation leads to slightly better results than constant relaxation, but it has to be noted that constant relaxation only performs this well for this specific relaxation parameter β, whereas adaptive relaxation performs well regardless of the starting value for β_0. This confirms the findings of Chapter 5.

Whether the mass ratio between the solid and the fluid influences the convergence behaviour of the Gauß-Seidel solution strategy is analysed by calculating the response of the system for a higher density of the flexible beam. A higher density of the flexible beam will decrease the value of mass ratio α_m as defined in Section 5.2 and it is therefore expected to lead to improved convergence rates. The density of the flexible beam is set to $\rho^s = 0.2$. Figure 6.10 shows the number of iterations n for respectively the case without relaxation, with constant relaxation and with adaptive relaxation. The average number of iterations for the case without relaxation is $\bar{n} = 23.8$. For the calculations with constant relaxation the average numbers of iterations are $\bar{n} = 61.3$ for $\beta = 0.2$, $\bar{n} = 28.5$ for $\beta = 0.4$, $\bar{n} = 16.8$ for $\beta = 0.6$ and $\bar{n} = 11.9$ for $\beta = 0.8$. Finally, the numbers of iterations for the calculations with adaptive relaxation are $\bar{n} = 11.0$ for $\beta_0 = 0.2$, $\bar{n} = 10.9$ for $\beta_0 = 0.4$, $\bar{n} = 10.7$ for $\beta_0 = 0.6$ and $\bar{n} = 9.6$ for $\beta_0 = 0.8$.

It can be observed that the Gauß-Seidel solution strategy without relaxation performs significantly better for the case with the decreased mass ratio α_m. The performance of the solution strategy with constant or adaptive relaxation improves slightly and is still better than the case without relaxation.

6.1.4 Comparison of different solution strategies

In this section the performance of the different solution strategies is assessed and compared with each other. The problem with the flow induced oscillating beam is solved with the material properties described in Section 6.1.1, time integration scheme parameters $\rho^s_\infty = \rho^s_\infty = 0.5$, time step size $\Delta t = 0.01$ and tolerance tol $= 10^{-7}$.

For all the solution strategies that are considered, the number of iterations n for $3 < t \leq 5$ is shown in Figure 6.11(a). The average number of iterations $\bar{n}$ for each strategy is given in Table 6.1. In the figure, the number of iterations

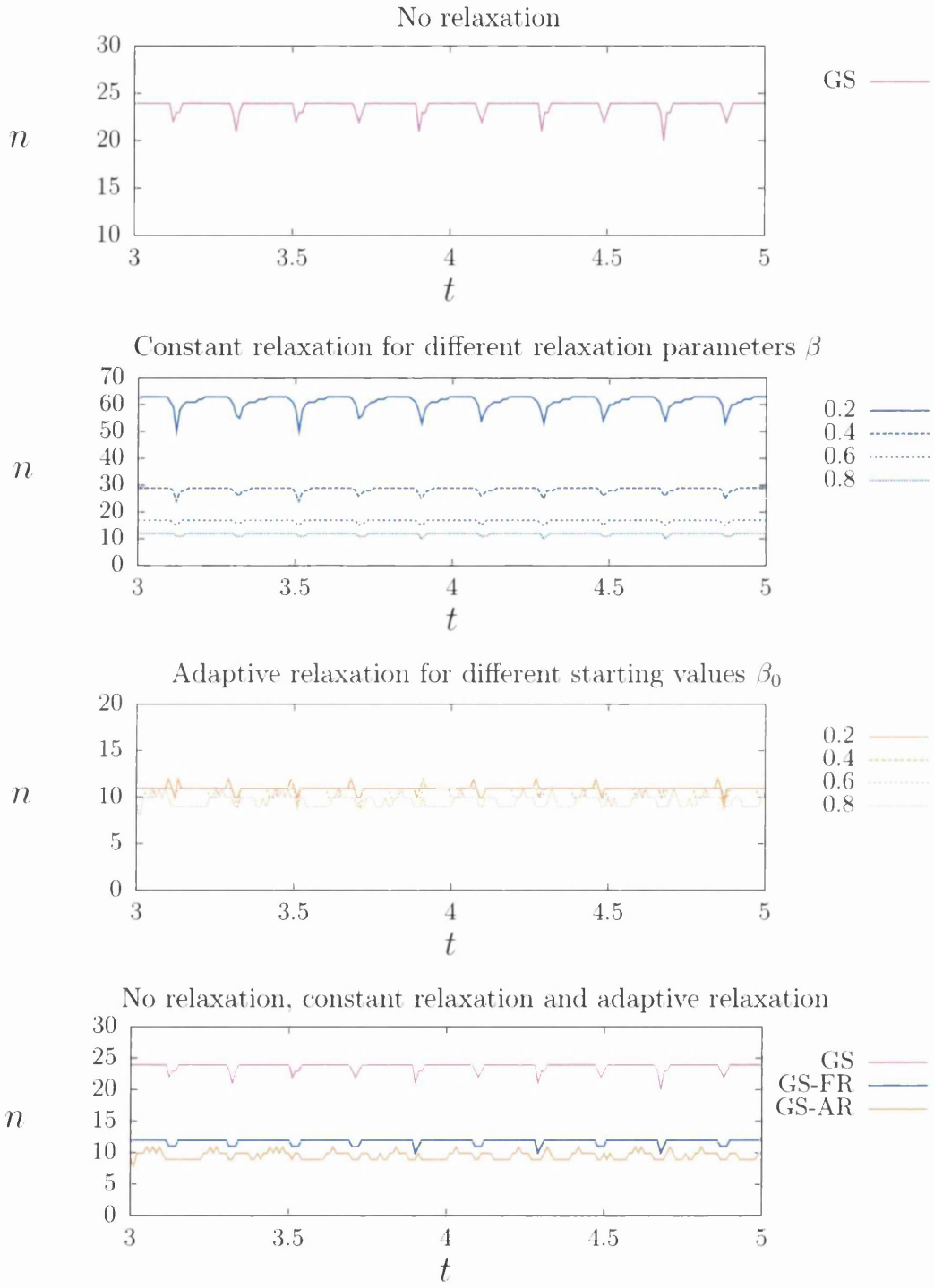

Figure 6.10: Oscillating flexible beam: The number of iterations n per time step needed for convergence using the Gauß Seidel solution procedure for the problem with a higher solid density $\rho^s = 0.2$.

for the monolithic solution strategy (MN) is not visible. This is caused by the fact that for the partitioned Newton procedure PN the number of iterations is exactly the same. Furthermore, it can be observed that the performance of the Gauß-Seidel strategy without relaxation is very poor compared to all the other strategies. The strategies that performs best in terms of number of iterations per time step are the partitioned Newton procedure and the monolithic strategy.

However, it is known that one Gauß-Seidel iteration costs less computational time than one block Newton iteration. The computational time t^* per time step is therefore displayed in Figure 6.11(b). Also, the average computational time $\bar{t}^*$ (again computed over the range $3 < t \leq 5$) is given in Table 6.1. The performance of the Gauß-Seidel strategy without relaxation is still much worse than any of the other strategies. The block Newton strategy, even thought performing as good as the monolithic strategy in terms of number of iterations, is not the one performing best in terms of computational time per time step. One iteration needs so much time, that it is more efficient to use another method that requires more iterations. The strategy that resolves the problem in the least amount of time is the monolithic strategy, followed by the Gauß-Seidel strategy with adaptive relaxation.

The range of calculations is repeated for time step sizes $\Delta t = 0.02$ and $\Delta t = 0.005$, in order to analyse the influence of the time step size on the performance of the solution strategies. For time step size $\Delta t = 0.02$ the number of iterations n and the computational time t^* are shown in Figures 6.12(a) and 6.12(b) respectively. The averages $\bar{n}$ and $\bar{t}^*$ can be found in Table 6.2. Figures 6.13(a) and 6.13(b) show respectively the number of iterations n and computational time t^* for time step size $\Delta t = 0.005$ and Table 6.3 the corresponding averages $\bar{n}$ and $\bar{t}^*$. It can be seen that the influence of the time step size on the performance of the solution strategies is small. For all time step sizes the monolithic strategy is the best one when it comes to computational time per time step. Also, for all time steps the Gauß-Seidel strategy without relaxation needs the most time to obtain the solution.

In order to get more insight in the convergence behaviour of the solution strategies, in Figure 6.1.4 the residual e is plotted against the iterations i. The residuals are calculated for time step size $\Delta t = 0.005$ and the residuals shown are obtained in the 1000^{th} time step (*i. e.* time instant $t = 5$). It can be seen that for all solution strategies the convergence behaviour is smooth. The residuals for the monolithic strategy and the block Newton strategy are the same and the poor convergence rate of the Gauß-Seidel strategy is clearly visible.

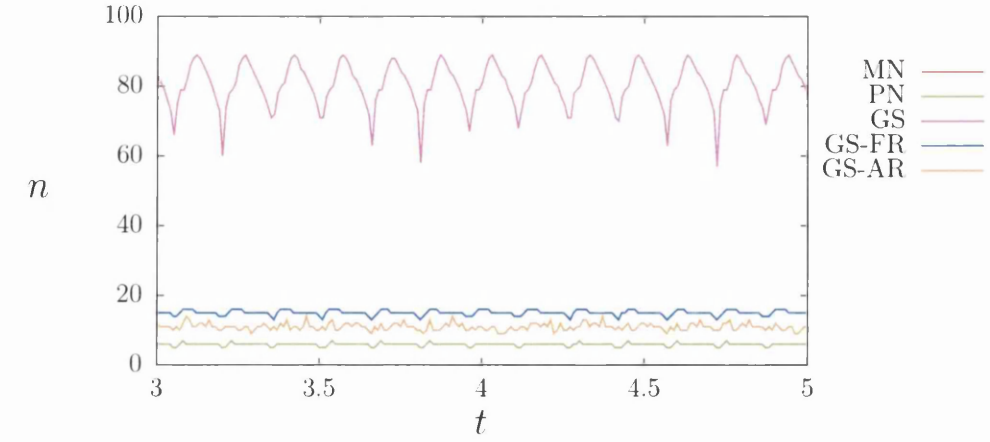

(a) Number of iterations per time step

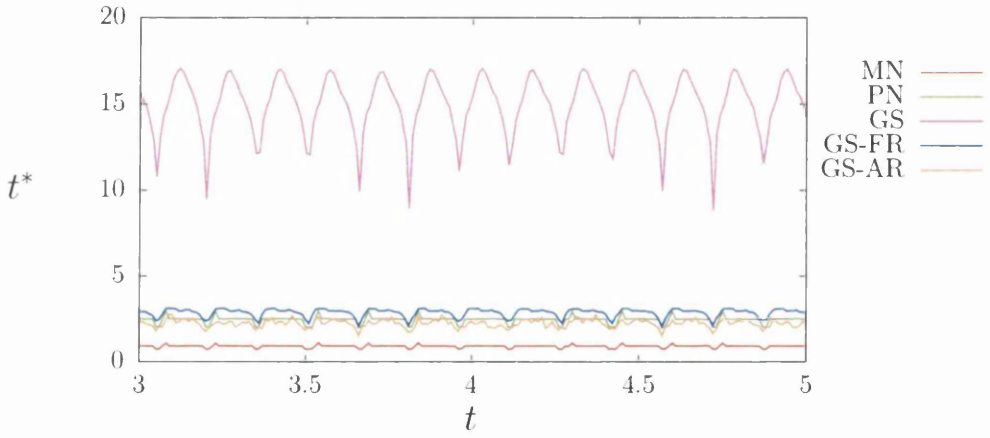

(b) Computational time per time step

Figure 6.11: Oscillating flexible beam: The number of iterations n and computational time t^* per time step needed for convergence with time step size $\Delta t = 0.01$.

	$\bar{n}$	$\bar{t}^*$
MN	5.9	0.91
PN	5.9	2.45
GS	80.4	14.92
GS-FR	15.0	2.86
GS-AR	11.0	2.24

Table 6.1: Oscillating flexible beam: The average number of iterations $\bar{n}$ and average computational time $\bar{t}^*$ for each solution strategy, using $\Delta t = 0.01$.

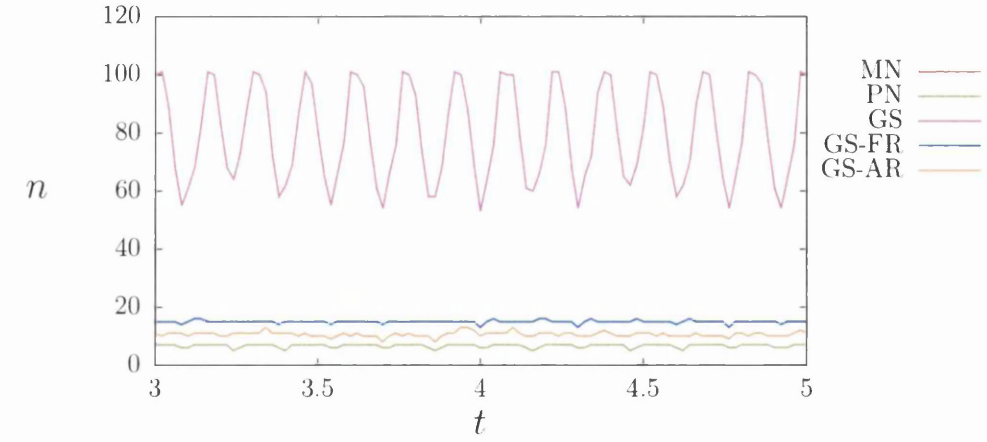

(a) Number of iterations per time step

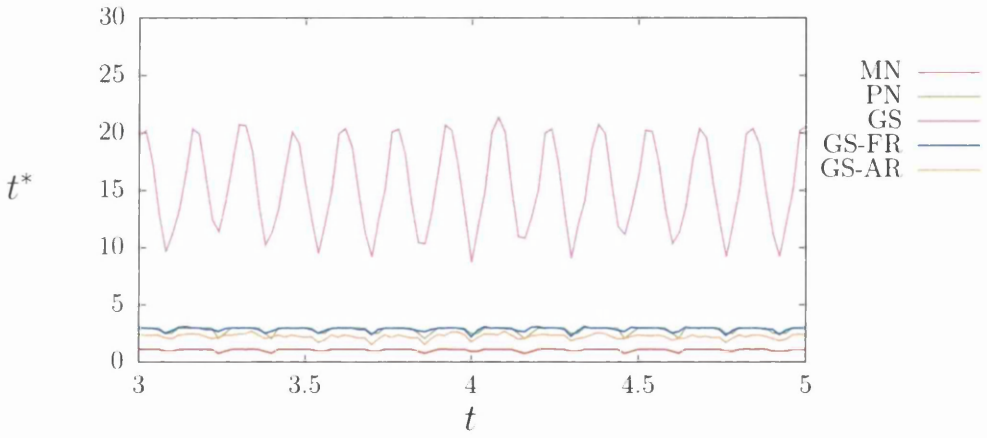

(b) Computational time per time step

Figure 6.12: Oscillating flexible beam: The number of iterations n and computational time t^* per time step needed for convergence with time step size $\Delta t = 0.02$.

	$\bar{n}$	$\bar{t}^*$
MN	6.7	1.04
PN	6.7	2.79
GS	79.7	15.42
GS-FR	15.0	2.85
GS-AR	10.6	2.22

Table 6.2: Oscillating flexible beam: The average number of iterations $\bar{n}$ and average computational time $\bar{t}^*$ for each solution strategy, using $\Delta t = 0.02$.

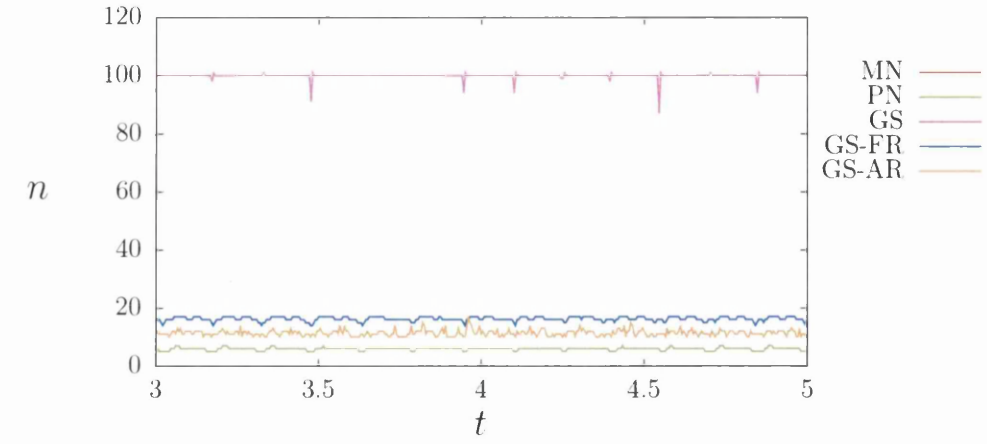

(a) Number of iterations per time step

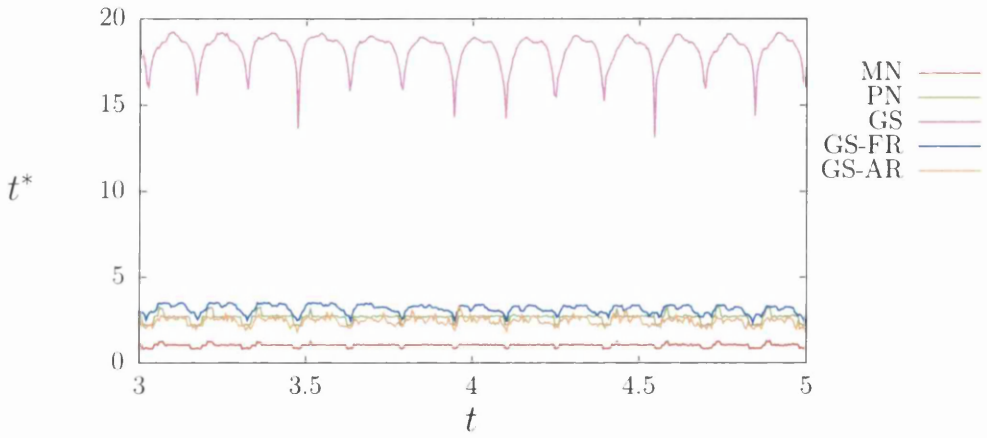

(b) Computational time per time step

Figure 6.13: Oscillating flexible beam: The number of iterations n and computational time t^* per time step needed for convergence with time step size $\Delta t = 0.005$.

	$\bar{n}$	$\bar{t}^*$
MN	5.9	1.01
PN	5.9	2.64
GS	99.9	18.20
GS-FR	16.3	3.14
GS-AR	11.4	2.42

Table 6.3: Oscillating flexible beam: The average number of iterations $\bar{n}$ and average computational time $\bar{t}^*$ for each solution strategy, using $\Delta t = 0.01$.

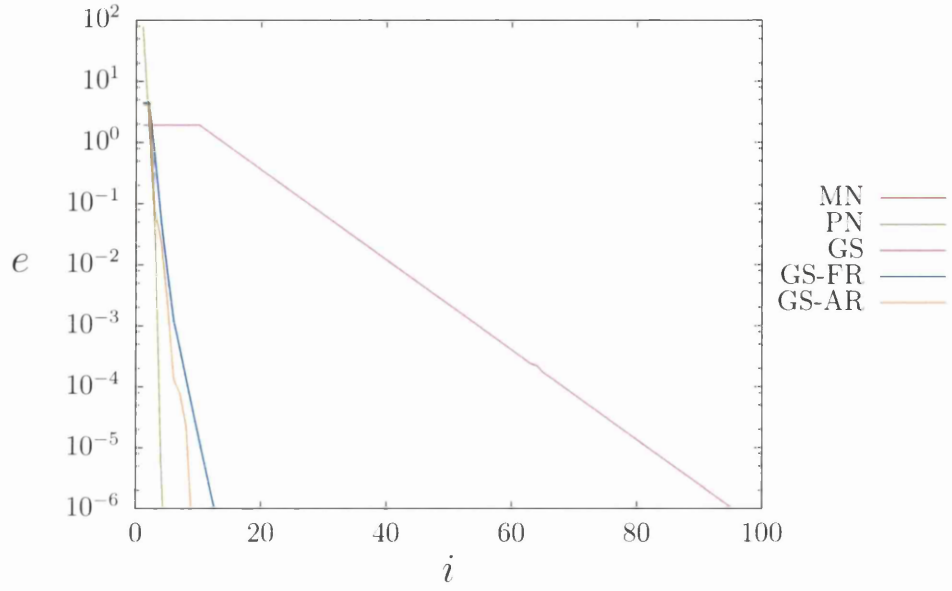

Figure 6.14: Oscillating flexible beam: The residual e as a function of the iteration number i for time step size $\Delta t = 0.005$.

The main conclusion is that the monolithic and the partitioned Newton strategies require the least amount of iterations per time step, but that the Gauß-Seidel strategies may need less computational time per time step. This is due to the elimination process and it is expected that optimising this process can reduce the computational time. This only applies to the partitioned Newton procedure, where the monolithic and Gauß-Seidel strategies already perform at their best ability.

6.1.5 Conclusion

Based on the 2D fluid-structure interaction problem of the oscillating beam in a uniform flow with a range of solution strategies, a few conclusions can be made. First of all it is confirmed that when using different time integration schemes for the different domains it is important to carefully interpolate the traction forces at the interface. It is shown that when this is not done appropriately, instabilities may occur and inaccuracies will appear.

Regarding the Gauß-Seidel solution procedure it can be concluded that the addition of relaxation significantly improves the convergence behaviour

and that the mass ratio between the fluid and the solid indeed influences the number of iteration that is needed for convergence.

The Newton procedures are the best strategies in terms of iterations per time step, however, when it comes to computational time the Gauß-Seidel strategy with adaptive relaxation can be performing better. It is thought that the current eliminating process in the solver can be improved, which would result in less computational time for the partitioned Newton strategy.

6.2 Numerical Example 2: Flow through channel with flexible wall

6.2.1 Introduction

This example describes a viscous flow through a 2D channel with a flexible wall. The fluid-structure interaction problem has been studied by Pedley *et. al.* [53], Heil [54] and Dettmer & Perić [7] among others and is characterised by a highly nonlinear fluid flow and large-displacement oscillations of the structure. These features are typical for fluid-structure interaction problems in biomedical applications, like blood flow through arteries [54]. The example concerns a channel with a partially flexible wall. The flexible part of the wall is modelled with 25 pre-stressed neo-Hooke elastic membrane elements, while the rest of the wall is fixed in space. The fluid domain consists of 8658 elements. A schematic view of the geometry and the boundary conditions of the problem is shown in Figure 6.15, together with the mesh and detailed view of the mesh. In the ALE region (see Figure 6.15(a)), the mesh is updated using the pseudo-elastic strategy. The degrees of freedom of the interface coincide with the degrees of freedom of the solid membrane.

The external pressure on the membrane elements is $p_{ext} = -0.5$. The pressure is applied linearly in 100 seconds. Then after 10 seconds the fluid flow, with a Poiseuille profile and average inflow velocity of $\bar{u}_{in} = 1.0$, is applied. This again takes 10 seconds. The time step that is used for loading the pressure is $\Delta t_p = 2.0$. The time step afterwards is variable for different simulations (and being referred to as Δt).

The fluid density and viscosity are respectively $\rho_f = 1.0$ and $\mu_f = 0.002$. The solid density $\rho_s = 0.0$ (but will be increased later on). Both domains

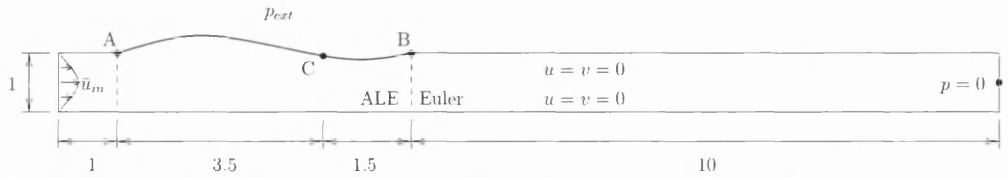

(a) Geometry and boundary conditions for the flow through a channel with flexible wall.

(b) Fluid mesh with 8658 elements and membrane mesh with 25 elements.

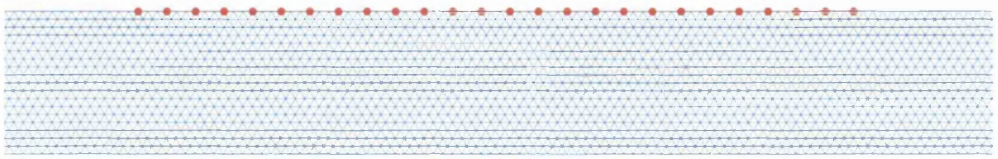

(c) Detail of the fluid and membrane mesh.

Figure 6.15: Flow through a channel with a flexible wall: Geometry, mesh and detail of the mesh.

are solved using the generalized-α method, where the time integration parameters ρ_∞^f and ρ_∞^s are both set to 0.8 for all simulations. The fluid solver tolerance and the solid solver tolerance are both set to $1.0 \cdot 10^{-8}$ and the mesh update tolerance is set to $1.0 \cdot 10^{-5}$.

The membrane is flexible and incompressible and modelled as a neo-Hookean elastic with $\mu^s = 260$. The constitutive relation between the stress and the strain is given by

$$\sigma = \mu^s \frac{\lambda^4 - 1}{\lambda^2} \tag{6.2}$$

where the principle Cauchy stress associated with the in-plane stretch λ is denoted by σ. The thickness of the membrane is 0.01 and the membrane is assumed to be in a prestressed state with $\lambda_0 = 1.2$.

The problem is solved using the monolithic strategy (MN), the partitioned Newton strategy (PN) and the Gauß-Seidel strategies (GS for no relaxation, GS-FR for constant relaxation and GS-AR for Adaptive relaxation). For the monolithic strategy, the vertical displacement of point C as shown in Figure 6.15(a) for different time step sizes is shown in Figure 6.16(a) with a detail for time step size $\Delta t = 0.1$ in Figure 6.16(b). Vorticity plots for the entire geometry are shown in Figures 6.17(a) to 6.17(d). As it can be seen in Figure 6.15(a) that the solutions for time step sizes $\Delta t = 0.1$ and $\Delta t = 0.05$

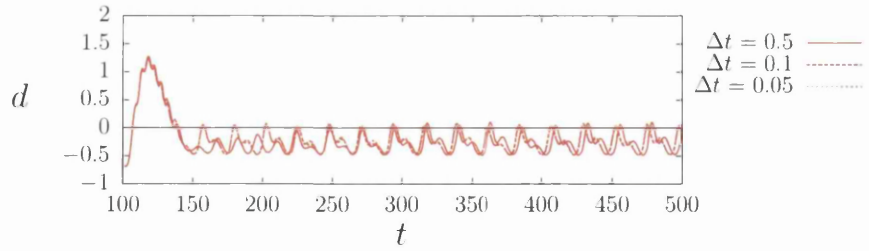

(a) Vertical displacement of point C (see Figure 6.15(a)) on the membrane.

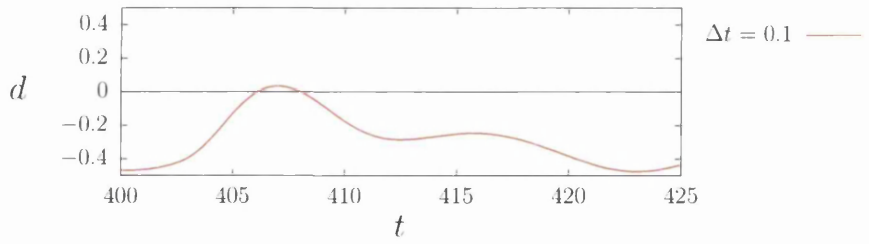

(b) Detail of the vertical displacement of point C (see Figure 6.15(a)) on the membrane.

Figure 6.16: Flow through a channel with a flexible wall: Displacement of the membrane.

(a) $t = 400.4$

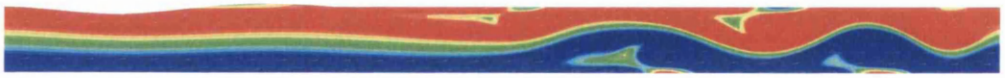

(b) $t = 407$

(c) $t = 412.5$

(d) $t = 415.8$

Figure 6.17: Vorticity distribution at time instants $t = 400.4$ ((a)), $t = 407$ ((b)), $t = 412.5$ ((c)) and $t = 415.8$ ((d)), ranging from -150 (blue) to 150 (red).

are relatively similar, the simulations in the rest of this section will be carried out with time step size $\Delta t = 0.1$.

6.2.2 Simulations

$\rho^s = 0$

The problem, as described in the previous section, is solved using the different solution strategies. The number of iterations n that was needed for convergence is shown in Figure 6.18(a). It can be seen immediately that only the results for the monolithic strategy and the partitioned Newton strategy are plotted. This is because the other methods failed to converge at one point during the simulation. In some cases stability problems occured straight at the beginning, where for other solution strategies problems occured after applying the fluid flow. The two solution strategies that succesfully solved the problem, required roughly the same amount of iterations per time step. However, looking at Figure 6.18(b), where the amount of time t^* per time step is shown, it can be observed that the monolithic strategy is more efficient. The average number of iterations $\bar{n}$ and average time $\bar{t^*}$ per time step are given in Table 6.4.

It is thought that the reason for the failure of the other methods is due to the lack of mass of the solid domain. The membrane elements are modelled with a density of $\rho^s = 0$. In Chapter 5 the limitations of the Gauß-Seidel strategy were related to the ratio between the solid mass and fluid mass. For the partitioned Newton strategy it is important to note that the interface degrees of freedom coincide with all the solid degrees of freedom, which means there are no internal degrees of freedom for the solid. To analyse the influence of the solid mass on the performance of the solution strategies, the same problem is solved for solid densities of $\rho^s = 50$ and $\rho^s = 500$.

$\rho^s = 50$

In Figures 6.19(a) and 6.19(b) respectively, the number of iterations n and computational time t^* per time step are shown for the case with solid density $\rho^s = 50$. The average number of iterations $\bar{n}$ and average time $\bar{t^*}$ per time step can be found in Table 6.4. It is immediately observed that the performance has not improved. Still only two of the solution strategies manage to succesfully obtain a solution for the problem. The two strategies, MN and PN, require roughly the same amount of iterations per time step and the monolithic strategy needs less time.

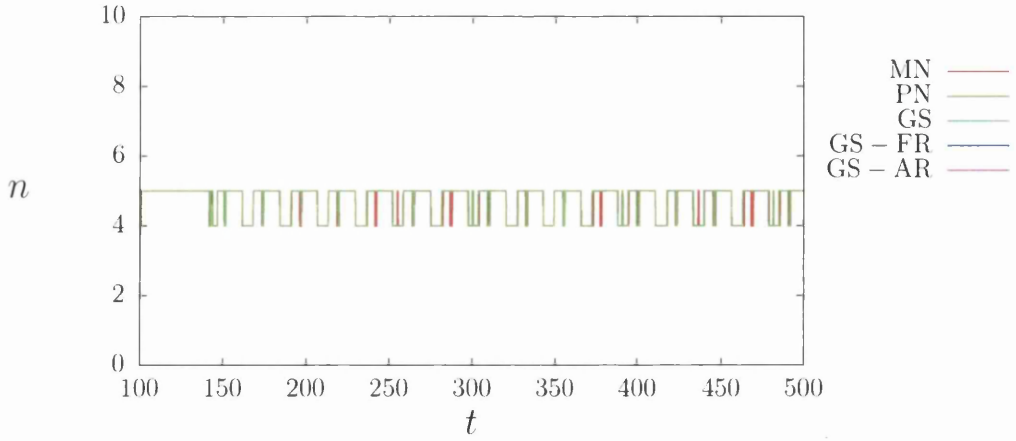

(a) Number of iterations per time step

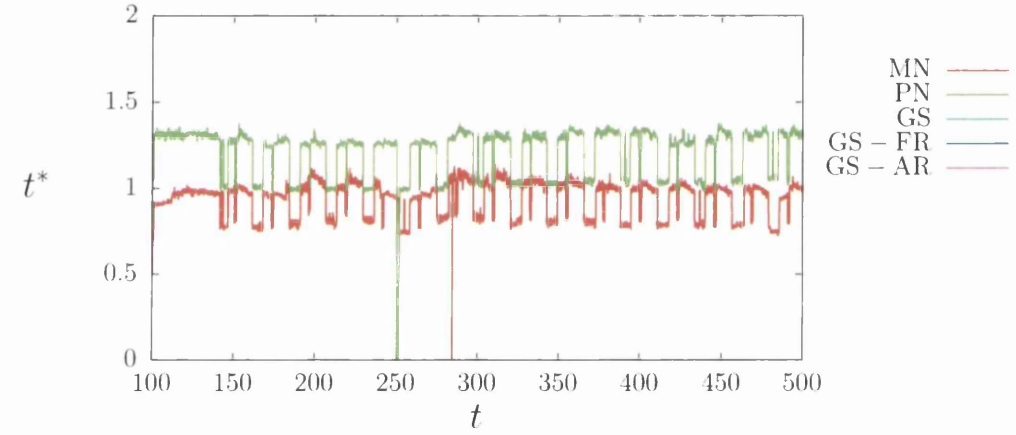

(b) Computational time per time step

Figure 6.18: Flow through a channel with a flexible wall: The number of iterations n and computational time t^* per time step needed for convergence with time step size $\Delta t = 0.01$.

	$\bar{n}$	$\bar{t^*}$
MN	4.7	0.92
PN	4.7	1.23
GS	x	x
GS-FR	x	x
GS-AR	x	x

Table 6.4: Flow through a channel with a flexible wall: The average number of iterations $\bar{n}$ and average computational time $\bar{t^*}$ for each solution strategy, using $\Delta t = 0.01$.

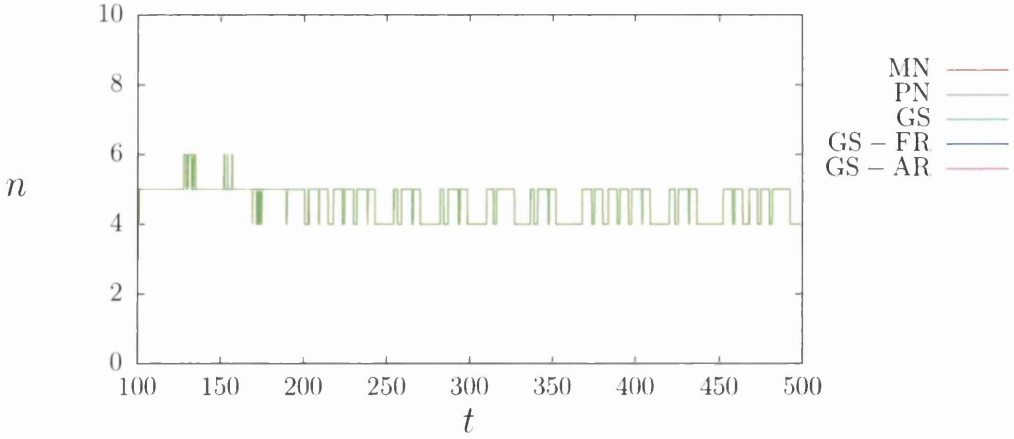

(a) Number of iterations per time step

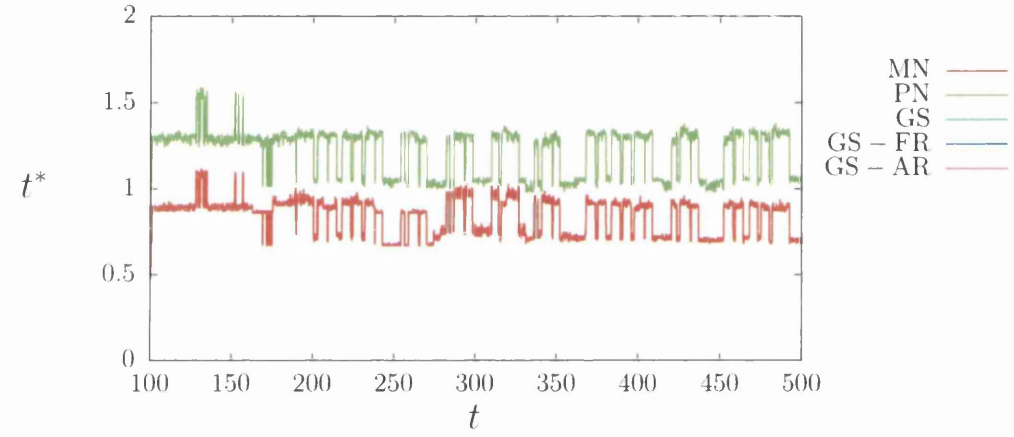

(b) Computational time per time step

Figure 6.19: Flow through a channel with a flexible wall: The number of iterations n and computational time t^* per time step needed for convergence with time step size $\Delta t = 0.01$.

	$\bar{n}$	$\bar{t}^*$
MN	4.6	0.82
PN	4.6	1.19
GS	x	x
GS-FR	x	x
GS-AR	x	x

Table 6.5: Flow through a channel with a flexible wall: The average number of iterations $\bar{n}$ and average computational time $\bar{t}^*$ for each solution strategy, using $\Delta t = 0.01$.

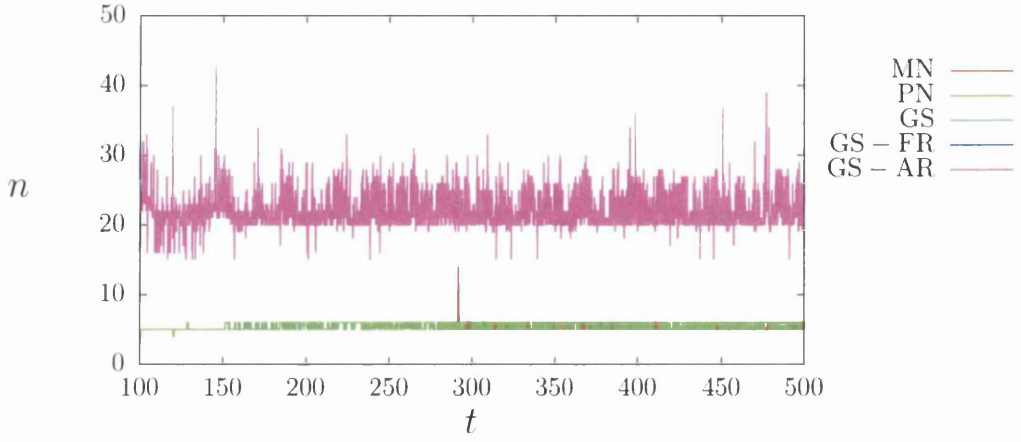

(a) Number of iterations per time step

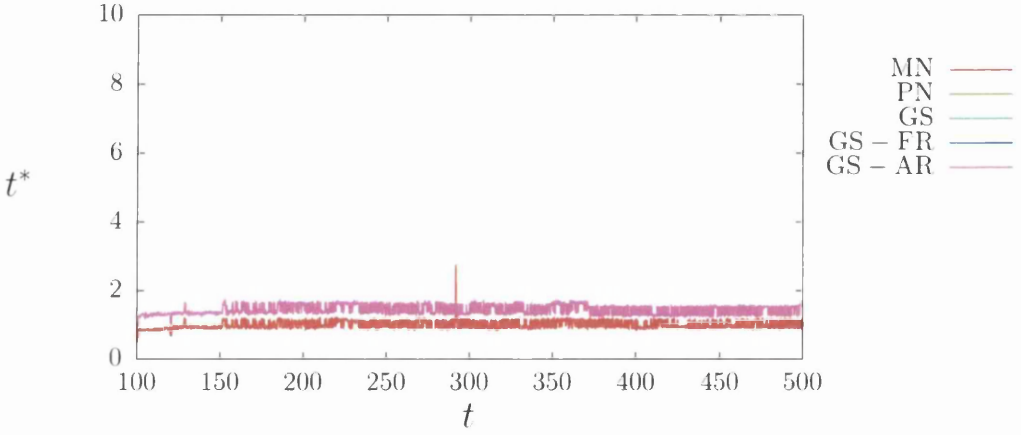

(b) Computational time per time step

Figure 6.20: Flow through a channel with a flexible wall: The number of iterations n and computational time t^* per time step needed for convergence with time step size $\Delta t = 0.01$.

	$\bar{n}$	$\bar{t^*}$
MN	5.3	1.00
PN	5.5	1.41
GS	x	x
GS-FR	x	x
GS-AR	21.94	5.49

Table 6.6: Flow through a channel with a flexible wall: The average number of iterations $\bar{n}$ and average computational time $\bar{t^*}$ for each solution strategy, using $\Delta t = 0.01$.

$\rho^s = 500$

For a solid density of $\rho^s = 500$, the number of iterations n and computational time t^* per time step are shown in respectively Figures 6.20(a) and 6.20(b). It can be seen that for this case the Gauß-Seidel strategy with Aitken relaxation succesfully obtains a solution as well. The Gauß-Seidel strategies with no or constant relaxation still fail to converge. The monolithic strategy and block Newton strategy require significantly less iterations per time step than the Gauß-Seidel strategy with adaptive relaxation. Also, the Gauß-Seidel strategy needs more computational time than the other methods. The monolithic strategy still is the most efficient one.

6.2.3 Conclusion

The numerical example of the flow through a channel with a flexible wall is solved with the different solution strategies. Only the monolithic strategy and partitioned Newton strategy lead to a converged solution. It is shown that for very high values for the solid density ρ^s, solutions can be obtained by using the Gauß-Seidel strategy with Aitken relaxation. For all cases the monolithic strategy gives the best performance.

6.3 Numerical Example 3: Flow through a flexible tube

6.3.1 Introduction

This example describes a flow through a flexible pipe. This type of problems is relevant in the field of biomechanics. It is analysed how well the different solution strategies perform for this class of problems, where there is a relatively large interface between the fluid and the solid domain.

The pipe is modelled with a neo-Hookean elastic material, see [4]. At the inflow, the nodes at the inside of the pipe are fixed in space and the outflow is free to move. The geometry and boundary conditions for this problem are shown in Figure 6.21(a). The problem is assumed to be axisymmetric. The fluid viscosity and density are respectively given as $\mu^f = 0.0101$ and

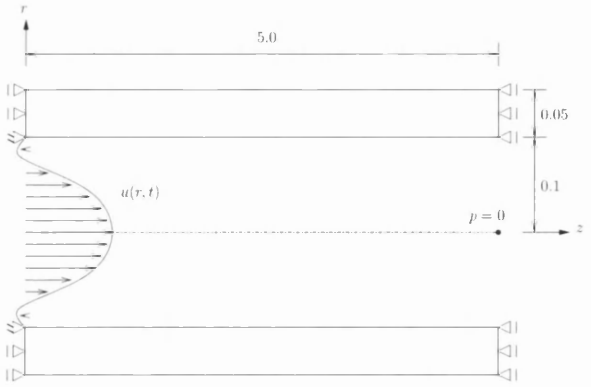

(a) Geometry and boundary conditions for the flow through a flexible pipe.

(b) Fluid mesh with 3250 elements and solid mesh with 450 elements.

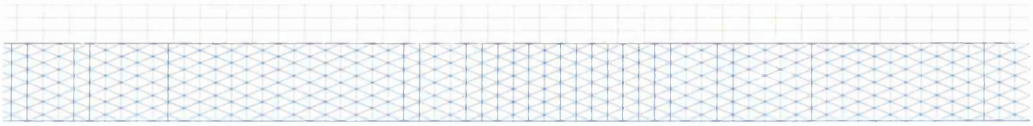

(c) Detail of the fluid mesh with 3250 elements and solid mesh with 450 elements.

Figure 6.21: Flow through a channel with a flexible wall: Geometry, mesh and detail of the mesh.

$\rho^f = 0.998$. The solid properties are given by the solid viscosity $\mu^s = 0.1$, bulk modulus $K^s = 5$ and solid density $\rho^s = 0.1$.

The inflow velocity is described by a Wormersley profile. The Wormersley velocity profile is a steady flow condition that arises due to a developed periodic flow through a circular pipe. In certain regions blood flow can be approximated by the Womersley profile. The velocity profile is described as follows [55]:

$$w(r,t) = \frac{2B_0}{\pi R^2}\left[1-\left(\frac{r}{R}\right)^2\right] + \sum_{n-1}^{N}\frac{B_n}{\pi R^2}\left[\frac{1-\frac{J_0\left(\alpha_n \frac{r}{R} \mathrm{i}^{3/2}\right)}{J_0\left(\alpha_n \mathrm{i}^{3/2}\right)}}{1-\frac{2J_1\left(\alpha_n \mathrm{i}^{3/2}\right)}{\alpha_n \mathrm{i}^{3/2} J_0\left(\alpha_n \mathrm{i}^{3/2}\right)}}\right] \mathrm{e}^{\mathrm{i}n\omega t} \qquad (6.3)$$

where r and R denote respectively the cylindrical coordinate and the radius of the inlet cross-section, and J_0 and J_1 are the Bessel functions of the first kind

of order 0 and 1. The dimensionless parameter α is known as the Womersley number and defined as

$$\alpha = R\sqrt{\omega/\nu}. \tag{6.4}$$

Similarly

$$\alpha_n = R\sqrt{n\omega/\nu}. \tag{6.5}$$

The frequency ω is based on the cardiac function and the Bessel coefficients B_n can be obtained by performing measurements. Ultrasound Doppler velocimetry can be used to derive a velocity profile, which then can be used to fit the Bessel coefficients [55]:

$$Q(t) = \sum_{n=0}^{N} B_n e^{i\omega t}. \tag{6.6}$$

In here, however, no measured data is used. The Bessel coefficients B_n are found by fitting a standard cosine volume flow. The inflow profile is calculated using $B_0 = 0.0392699$ and $B_1 = -0.0392699$ and $\omega = 10$.

The problem is solved using the mesh shown in Figure 6.21(b), with a detail of the mesh shown in Figure 6.21(c). The fluid domain consists of 3250 elements, whereas the solid domain is modelled with 450 eight noded quadrilateral elements. The entire fluid domain is modelled as a ALE region, where the mesh update is performed by the pseude-elastic technique. The generalised-α method is used for integration in time, with the following parameters: $\rho_\infty^f = 0.85$ and $\rho_\infty^f = 0.7$.

The outflow velocity versus the inflow velocity is shown in Figure 6.22. The velocity is calculated at the center of the pipe. It is observed that it takes approximately 15 seconds for the outflow velocity to reach a stable long term response. The flexible pipe damps out the variations of the flow velocity, however, the average inflow and outflow velocities are equal. The outflow velocity is shown again in Figure 6.23, for time step sizes $\Delta t = 0.02$, $\Delta t = 0.01$ and $\Delta t = 0.005$. It can be seen that the response for the different time step sizes deviates only by a small amount, so for the remaining of this section a time step size of $\Delta t = 0.02$ is used. For different time instances a contour plot of the vorticity is shown in Figure 6.24.

6.3.2 Simulations

To compare the different solution strategies, the problem is solved using the monolithic strategy (MN), the partioned Newton strategy (PN) and the

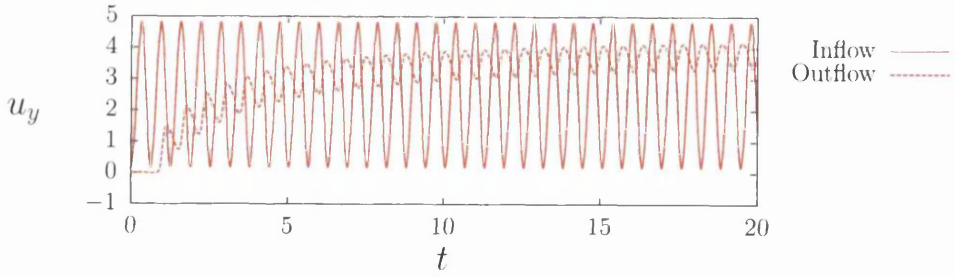

Figure 6.22: Inflow velocity vs outflow velocity in time.

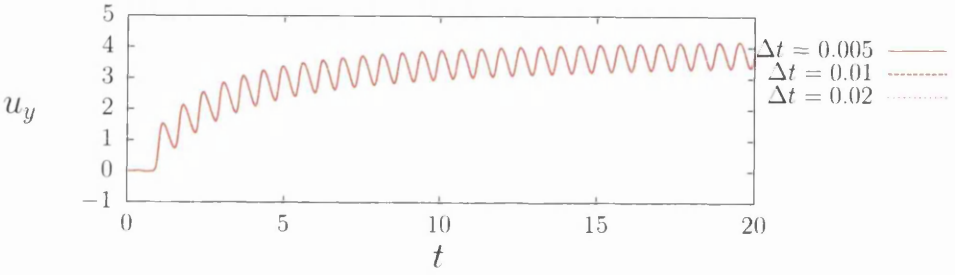

Figure 6.23: Outflow velocity at the center of the pipe for time step sizes $\Delta t = 0.02$, $\Delta t = 0.01$ and $\Delta t = 0.005$.

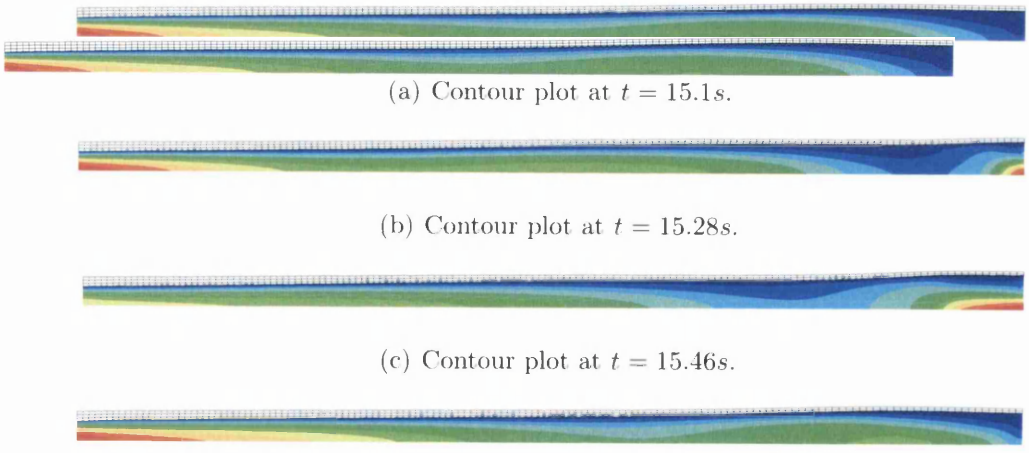

(a) Contour plot at $t = 15.1s$.

(b) Contour plot at $t = 15.28s$.

(c) Contour plot at $t = 15.46s$.

(d) Contour plot at $t = 15.64s$.

Figure 6.24: Contour plots for the flow through a flexible pipe at different time instances.

Gauß-Seidel strategies with no relaxation (GS), constant relaxation (GS-FR) and adaptive relaxation (GS-AR). The number of iterations n that were needed per time step are shown in Figure 6.25(a). It can be noted that only for the monolithic strategy and the partitioned Newton strategies a solution was found. All other strategies experienced divergence and failed to solve the problem. The monolithic strategy and the partitioned Newton strategy give similar results in terms of number of iterations per time step. The average number of time steps $\bar{n}$ is given in Table 6.7.

The amount of time t^* that was needed per time step is shown in Figure 6.25(b). The monolithic strategy needs significantly less time per time step, which also becomes clear from the average amount of time $\bar{t^*}$, as shown in Table 6.8. It is concluded that for this problem the monolithic strategy performs best, however, it may be possible to improve computational time regarding the partitioned Newton strategy.

In order to establish whether the ratio between the solid and fluid mass again is an important factor in the failure of the Gauß-Seidel strategies, the problem is solved with a higher solid density. It is noted that this will completely change the physical properties of the model and it will no longer relate to any physical problem.

The density of the solid is set to $\rho^s = 1$. The number of iterations n and the amount of time t^* that are needed per time step are shown in respectively Figure 6.26(a) and Figure 6.26(b). Again the Gauß-Seidel strategies failed to solve the problem. The number of iterations n is similar for both the monolithic strategy and the partitioned Newton strategy and the computational time t^* is much smaller for the monolithic strategy again.

6.3.3 Conclusion

The problem that describes a flow through a flexible pipe has been solved for the different solution strategies. For only two of the strategies (MN and PN) a solution is obtained succesfully. Increasing the density of the solid does not improve the performance of the Gauß-Seidel strategies for this case. It is concluded that the monolithic strategy gives the best performance when solving the problem of a flow through a flexible pipe.

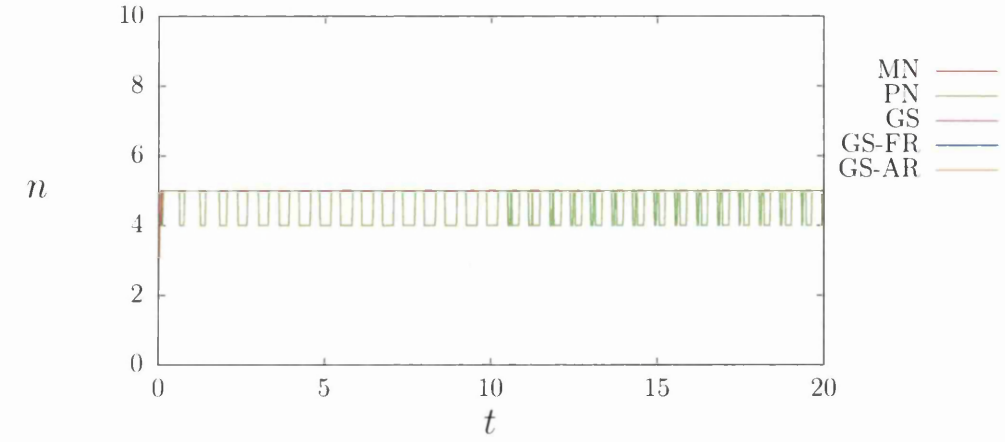

(a) Number of iterations per time step

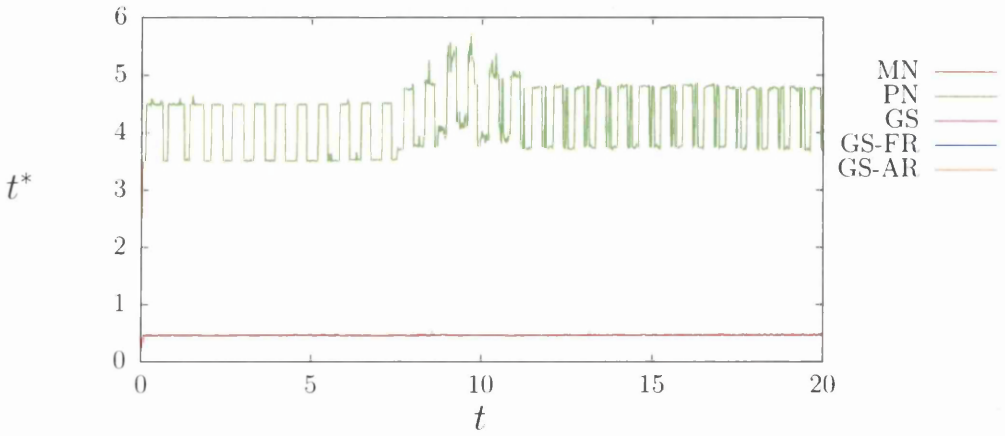

(b) Computational time per time step

Figure 6.25: Flow through a flexible pipe: The number of iterations n and computational time t^* per time step needed for convergence with time step size $\Delta t = 0.02$.

	$\bar{n}$	$\bar{t}^*$
MN	5.0	0.47
PN	4.6	4.38
GS	x	x
GS-FR	x	x
GS-AR	x	x

Table 6.7: Flow through a flexible pipe: The average number of iterations $\bar{n}$ and average computational time $\bar{t}^*$ for each solution strategy, using $\Delta t = 0.02$.

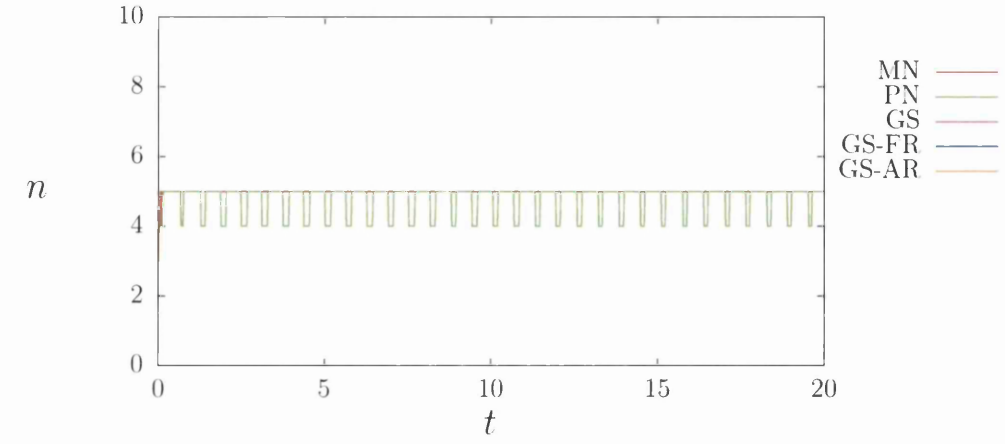

(a) Number of iterations per time step

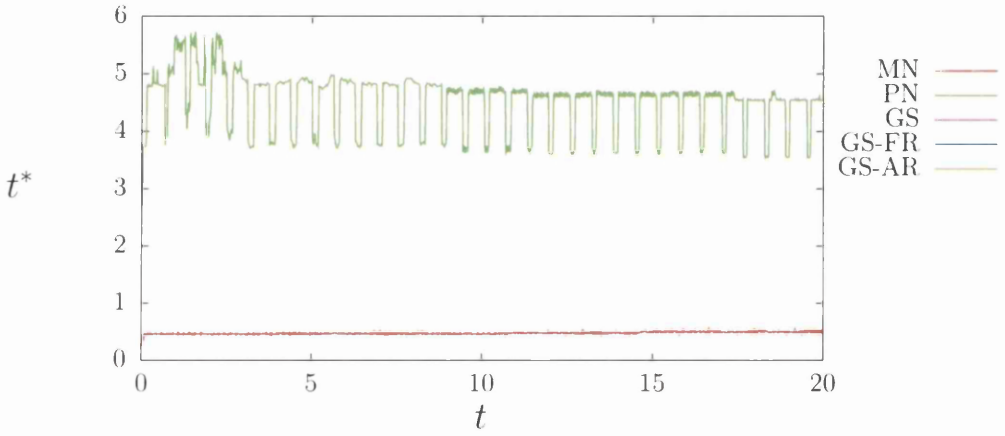

(b) Computational time per time step

Figure 6.26: Flow through a flexible pipe: The number of iterations n and computational time t^* per time step needed for convergence with time step size $\Delta t = 0.02$.

	$\bar{n}$	$\bar{t}^*$
MN	5.0	0.50
PN	4.8	4.41
GS	x	x
GS-FR	x	x
GS-AR	x	x

Table 6.8: Flow through a flexible pipe: The average number of iterations $\bar{n}$ and average computational time $\bar{t}^*$ for each solution strategy, using $\Delta t = 0.02$.

Chapter 7

Conclusions

In this work different aspects of interface modelling in fluid-structure interaction problems are discussed. Fluid-structure interaction problems are coupled problems where a fluid domain and a solid domain interact with each other. The fluid domain is described with the Navier-Stokes equations which are solved using the Petrov-Galerkin method. The solid domain is assumed to be compressible and solved using the finite element method as well.

The interface between the fluid and solid domain is modelled as a separate domain. The transfer of solution variables at the interface is based on finite element type interpolation between the nodes. To perform the coupling between the domains, weakly or strongly coupled strategies can be applied. In here, only the strongly coupled solution strategies are considered. The strongly coupled strategies consists of monolithic and partitioned methods. For the monolithic scheme, the entire set of equations is solved simultaneously using a Newton-Rapshon procedure. A Newton-Raphson procedure is also used for the partitioned block Newton scheme, where parts of the assembled stiffness matrix are eliminated before the solution process. The other solution strategies considered are the Gauß-Seidel procedures. Gauß-Seidel strategies are strongly coupled schemes where the fluid and solid domain are solved seperately, without the need for a specific interface domain. Three variations of the Gauß-Seidel solution procedure are considered, one without any form of relaxation, one with fixed relaxation and one with adaptive relaxation.

For the discretisation in time, single step time integration schemes are used. The trapezoidal rule, backward Euler method, generalised midpoint

rule and the generalised-α method are discussed to allow detailed analysis of several model problems. The stability and accuracy properties of the schemes are derived and terminology is introduced. This leads to the investigation of the situation where different time integration schemes are used for the different domains in coupled problems. For a model problem it is shown that when two different time integration schemes are used, the stability and accuracy properties of the individual schemes are not maintained. However, it is noted that the traction forces for both domains at the interface are not evaluated at the same time instance and therefore interpolation of the traction forces is suggested. It has been shown that this gives good results and that after appropiate interpolation of all transferred solution variables at the interface, stability and accuracy properties can be maintained. The same interpolation strategy is applied to a 2D fluid-structure interaction problem, which confirms the findings obtained with the 1D model problem.

From the solution strategies discussed in this work, the Gauß-Seidel strategy is analysed in more detail as this method is known to have limited stability properties. To analyse the limitations, another 1D model problem is introduced. The problem is discretised with the trapezoidal rule and the backward Euler method. The set of equations that describes the problem is rewritten so that one iteration step is captured. This gives an amplification factor which determines whether the system will converge or not. It is shown in this work that the amplification factor depends on the ratio between the masses of the two domains. This leads to the conclusion that for certain mass ratios the Gauß-Seidel solution strategy will fail to solve the coupled problem. This issue can be overcome by applying a type of relaxation. Improved stability properties can be obtained by applying constant relaxation. For the linear model problem it is shown that an optimal relaxation parameter exists. The presence of a constraint gives similar results. For a nonlinear problem it is no longer possible to derive an optimal relaxation parameter. For this case it is beneficial to introduce adaptive relaxation, which for the model problem leads to extremely fast convergence. The findings of the simulations with the model problems are confirmed for a 2D fluid-structure interaction problem, for which it is shown that the mass ratio influences the convergence behaviour and that applying relaxation improves the convergence behaviour.

For three different numerical examples the previously mentioned solution strategies are compared with each other. The three examples consider a flow around a flexible beam, a flow through a channel with a flexible wall and a flow through a flexible pipe. The first example deals with large deformations of the structure, the second one has a solid domain consisting of solid

membrane elements which cover the entire interface (and thus no internal solid nodes are present) and the last example deals with a relatively large interface between the fluid and the solid domain. Based on the three numerical examples it can be concluded that the monolithic strategy and the partitioned Newton strategy are performing best in terms of number of iterations that are needed per time step. At this stage the monolithic strategy is the best performing strategy in terms of computational time, however, it is thought that for the partitioned Newton strategy, computational time can be reduced by parallellisation of the computer code. In terms of implementation the Gauß-Seidel strategy is the best option, as this strategy can be implemented using existing codes for the fluid and the solid domain, but the limitations of its stability are a major drawback. For an ultimate comparison of all solution strategies, the simulation of 3D fluid-structure interaction problems is required.

Bibliography

[1] M. Fernández and M. Moubachir, "A newton method using exact jacobians for solving fluid-structure coupling," *Computers and Structures*, vol. 83, pp. 127–142, 2005.

[2] M. Fernández, J.-F. Gerbeau, and C. Grandmont, "A projection semi-implicit scheme for the coupling of an elastic structure with an incompressible fluid," *International Journal for Numerical Methods in Engineering*, vol. 69, pp. 794–821, 2007.

[3] W. Dettmer and D. Perić, "A computational framework for fluid-rigid body interaction: Finite element formulation and applications," *Computer Methods in Applied Mechanics and Engineering*, vol. 195, pp. 1633–1666, 2006.

[4] W. Dettmer and D. Perić, "A computational framework for fluid-structure interaction: Finite element formulation and applications," *Computer Methods in Applied Mechanics and Engineering*, vol. 195, pp. 5754–5779, 2006.

[5] W. Dettmer and D. Perić, "A fully implicit computational strategy for strongly coupled fluid-solid interaction," *Archives of Computational Methods in Engineering*, vol. 14, pp. 205–247, 2007.

[6] P. Saksono, W. Dettmer, and D. Perić, "An adaptive remeshing strategy for flows with moving boundaries and fluid-structure interaction," *International Journal for Numerical Methods in Engineering*, vol. 71, pp. 1009–1050, 2007.

[7] W. Dettmer and D. Perić, "On the coupling between fluid flow and mesh motion in the modelling of fluid-structure interaction," *Computational Mechanics*, vol. 43, pp. 81–90, 2008.

[8] T. Tezduyar, "Finite element methods for flow problems with moving boundaries and interfaces," *Archives of Computational Methods in Engineering*, vol. 8, pp. 83–130, 2001.

[9] T. Tezduyar and S. Sathe, "Modelling of fluidstructure interactions with the spacetime finite elements: solution techniques," *International Journal for Numerical Methods*, vol. 54, pp. 855–900, 2007.

[10] H. Matthies and J. Steindorf, "Partitioned strong coupling algorithms for fluid-structure interaction," *Computers and Structures*, vol. 81, pp. 805–812, 2003.

[11] H. G. Matthies, R. Niekamp, and J. Steindorf, "Algorithms for strong coupling procedures," *Computer Methods in Applied Mechanics and Engineering*, vol. 195, pp. 2028–2049, 2006.

[12] B. Hübner, E. Walhorn, and D. Dinkler, "A monolithic approach to fluid-structure interaction using space-time finite elements," *Computer Methods in Applied Mechanics and Engineering*, vol. 193, pp. 2087–2104, 2004.

[13] S. Piperno, C. Farhat, and B. Larrouturou, "Partitioned procedures for the transient solution of coupled aeroelastic problems. part 1: Model problem, theory and two-dimensional application," *Computer Methods in Applied Mechanics and Engineering*, vol. 124, pp. 79–112, 1995.

[14] C. Felippa, K. Park, and C. Farhat, "Partitioned analysis of coupled mechanical systems," *Computer Methods in Applied Mechanics and Engineering*, vol. 190, pp. 3247–3270, 2001.

[15] C. Farhat, K. van der Zee, and P. Geuzaine, "Provably second-order time-accurate loosely-coupled soltuion algorithms for transient nonlinear computational aeroelasticity," *Computer Methods in Applied Mechanics and Engineering*, vol. 195, pp. 1973–2001, 2006.

[16] U. Küttler and W. Wall, "Fixed-point fluid-structure interaction solvers with dynamic relaxation," *Computational Mechanics*, vol. 43, pp. 61–72, 2008.

[17] D. Sternel, M. Schäfer, M. Heck, and S. Yigit, "Efficiency and accuracy of fluid-structure interaction simulations using an implicit partitioned approach," *Computational Mechanics*, vol. 43, pp. 103–113, 2008.

[18] M. Joosten, W. Dettmer, and D. Perić, "On the temporal stability and accuracy of coupled problems with reference to fluid-structure interaction," *International Journal for Numerical Methods in Fluids*, vol. 64, pp. 1363–1378, 2010.

[19] M. Joosten, W. Dettmer, and D. Perić, "Analysis of the block gauss-seidel solution procedure for a strongly coupled model problem with reference to fluid-structure interaction," *International Journal for Numerical Methods in Engineering*, vol. 78, pp. 757–778, 2009.

[20] E. Turska and B. Schrefler, "On convergence conditions of partitioned solution procedures for consolidation problems," *Computer Methods in Applied Mechanics and Engineering*, vol. 106, pp. 51–63, 1993.

[21] F. Armero and J. Simo, "A new unconditionally stable fractional step method for nonlinear coupled thermomechanical problems," *International Journal for Numerical Methods in Engineering*, vol. 35, pp. 737–756, 1992.

[22] T. J. R. Hughes, *The Finite Element Method, Linear Static and Dynamic Finite Element Analysis.* New York: Dover Publications, 2000.

[23] O. Zienkiewicz, R. Taylor, and J. Zhu, *The Finite Element Method, it's basis & fundamentals.* Butterworth-Heinemann, 6th ed., 2005.

[24] W. Wall, *Fluid-Struktur-Interaktion mit stabilisierten Finiten Elementen.* Phd thesis, Stuttgart University, 1999.

[25] W. Dettmer, *Finite Element Modelling of Fluid Flow with Moving Free Surfaces and Interfaces Including Fluid-Solid Interaction.* Phd thesis, University of Wales Swansea, 2004.

[26] C. Johnson, *Numerical Solution of Partial Differential Equations by the Finite Element Method.* Cambridge: Cambridge University Press, 1987.

[27] C. Hirsch, *Numerical Computation of Internal and External Flows.* John Wiley, 1988.

[28] T. J. R. Hughes, L. P. Franca, and G. M. Hulbert, "A new finite element formulation for computational fluid dynamics: Viii. the galerkin/least-squares method for advective-diffusive equations," *Methods in Applied Mechanics and Engineering*, vol. 73, pp. 173–189, 1989.

[29] T. J. R. Hughes, L. P. Franca, and M. Balestra, "A new finite element formulation for computational fluid dynamics: V. circumventing the babuska-brezzi condition: A stable petrov-galerkin formulation of the stokes problem accommodating equal-order interpolations," *Methods in Applied Mechanics and Engineering*, vol. 59, pp. 85–99, 1986.

[30] I. Babuška, "Error bounds for the finite element method," *Numerische Mathematik*, vol. 16, pp. 322–333, 1971.

[31] F. Brezzi, "On the existence, uniqueness and approximation of saddlepoint problems arising from lagrange multipliers," *Revue Francaise d'Automatique, d'Informatique et de Recherche Operationnelle. Serie Rouge, Analyse Numerique*, vol. 8, pp. 129–151, 1974.

[32] W. Dettmer and D. Perić, "A fully implicit computational strategy for strongly coupled fluid-solid interaction," *Archives of Computational Methods in Engineering*, vol. 14, pp. 205–247, 2007.

[33] O. Axelsson, *Iterative Solution Methods*. Cambridge: Cambridge University Press, 1996.

[34] B. Schrefler, L. Simoni, and E. Turska, "Standard staggered and staggered newton schemes in thermo-hydro-mechanical problems," *Computer Methods in Applied Mechanics and Engineering*, vol. 144, pp. 93–109, 1997.

[35] P. Vijalapura and S. Govindjee, "An adaptive hybrid time-stepping scheme for highly non-linear strongly coupled problems," *International Journal for Numerical Methods in Engineering*, vol. 64, pp. 819–848, 2005.

[36] W. Dettmer and D. Perić, "An analysis of the time integration algorithm for the finite element solutions of incompressible navier-stokes equations based on a stabilised formulation," *Computer Methods in Applied Mechanics and Engineering*, vol. 192, pp. 1177–1226, 2003.

[37] J. Chung and G. Hulbert, "A time integration algorithm for structural dynamics with improved numerical dissipation: The generalized-α method," *Journal of Applied Mechanics*, vol. 60, pp. 371–375, 1993.

[38] K. Jansen, C. Whiting, and G. Hulbert, "A generalized-α method for integrating the filtered navier-stokes equations with a stabilized finite element method," *Computer Methods in Applied Mechanics and Engineering*, vol. 190, pp. 305–319, 2000.

[39] M. K. Jain, *Numerical Solution of Differential Equations.* New Delhi: Wiley Eastern Limited, 1979.

[40] M. T. Heath, *Scientific Computing, An Introductory Survey.* New York: McGraw-Hill Higher Education, second ed., 2002.

[41] B. Hübner and D. Dinkler, "A simultaneous solution procedure for strong interactions of generalised newtonian fluids and viscoelastic solids at large strains," *International Journal for Numerical Methods in Engineering*, vol. 64, pp. 920–939, 2005.

[42] Y. Bazilevs, V. Calo, T. Hughes, and Y. Zhang, "Isogeometric fluid-structure interaction: theory, algorithms, and computations," *Computational Mechanics*, vol. 43, pp. 3–37, 2008.

[43] M. Heil, A. Hazel, and J. Boyle, "Solvers for large-displacement fluid-structure interaction problems: segregated versus monolithic approaches," *Computational Mechanics*, vol. 43, pp. 91–101, 2008.

[44] R. Löhner, C. Yang, and E. Oñate, "Simulation of flows with violent free surface motion and moving objects using unstructured grids," *International Journal for Numerical Methods in Fluids*, vol. 53, pp. 1315–1338, 2007.

[45] T. Tezduyar, M. Schwaab, and S. Sathe, "Sequentially-coupled arterial fluid-structure interaction (scafsi) technique," *Computer Methods in Applied Mechanics and Engineering*, vol. 198, pp. 3524–3533, 2009.

[46] W. Dettmer and D. Perić, "A computational framework for free surface fluid flows accounting for surface tension," *Computer Methods in Applied Mechanics and Engineering*, vol. 195, pp. 3038–3071, 2006.

[47] P. Causin, J. Gerbeau, and F. Nobile, "Added-mass effect in the design of partitioned algorithms for fluid-structure problems," *Computer Methods in Applied Mechanics and Engineering*, vol. 194, pp. 4506–4527, 2005.

[48] U. Küttler, C. Förster, and W. A. Wall, "A solution for the incompressibility dilemma in partitioned fluid-structure interaction with pure dirichlet fluid domains," *Computational Mechanics*, vol. 38, pp. 417–429, 2006.

[49] C. Förster, W. A. Wall, and E. Ramm, "Artificial added mass instabilities in sequential staggered coupling of nonlinear structures and incompressible viscous flows," *Computer Methods in Applied Mechanics and Engineering*, vol. 196, pp. 1278–1293, 2007.

[50] P. G. Ciarlet, *Introduction to Numerical Linear Algebra and Optimisation.* Cambridge Texts in Applied Mathematics, Cambridge University Press, 1989.

[51] B. M. Irons and R. C. Tuck, "A version of the aitken accelerator for computer iteration," *International journal of numerical methods in engineering*, vol. 1, pp. 275–277, 1969.

[52] D. P. Mok and W. A. Wall, "Partitioned analysis schemes for the transient interaction of incompressible flows and nonlinear flexible structures in w. a. wall, k.-u. bletzinger and k. schweitzerhof (editors)," *Trends in Computational Structural Mechanics*, 2001.

[53] X. Y. Luo and T. J. Pedley, "A numerical simulation of unsteady flow in a two-dimensional collapsible channel," *Journal of Fluid Mechanics*, vol. 314, pp. 191–225, 1996.

[54] M. Heil, "An efficient solver for the fully coupled solution of large-displacement fluid-structure interaction problems," *Computer Methods in Applied Mechanics and Engineering*, vol. 193, pp. 1–23, 2004.

[55] R. Torii, M. Oshima, T. Kobayashi, K. Takagi, and T. E. Tezduyar, "Computer modeling of cardiovascular fluid-structure interactions with the deforming-spatial-domain/stabilized space-time formulation," *Computer Methods in Applied Mechnanics and Engineering*, vol. 195, pp. 1885–1895, 2006.

Appendix A

Contour plots for eigenvalue analysis - Part 1

To analyse the stability of the coupled problem (described by Equation (4.14)), the eigenvalues of the amplification matrix are calculated and the absolute value of the largest eigenvalue $|\zeta^h|_{\max}$ is plotted as a function of α and $\Delta t/T$ for a range of values for ξ, ω, ρ_∞^s and ρ_∞^f. The eigenvalues are calculated using a symbolic toolbox. Every contour plot consists of 2013 data points; 61 points from $\Delta t/T = 0.001$ to $\Delta t/T = 1000$ and 33 points from $\alpha = 0.1$ to $\alpha = 0.9$.

There are 32 contour plots on the following pages. The natural frequency ω is constant ($\omega = 1.0$), as the influence of ω on the behaviour of the system is captured by characteristic time period T. For the first 16 plots the dimensionless damping ratio is set to $\xi = 0.01$ and for the last 16 plots this value is set to $\xi = 0.001$. Within each of these sets of 16 plots, various combinations of ρ_∞^s and ρ_∞^f are used.

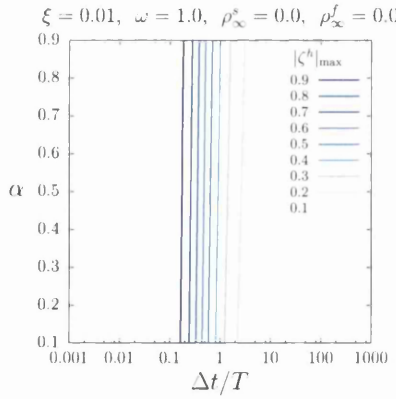
$\xi = 0.01,\ \omega = 1.0,\ \rho^s_\infty = 0.0,\ \rho^f_\infty = 0.0$
$|\zeta^h|_{\max}$
0.9
0.8
0.7
0.6
0.5
0.4
0.3
0.2
0.1
α
$\Delta t/T$

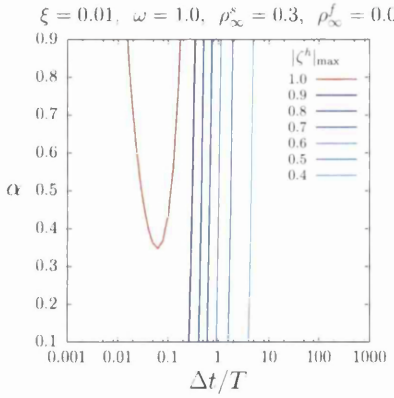
$\xi = 0.01,\ \omega = 1.0,\ \rho^s_\infty = 0.3,\ \rho^f_\infty = 0.0$
$|\zeta^h|_{\max}$
1.0
0.9
0.8
0.7
0.6
0.5
0.4
α
$\Delta t/T$

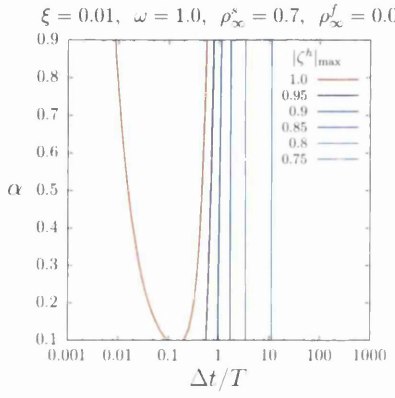
$\xi = 0.01,\ \omega = 1.0,\ \rho^s_\infty = 0.7,\ \rho^f_\infty = 0.0$
$|\zeta^h|_{\max}$
1.0
0.95
0.9
0.85
0.8
0.75
α
$\Delta t/T$

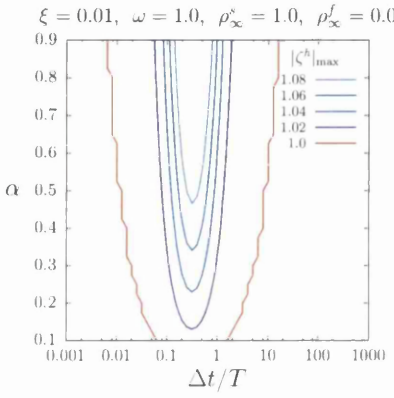
$\xi = 0.01,\ \omega = 1.0,\ \rho^s_\infty = 1.0,\ \rho^f_\infty = 0.0$
$|\zeta^h|_{\max}$
1.08
1.06
1.04
1.02
1.0
α
$\Delta t/T$

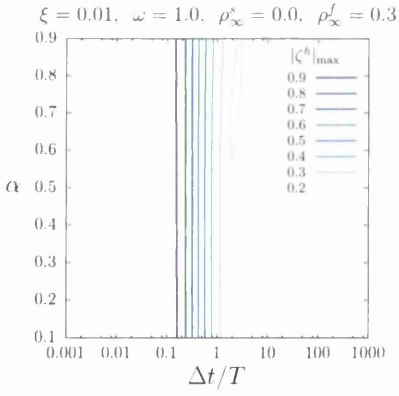
$\xi = 0.01,\ \omega = 1.0,\ \rho^s_\infty = 0.0,\ \rho^f_\infty = 0.3$
$|\zeta^h|_{\max}$
0.9
0.8
0.7
0.6
0.5
0.4
0.3
0.2
α
$\Delta t/T$

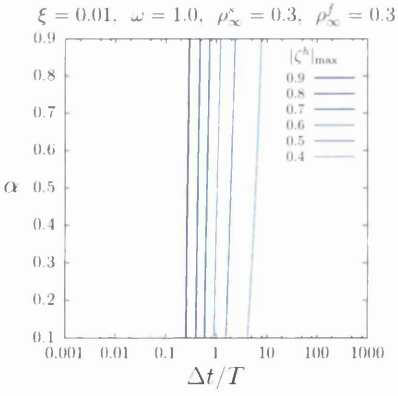
$\xi = 0.01,\ \omega = 1.0,\ \rho^s_\infty = 0.3,\ \rho^f_\infty = 0.3$
$|\zeta^h|_{\max}$
0.9
0.8
0.7
0.6
0.5
0.4
α
$\Delta t/T$

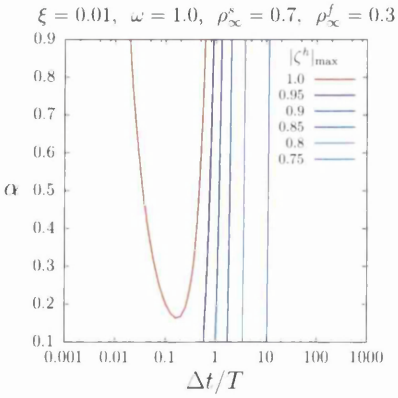
$\xi = 0.01,\ \omega = 1.0,\ \rho^s_\infty = 0.7,\ \rho^f_\infty = 0.3$
$|\zeta^h|_{\max}$
1.0
0.95
0.9
0.85
0.8
0.75
α
$\Delta t/T$

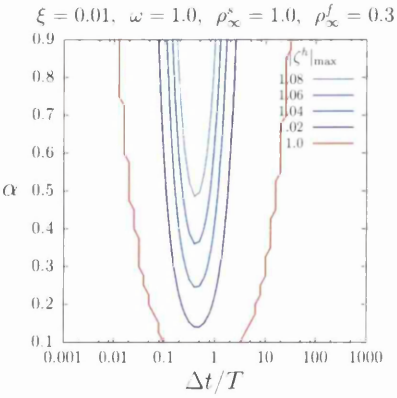
$\xi = 0.01,\ \omega = 1.0,\ \rho^s_\infty = 1.0,\ \rho^f_\infty = 0.3$
$|\zeta^h|_{\max}$
1.08
1.06
1.04
1.02
1.0
α
$\Delta t/T$

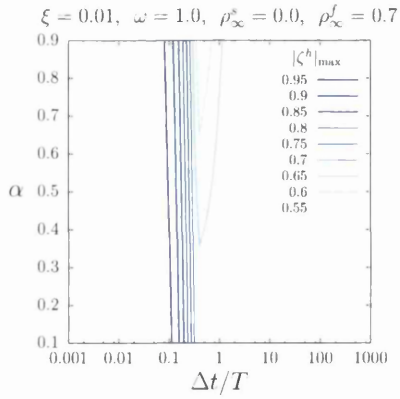
$\xi = 0.01,\ \omega = 1.0,\ \rho^s_\infty = 0.0,\ \rho^f_\infty = 0.7$
$|\zeta^h|_{\max}$
0.95
0.9
0.85
0.8
0.75
0.7
0.65
0.6
0.55
α
$\Delta t/T$

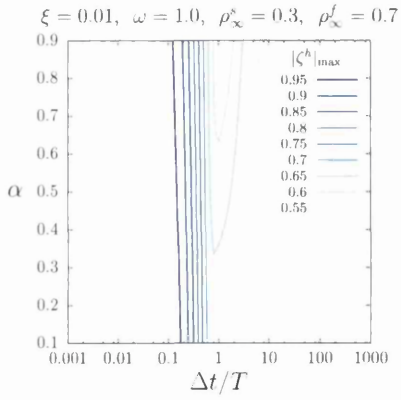
$\xi = 0.01,\ \omega = 1.0,\ \rho^s_\infty = 0.3,\ \rho^f_\infty = 0.7$
$|\zeta^h|_{\max}$
0.95
0.9
0.85
0.8
0.75
0.7
0.65
0.6
0.55
α
$\Delta t/T$

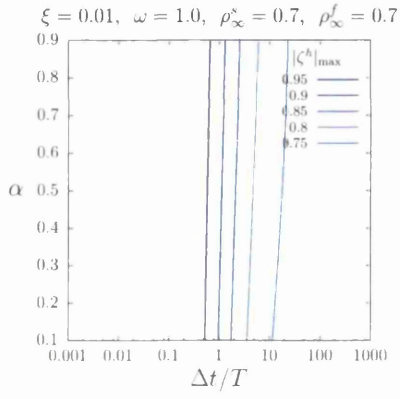
$\xi = 0.01,\ \omega = 1.0,\ \rho^s_\infty = 0.7,\ \rho^f_\infty = 0.7$
$|\zeta^h|_{\max}$
0.95
0.9
0.85
0.8
0.75
α
$\Delta t/T$

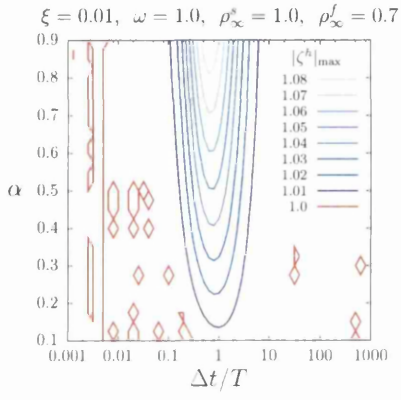
$\xi = 0.01,\ \omega = 1.0,\ \rho^s_\infty = 1.0,\ \rho^f_\infty = 0.7$
$|\zeta^h|_{\max}$
1.08
1.07
1.06
1.05
1.04
1.03
1.02
1.01
1.0
α
$\Delta t/T$

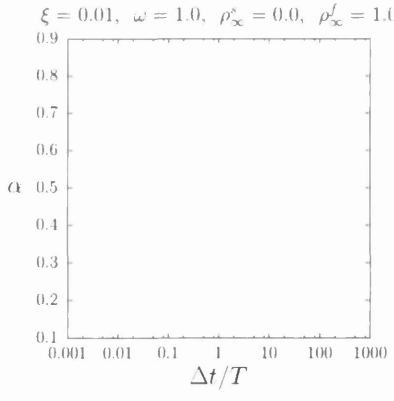
$\xi = 0.01,\ \omega = 1.0,\ \rho^s_\infty = 0.0,\ \rho^f_\infty = 1.0$
α
$\Delta t/T$

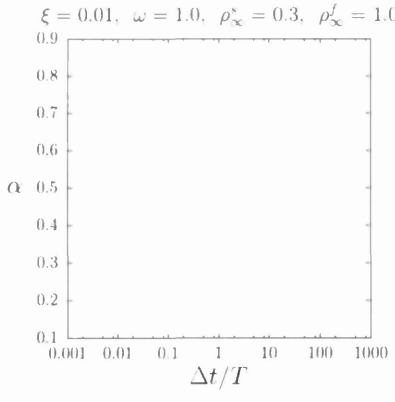
$\xi = 0.01,\ \omega = 1.0,\ \rho^s_\infty = 0.3,\ \rho^f_\infty = 1.0$
α
$\Delta t/T$

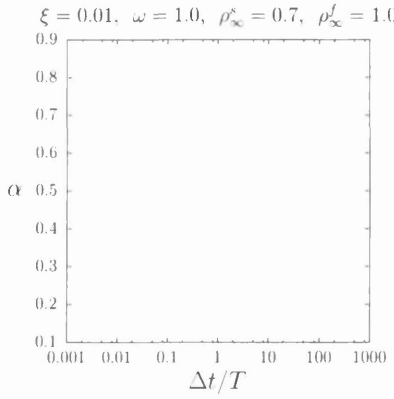
$\xi = 0.01,\ \omega = 1.0,\ \rho^s_\infty = 0.7,\ \rho^f_\infty = 1.0$
α
$\Delta t/T$

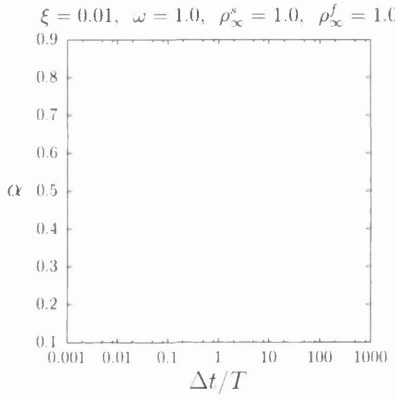
$\xi = 0.01,\ \omega = 1.0,\ \rho^s_\infty = 1.0,\ \rho^f_\infty = 1.0$
α
$\Delta t/T$

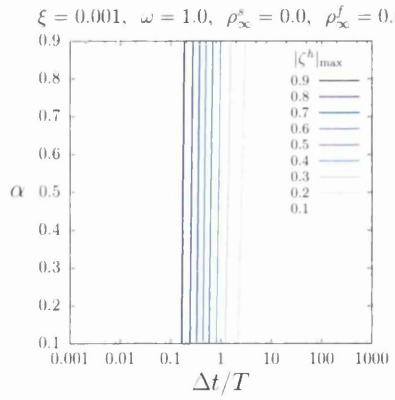
$\xi = 0.001,\ \omega = 1.0,\ \rho^s_\infty = 0.0,\ \rho^f_\infty = 0.0$
$|\zeta^h|_{\max}$
0.9
0.8
0.7
0.6
0.5
0.4
0.3
0.2
0.1
α
$\Delta t/T$

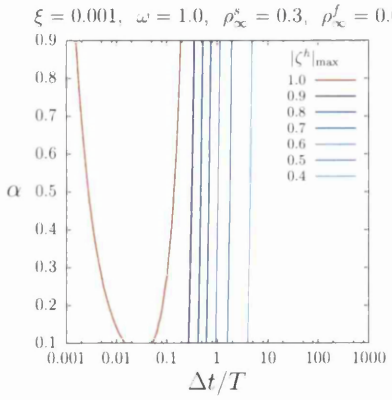
$\xi = 0.001,\ \omega = 1.0,\ \rho^s_\infty = 0.3,\ \rho^f_\infty = 0.0$
$|\zeta^h|_{\max}$
1.0
0.9
0.8
0.7
0.6
0.5
0.4
α
$\Delta t/T$

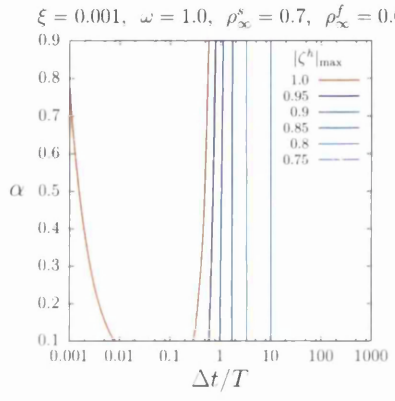
$\xi = 0.001,\ \omega = 1.0,\ \rho^s_\infty = 0.7,\ \rho^f_\infty = 0.0$
$|\zeta^h|_{\max}$
1.0
0.95
0.9
0.85
0.8
0.75
α
$\Delta t/T$

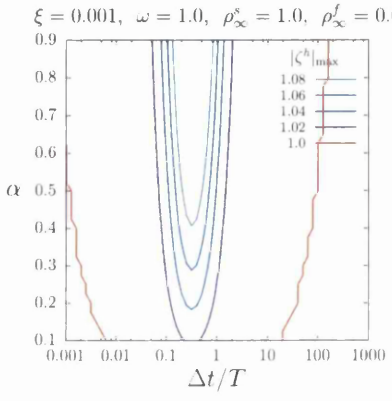
$\xi = 0.001,\ \omega = 1.0,\ \rho^s_\infty = 1.0,\ \rho^f_\infty = 0.0$
$|\zeta^h|_{\max}$
1.08
1.06
1.04
1.02
1.0
α
$\Delta t/T$

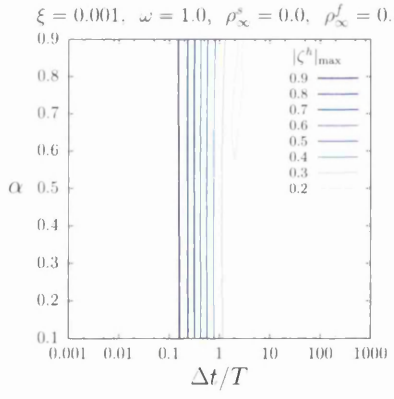
$\xi = 0.001,\ \omega = 1.0,\ \rho^s_\infty = 0.0,\ \rho^f_\infty = 0.3$
$|\zeta^h|_{\max}$
0.9
0.8
0.7
0.6
0.5
0.4
0.3
0.2
α
$\Delta t/T$

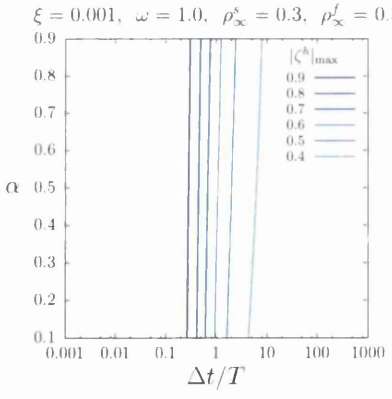
$\xi = 0.001,\ \omega = 1.0,\ \rho^s_\infty = 0.3,\ \rho^f_\infty = 0.3$
$|\zeta^h|_{\max}$
0.9
0.8
0.7
0.6
0.5
0.4
α
$\Delta t/T$

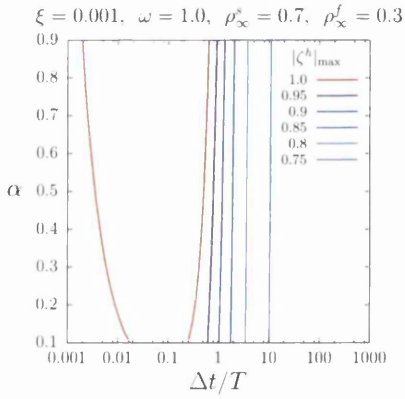
$\xi = 0.001,\ \omega = 1.0,\ \rho^s_\infty = 0.7,\ \rho^f_\infty = 0.3$
$|\zeta^h|_{\max}$
1.0
0.95
0.9
0.85
0.8
0.75
α
$\Delta t/T$

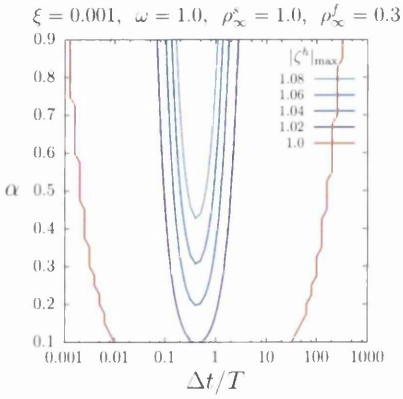
$\xi = 0.001,\ \omega = 1.0,\ \rho^s_\infty = 1.0,\ \rho^f_\infty = 0.3$
$|\zeta^h|_{\max}$
1.08
1.06
1.04
1.02
1.0
α
$\Delta t/T$

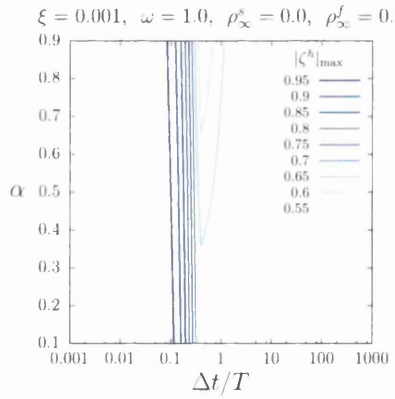
$\xi = 0.001,\ \omega = 1.0,\ \rho^s_\infty = 0.0,\ \rho^f_\infty = 0.7$
$|\zeta^h|_{\max}$
0.95
0.9
0.85
0.8
0.75
0.7
0.65
0.6
0.55
α
$\Delta t/T$

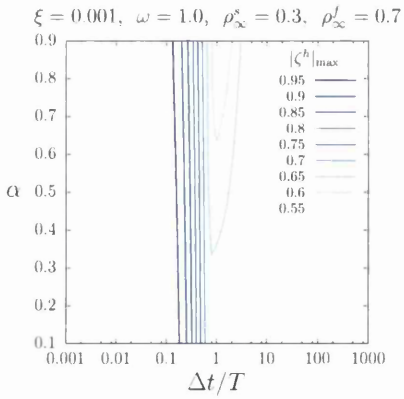
$\xi = 0.001,\ \omega = 1.0,\ \rho^s_\infty = 0.3,\ \rho^f_\infty = 0.7$
$|\zeta^h|_{\max}$
0.95
0.9
0.85
0.8
0.75
0.7
0.65
0.6
0.55
α
$\Delta t/T$

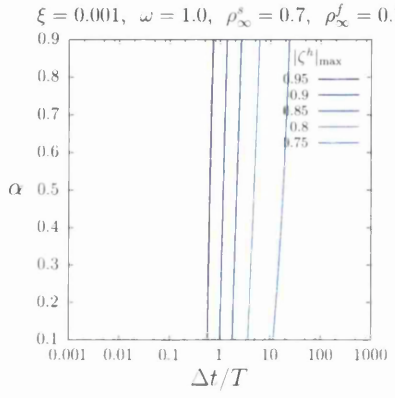
$\xi = 0.001,\ \omega = 1.0,\ \rho^s_\infty = 0.7,\ \rho^f_\infty = 0.7$
$|\zeta^h|_{\max}$
0.95
0.9
0.85
0.8
0.75
α
$\Delta t/T$

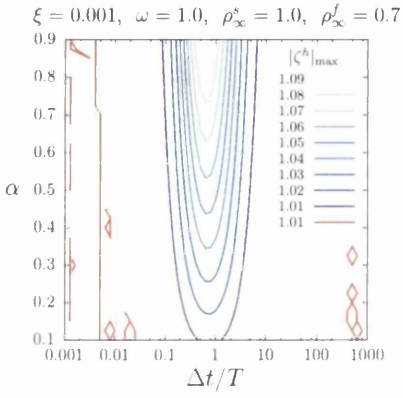
$\xi = 0.001,\ \omega = 1.0,\ \rho^s_\infty = 1.0,\ \rho^f_\infty = 0.7$
$|\zeta^h|_{\max}$
1.09
1.08
1.07
1.06
1.05
1.04
1.03
1.02
1.01
1.01
α
$\Delta t/T$

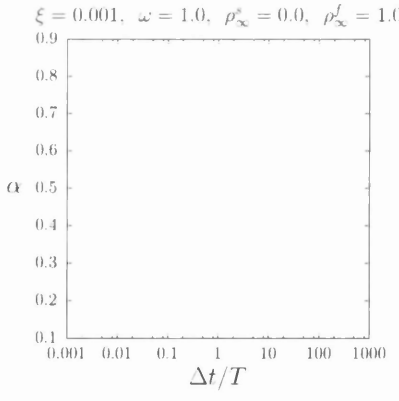
$\xi = 0.001,\ \omega = 1.0,\ \rho^s_\infty = 0.0,\ \rho^f_\infty = 1.0$
α
$\Delta t/T$

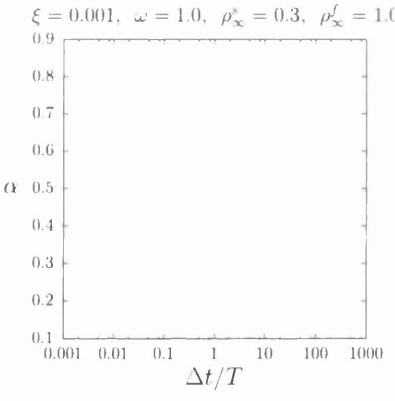
$\xi = 0.001,\ \omega = 1.0,\ \rho^s_\infty = 0.3,\ \rho^f_\infty = 1.0$
α
$\Delta t/T$

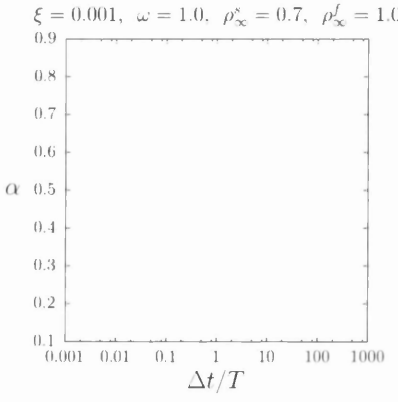
$\xi = 0.001,\ \omega = 1.0,\ \rho^s_\infty = 0.7,\ \rho^f_\infty = 1.0$
α
$\Delta t/T$

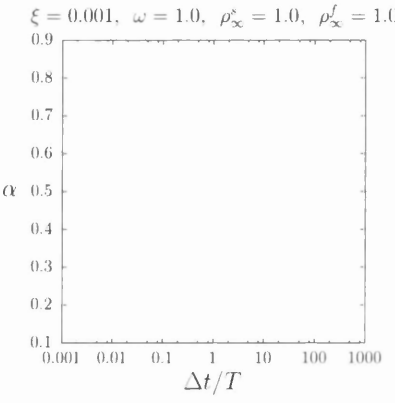
$\xi = 0.001,\ \omega = 1.0,\ \rho^s_\infty = 1.0,\ \rho^f_\infty = 1.0$
α
$\Delta t/T$

Appendix B

Contour plots for eigenvalue analysis - Part 2

For the coupled problem with linearly interpolated traction forces at the interface, the eigenvalue analysis of the amplification matrix given by Equation (4.26) leads to the following contour plots. The used procedure is the same as in A.

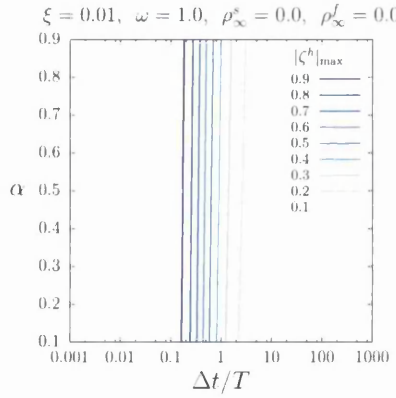
$\xi = 0.01,\ \omega = 1.0,\ \rho^s_\infty = 0.0,\ \rho^f_\infty = 0.0$
$|\zeta^h|_{\max}$
0.9
0.8
0.7
0.6
0.5
0.4
0.3
0.2
0.1
α
$\Delta t/T$

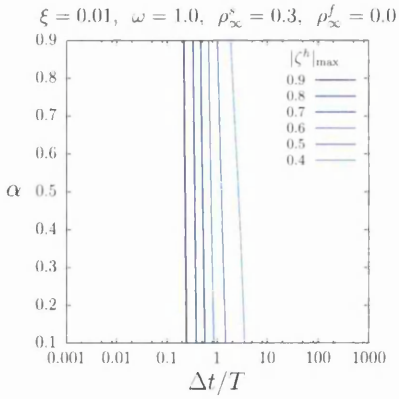
$\xi = 0.01,\ \omega = 1.0,\ \rho^s_\infty = 0.3,\ \rho^f_\infty = 0.0$
$|\zeta^h|_{\max}$
0.9
0.8
0.7
0.6
0.5
0.4
α
$\Delta t/T$

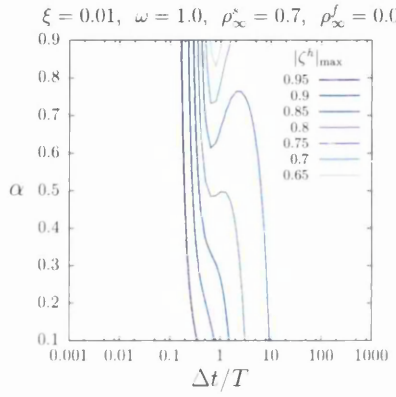
$\xi = 0.01,\ \omega = 1.0,\ \rho^s_\infty = 0.7,\ \rho^f_\infty = 0.0$
$|\zeta^h|_{\max}$
0.95
0.9
0.85
0.8
0.75
0.7
0.65
α
$\Delta t/T$

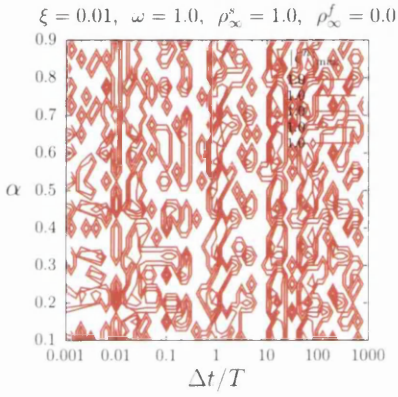
$\xi = 0.01,\ \omega = 1.0,\ \rho^s_\infty = 1.0,\ \rho^f_\infty = 0.0$
α
$\Delta t/T$

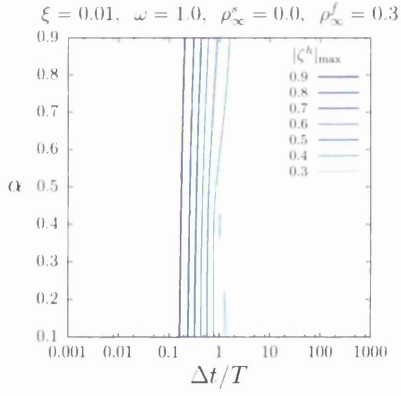
$\xi = 0.01,\ \omega = 1.0,\ \rho^s_\infty = 0.0,\ \rho^f_\infty = 0.3$
$|\zeta^h|_{\max}$
0.9
0.8
0.7
0.6
0.5
0.4
0.3
α
$\Delta t/T$

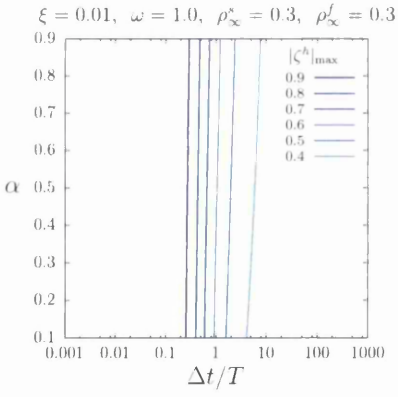
$\xi = 0.01,\ \omega = 1.0,\ \rho^s_\infty = 0.3,\ \rho^f_\infty = 0.3$
$|\zeta^h|_{\max}$
0.9
0.8
0.7
0.6
0.5
0.4
α
$\Delta t/T$

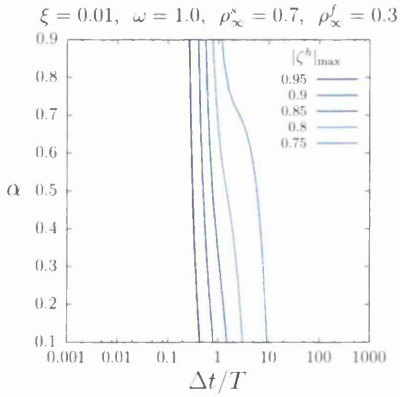
$\xi = 0.01,\ \omega = 1.0,\ \rho^s_\infty = 0.7,\ \rho^f_\infty = 0.3$
$|\zeta^h|_{\max}$
0.95
0.9
0.85
0.8
0.75
α
$\Delta t/T$

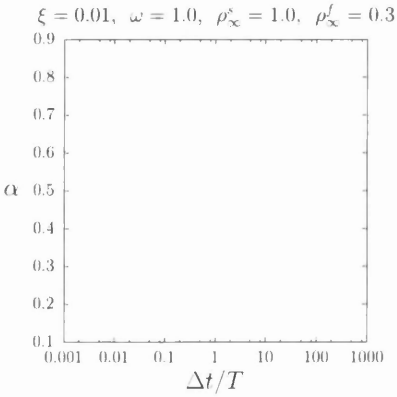
$\xi = 0.01,\ \omega = 1.0,\ \rho^s_\infty = 1.0,\ \rho^f_\infty = 0.3$
α
$\Delta t/T$

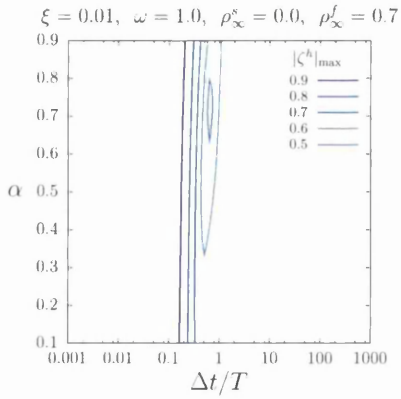
$\xi = 0.01,\ \omega = 1.0,\ \rho^s_\infty = 0.0,\ \rho^f_\infty = 0.7$
$|\zeta^h|_{\max}$
0.9
0.8
0.7
0.6
0.5
α
$\Delta t/T$

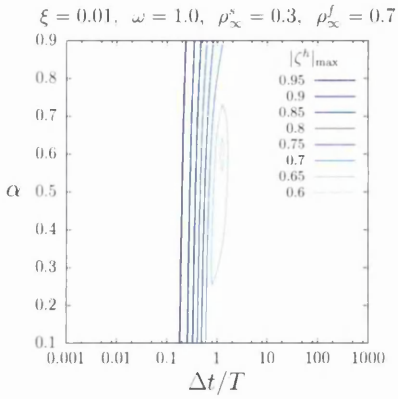
$\xi = 0.01,\ \omega = 1.0,\ \rho^s_\infty = 0.3,\ \rho^f_\infty = 0.7$
$|\zeta^h|_{\max}$
0.95
0.9
0.85
0.8
0.75
0.7
0.65
0.6
α
$\Delta t/T$

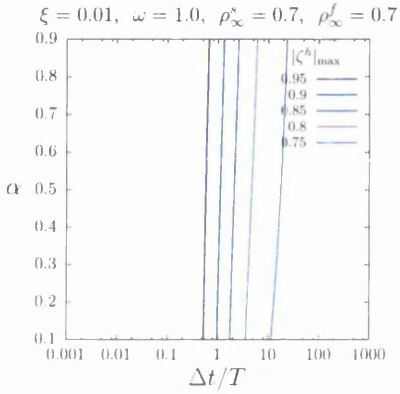
$\xi = 0.01,\ \omega = 1.0,\ \rho^s_\infty = 0.7,\ \rho^f_\infty = 0.7$
$|\zeta^h|_{\max}$
0.95
0.9
0.85
0.8
0.75
α
$\Delta t/T$

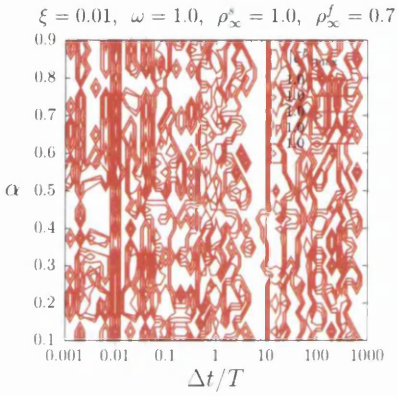
$\xi = 0.01,\ \omega = 1.0,\ \rho^s_\infty = 1.0,\ \rho^f_\infty = 0.7$
α
$\Delta t/T$

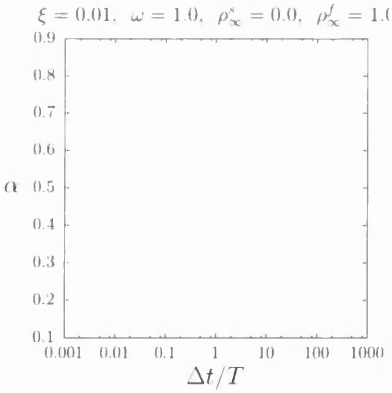
$\xi = 0.01,\ \omega = 1.0,\ \rho^s_\infty = 0.0,\ \rho^f_\infty = 1.0$
α
$\Delta t/T$

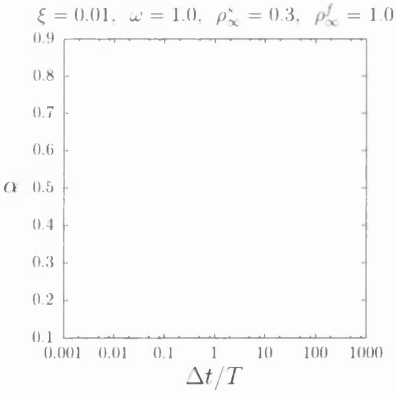
$\xi = 0.01,\ \omega = 1.0,\ \rho^s_\infty = 0.3,\ \rho^f_\infty = 1.0$
α
$\Delta t/T$

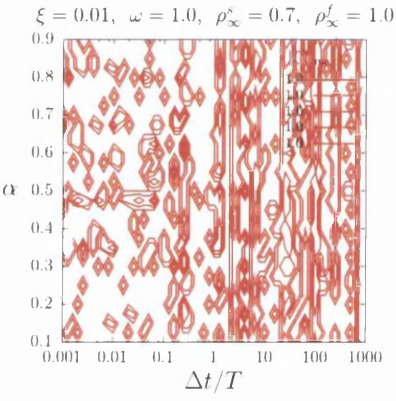
$\xi = 0.01,\ \omega = 1.0,\ \rho^s_\infty = 0.7,\ \rho^f_\infty = 1.0$
α
$\Delta t/T$

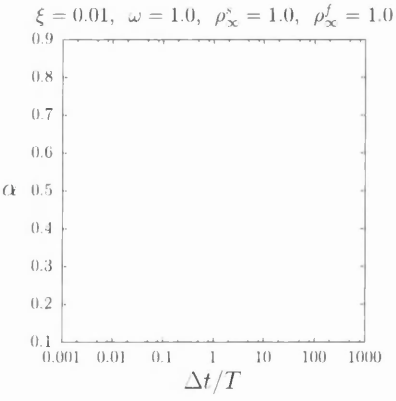
$\xi = 0.01,\ \omega = 1.0,\ \rho^s_\infty = 1.0,\ \rho^f_\infty = 1.0$
α
$\Delta t/T$

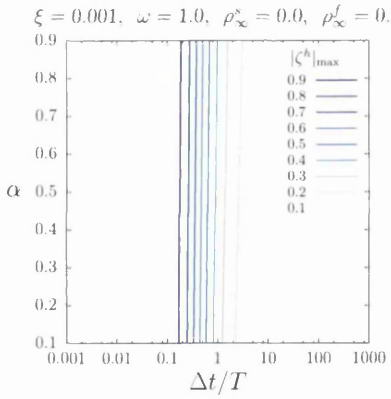
$\xi = 0.001,\ \omega = 1.0,\ \rho^s_\infty = 0.0,\ \rho^f_\infty = 0.0$
$|\zeta^h|_{\max}$
0.9
0.8
0.7
0.6
0.5
0.4
0.3
0.2
0.1
α
$\Delta t/T$

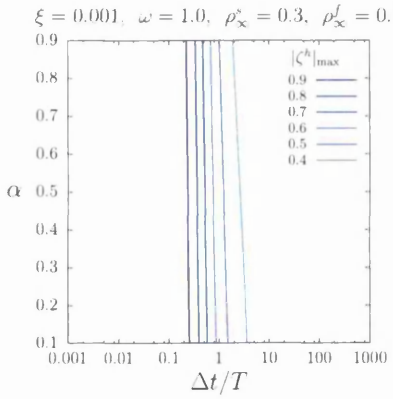
$\xi = 0.001,\ \omega = 1.0,\ \rho^s_\infty = 0.3,\ \rho^f_\infty = 0.0$
$|\zeta^h|_{\max}$
0.9
0.8
0.7
0.6
0.5
0.4
α
$\Delta t/T$

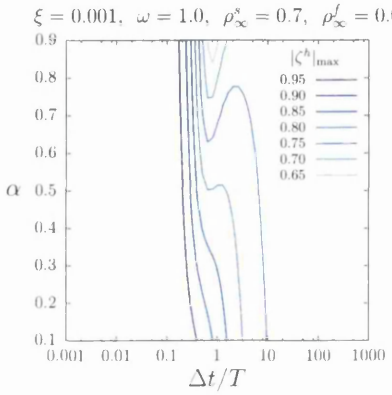
$\xi = 0.001,\ \omega = 1.0,\ \rho^s_\infty = 0.7,\ \rho^f_\infty = 0.0$
$|\zeta^h|_{\max}$
0.95
0.90
0.85
0.80
0.75
0.70
0.65
α
$\Delta t/T$

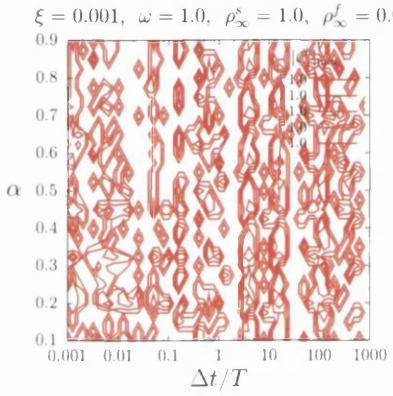
$\xi = 0.001,\ \omega = 1.0,\ \rho^s_\infty = 1.0,\ \rho^f_\infty = 0.0$
$|\zeta^h|_{\max}$
α
$\Delta t/T$

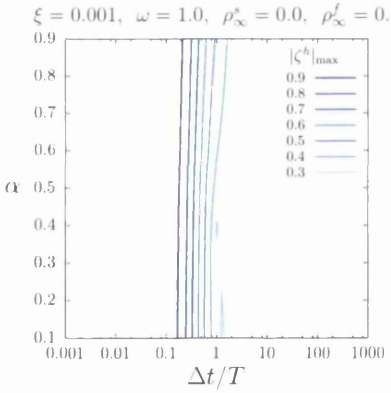
$\xi = 0.001,\ \omega = 1.0,\ \rho^s_\infty = 0.0,\ \rho^f_\infty = 0.3$
$|\zeta^h|_{\max}$
0.9
0.8
0.7
0.6
0.5
0.4
0.3
α
$\Delta t/T$

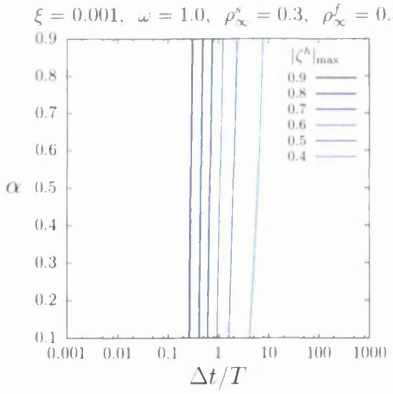
$\xi = 0.001,\ \omega = 1.0,\ \rho^s_\infty = 0.3,\ \rho^f_\infty = 0.3$
$|\zeta^h|_{\max}$
0.9
0.8
0.7
0.6
0.5
0.4
α
$\Delta t/T$

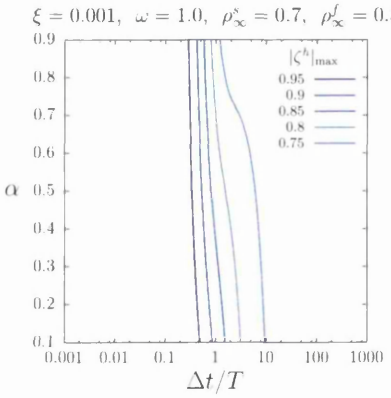
$\xi = 0.001,\ \omega = 1.0,\ \rho^s_\infty = 0.7,\ \rho^f_\infty = 0.3$
$|\zeta^h|_{\max}$
0.95
0.9
0.85
0.8
0.75
α
$\Delta t/T$

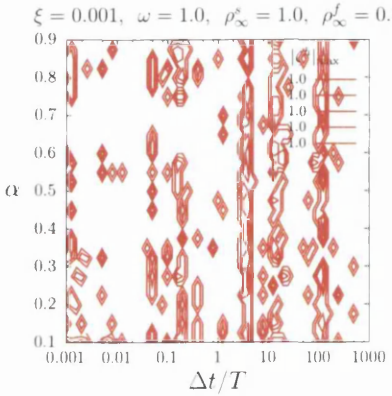
$\xi = 0.001,\ \omega = 1.0,\ \rho^s_\infty = 1.0,\ \rho^f_\infty = 0.3$
$|\zeta^h|_{\max}$
α
$\Delta t/T$

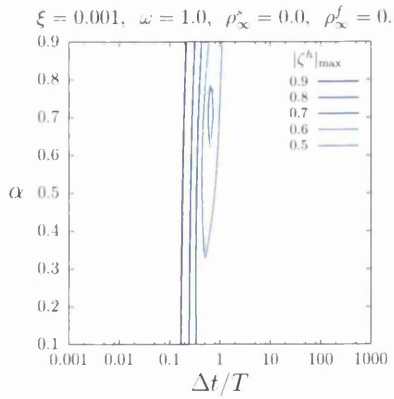
$\xi = 0.001,\ \omega = 1.0,\ \rho_\infty^s = 0.0,\ \rho_\infty^f = 0.7$
$|\zeta^h|_{\max}$
0.9
0.8
0.7
0.6
0.5
α
$\Delta t/T$

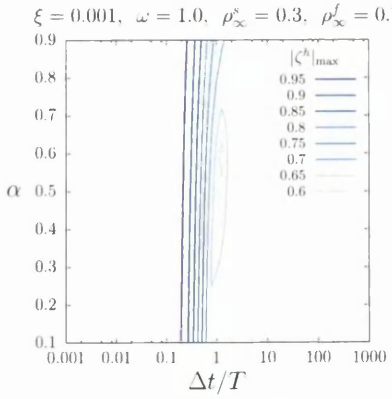
$\xi = 0.001,\ \omega = 1.0,\ \rho_\infty^s = 0.3,\ \rho_\infty^f = 0.7$
$|\zeta^h|_{\max}$
0.95
0.9
0.85
0.8
0.75
0.7
0.65
0.6
α
$\Delta t/T$

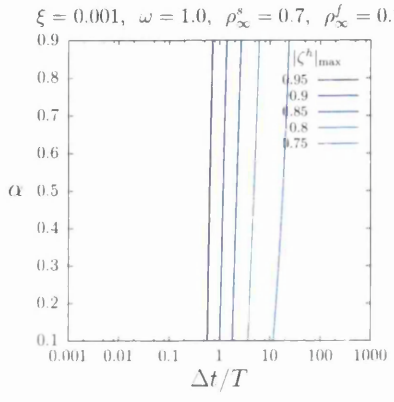
$\xi = 0.001,\ \omega = 1.0,\ \rho_\infty^s = 0.7,\ \rho_\infty^f = 0.7$
$|\zeta^h|_{\max}$
0.95
0.9
0.85
0.8
0.75
α
$\Delta t/T$

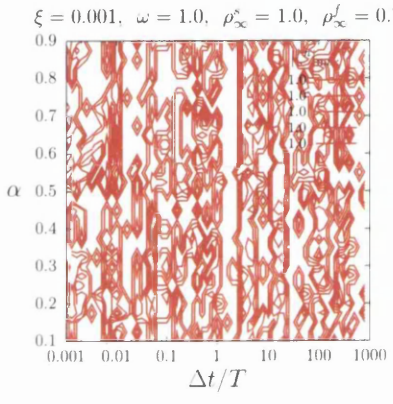
$\xi = 0.001,\ \omega = 1.0,\ \rho_\infty^s = 1.0,\ \rho_\infty^f = 0.7$
α
$\Delta t/T$

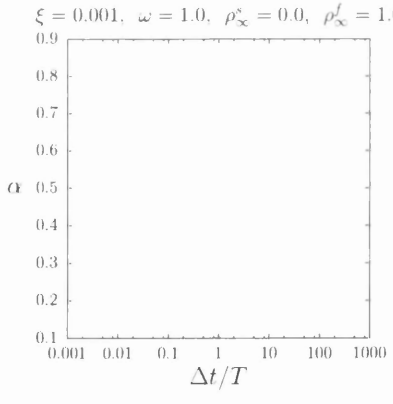
$\xi = 0.001,\ \omega = 1.0,\ \rho_\infty^s = 0.0,\ \rho_\infty^f = 1.0$
α
$\Delta t/T$

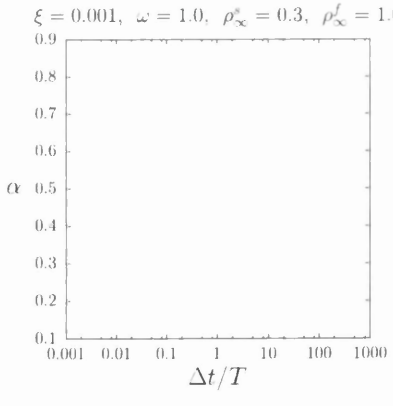
$\xi = 0.001,\ \omega = 1.0,\ \rho_\infty^s = 0.3,\ \rho_\infty^f = 1.0$
α
$\Delta t/T$

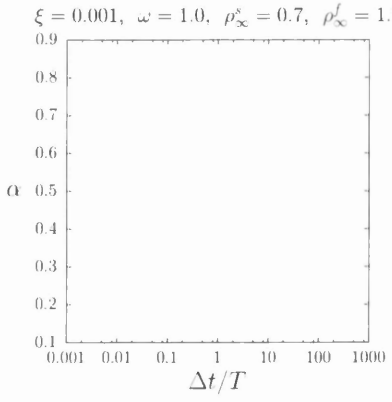
$\xi = 0.001,\ \omega = 1.0,\ \rho_\infty^s = 0.7,\ \rho_\infty^f = 1.0$
α
$\Delta t/T$

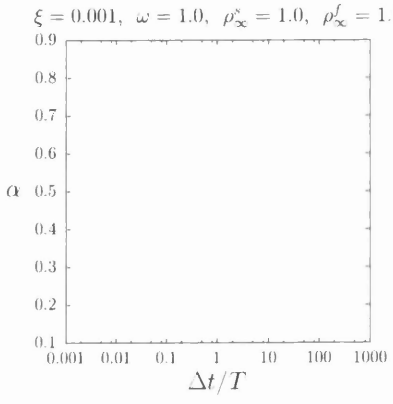
$\xi = 0.001,\ \omega = 1.0,\ \rho_\infty^s = 1.0,\ \rho_\infty^f = 1.0$
α
$\Delta t/T$